Precambrian Molar-Tooth Structure:
Unraveling the Diagenesis of Ancient Carbonates

A Dissertation Presented for the
Doctor of Philosophy
Degree
The University of Tennessee, Knoxville

Agustín Kriscautzky
August 2022

Copyright © 2022 by Agustín Kriscautzky
All rights reserved.

DEDICATION

To the most important in my life: my family.

To my friends, teachers, mentors, and colleagues who kept my passion for geology even during the most challenging times.

ACKNOWLEDGEMENTS

I want to thank my family who have always supported me with no hesitation. Particularly, my parents, who taught me their love for the sciences, their passion for teaching, and their commitment to the community.

I want to thank my "family" in the United Stated: my friends that made this process easier, helped me, supported me, and made me laugh when I needed.

I want to thank my friends from Argentina and the world, who have always been in touch and had the time to be with me even at the distance: Times during the COVID19 pandemic in 2020 and 2021 would have not been the same without their encouragement.

I want to thank Linda Kah for her guidance and support, and for trusting in me in the lab, in the field, and in the classroom, and thanks to whom I am pursuing my graduate degree.

I want to acknowledge my committee, Dr. Anna Szynkiewicz, Dr. Molly McCanta, and Dr. Julie Bartley (and formerly Dr. Michael Essington), for their time advocated to my qualifying exams, and for their commitment to enriching my dissertation and research.

I want to thank all of those who trusted in me during these past five years in the United States, and without whom I would have not learn that much: professors, technicians, and staff.

I want to acknowledge the College of Art and Sciences, the Department of Earth and Planetary Sciences, and the Advisory Board for their invaluable support when it was the most needed.

Funding for the projects related to this thesis was provided by the Geological Society of America (GSA), the Sedimentary Geology Division of the GSA, The National Aeronautics and Space Administration (NASA), the National Science Foundation (NSF), the National Geographic Society, and the Kenneth R. Walker Professorship fund. To all of them, thank you.

ABSTRACT

Molar-tooth structure (MTS) is an enigmatic carbonate fabric that occurs mainly within Proterozoic carbonate host rocks. It is composed of two distinct features: cracks of various morphologies and crack-filling calcite microspar. Although the origins of MTS remain unknown, most previous investigation has focused on the formation of the cracks and mechanisms involved in the void space generation, with less emphasis on the intriguing carbonate fill. In this study I have investigated molar-tooth bearing carbonates from regions that span both paleogeography and geologic time. Analysis at the microscopic scale, including traditional petrography, cathodoluminescence petrography, scanning electron microscopy, and micrometer-scale geochemical analyses (Chapters 1 and 2) provides a fresh look at MTS that augments the more traditional sedimentological and stratigraphical observations in the field (Chapter 3). Combined, these works provide a solid base of evidence to guide studies into MTS and will aid in our understanding of the evolution of the Earth's ancient oceans and processes of carbonate diagenesis through time. Specifically, this investigation demonstrates the complexity of carbonate precipitation and its earliest diagenesis, and therefore provides a key context for the evaluation and interpretation of isotopic and trace elements analyses that involve the evolution of carbonate phases through geologic time.

TABLE OF CONTENTS

INTRODUCTION 1
CHAPTER I 4
PRECAMBRIAN MOLAR-TOOTH STRUCTURE: A REVIEW OF ITS DEPOSITION AND DIAGENESIS 4
Abstract 5
Introduction 6
Molar-Tooth Structure 7
What is Molar-Tooth Structure? 7
Distribution of Molar-Tooth Structure in Space and Time 9
Timing of Molar-Tooth Structure Formation 11
Potential Mechanisms of Molar-Tooth Structure Formation 12
A biological origin 12
An evaporite origin 12
Formation via sediment shrinkage 13
Formation via stress-induced cracking 13
Formation via gas expansion and migration 14
Petrography of Molar-Tooth Structure 15
Petrographic Characteristics of Molar-Tooth Structure 15
Cathodoluminescence Characteristics of Molar-Tooth Structure 17
Discussion 22
Environments of molar-tooth structure genesis 22
Genesis of molar-tooth microspar 23
Stabilization of molar-tooth microspar 24
Molar-tooth microspar as a target for geochemical analysis 26
Conclusions 27
Aknowledgements 28
References 29
CHAPTER II 37
ORIGIN AND EARLY DIAGENESIS OF PRECAMBRIAN MOLAR-TOOTH MICROSPAR: EVIDENCE FROM CRYSTAL SIZE DISTRIBUTIONS AND GEOCHEMISTRY 37
Abstract 38
Introduction 38
Molar-tooth Structure 38
Models of Formation 40
Investigation of MT microspar 43
Crystal Size Distributions 44
Crystal Size Distributions and Molar-Tooth Microspar 46
Samples and data collection 48
Results and interpretations 50
CSDs 50
Elemental analyses and X-ray maps 54

Discussion 62
Conclusions 66
Acknowledgements 67
References 68
CHAPTER III 76
EVIDENCE OF THE ROLE OF SUBSTRATE RHEOLOGY AND LOCAL CARBONATE SATURATION ON THE FORMATION OF CARBONATE MOLAR-TOOTH STRUCTURE 76
Abstract 77
Introduction 77
Molar-Tooth Structure 77
Hypothesized MTS Formation mechanisms 78
MTS in the geologic record 81
Geology and Age of the Qingyunshan National Geopark 84
MT Occurrences 84
Discussion 89
Mechanism for the development of concretions 89
Formation of Zhangqu Formation MT-bearing concretions 94
Formation of MTS in time and space 97
Conclusions 98
Acknowledgements 99
References 100
Appendix I 107
Appendix II 120
Appendix III 121
Vita 123

LIST OF FIGURES

Figure 1.1	Field expression of MTS.	8
Figure 1.2	Distribution of MTS in time and space.	10
Figure 1.3	Petrographic character of MT microspar. (Petrographic microscope)	16
Figure 1.4	Petrographic character of MT microspar. (Cathodoluminescence)	18
Figure 1.5	Cathodoluminescence highlights variability in MT microspar cores.	20
Figure 1.6	Cathodoluminescence highlights a complex depositional and diagenetic history of MT microspar.	21
Figure 2.1	Outcrop photographs of molar-tooth structure exposed on weathered surface.	39
Figure 2.2	Distribution of MTS occurrences in space and time.	41
Figure 2.3	Standard shapes of CSDs.	45
Figure 2.4	Cathodoluminescence photomicrographs.	47
Figure 2.5	Comparison between MT images obtained with different techniques from polished thin section surfaces.	49
Figure 2.6	Distribution of the short/long axis ratio versus the long axis.	52
Figure 2.7	Crystal size distributions of MT microspar cores (left) and whole crystals (cores plus rims; right)	55
Figure 2.8	Backscattered electron images and elemental X-ray maps.	59
Figure 2.9	Backscattered electron image and CL photomicrograph of dolomite crystals crosscutting MT microspar.	61
Figure 3.1	Outcrop view of MTS on weathered surface.	79
Figure 3.2	Distribution of MTS occurrences in space and time.	82
Figure 3.3	Field view of nested rings and septae in MTS from the Zhangqu Formation, China.	83
Figure 3.4	Location of the study site.	85
Figure 3.5	Stratigraphic column of the Proterozoic Huaihe Group.	86
Figure 3.6	Molar-tooth structure from the lowest section of the Zhangqu Formation showing thick, slightly curvilinear, vertical features.	87
Figure 3.7	Brecciated MTS and stromatolite intervals within the Zhangqu formation.	88
Figure 3.8	Plan view of three-dimensional MT-bearing bodies.	90
Figure 3.9	Dense accumulation of MTS within ellipsoidal bodies.	91
Figure 3.10	Variability of MTS within a single ellipsoidal body.	92
Figure 3.11	Examples of beds indicating seismic deformation and liquefaction.	96
Figure 4.1	Distribution of the Short/Long axis ratio versus the long axis per individual sample.	121

MTS: Molar-tooth Structure

INTRODUCTION

Overview: Molar-tooth structure (MTS) is an enigmatic carbonate fabric that shows distinctive complex arrays of variously planar, folded, and broken sheets filled with micritic calcite, generally occurring within ancient argillaceous carbonate host rocks (Bauerman 1885, Daly 1912, Fenton and Fenton 1937, Rezak 1957, Ross 1959). MTS occurs primarily in association with fine-grained, laminated, carbonate rocks (Furniss et al. 1998, Hodgskiss et al. 2018), although these structures also occur in fine-grained siliciclastic rocks (Bishop and Sumner 2006; Bishop et al. 2006; Gilleaudeau and Kah 2010; Pratt 2011; Stewart and Mauk 2017; L.C. Kah and J.K. Bartley, unpublished data) and more rarely in coarse-grained carbonate and siliciclastic lithologies (Pratt 1998, Pollock et al. 2006). As a sedimentary structure, MTS appears globally in shallow marine systems and is restricted in time to Precambrian successions, lacking a known modern analog.

Molar-tooth carbonate: Molar-tooth structure consist of two elements: voids and crack of various sizes and shapes (cracks), and a homogeneous calcite microspar cement that fills the cracks (micrite) (Fairchild et al. 1997, Furniss et al. 1998, Pollock et al. 2006). The formation of fractures and voids within a host material, requires that MTS formed within the sedimentary substrate, and the lithologically distinct character of molar-tooth (MT) microspar, which typically lacks detrital infill (Furniss et al. 1998, Pollock et al. 2006), is consistent with MT microspar forming as an in situ precipitate near the sediment-water interface. The micrite shows an intriguing similarity regardless of age, host lithology or geographic location. This calcite filling is composed of uniform, equant, limpid crystals that show planar, noninterlocking boundaries. This fabric defies a straightforward interpretation but is considered as a critical record of Precambrian marine environments that may help better understand atmospheric-ocean evolution of the early Earth (James et al. 1998, Shields 2002, Fairchild et al. 2018, Cantine et al.2019, Kah and Bartley 2021).

Relevance: A growing interest in the geochemical reconstruction of Precambrian marine environments (Lyons et al. 2009, Halverson et al. 2010, Fike et al. 2015) has renewed an overall interest in MTS, and a specific interest in the microcrystalline calcite that comprises them. The MT microspar, inferred to be a synsedimentary precipitated phase little altered by diagenesis (Bishop and Sumner 2006, Pollock et al. 2006), is assumed to be an ideal proxy for constraining marine composition (Wu et al. 2020, Zhou et al. 2020), redox conditions (Frank and Lyons 1998, Shen et al. 2016, Hodgskiss et al. 2018), marine pH, pCO_2, and carbonate saturation (Tosca et al. 2011, Strauss and Tosca 2020, Roest-Ellis et al. 2021).

Outcome: This study focuses on MTS from different Proterozoic basins across the globe and adds relevant data to the understanding of the genesis of this unusual fabric. This work produced a series of detailed petrographic and field observations, along with geochemical interpretations that provide a solid base to expand our understanding of the composition of ancient oceans, and the diagenetic processes involved in the alteration of carbonates. A

complete understanding for the timing and mechanisms of voids formation, and the following precipitation of microspar is key to trace the diverse diagenetic pathways experienced by individual MTS occurrences and to evaluate the fidelity of geochemical signals and rheological interpretations.

CHAPTER 1: In chapter 1, I provide a thorough review of the literature to summarize MTS occurrences in time and space and analyze its mechanisms of formation. As part of the review, I contribute the first comparative petrographic analysis of MTS. This analysis includes samples from various localities and ages using both traditional and cathodoluminescence microscopy. With this information, I provide a new model for the crystallization and early diagenesis of MT microspar. In this model, MT microspar first forms a precursor gel phase of amorphous calcium carbonate (ACC) that initiates mineral growth and helps preserve the void space. This is followed by the subsequent diagenesis of the ACC and precipitation of a crystalline phase. Crystals resulting from this process show a characteristic zoning, with a defined inner core, surrounded by an isopachous rim, easily observed with cathodoluminescence microscopy. Of the many models for MT formation that have been previously proposed, a void formation mechanism based on gas expansion and migration (Furniss et al. 1998) is most consistent with observations of the morphology of MT voids and the distribution of MT microspar (Pollock et al. 2006) I, therefore use a scenario of gas expansion and migration as the basis for the hypothesized model for microspar precipitation. Additionally, I have used the petrographic observations provided in this chapter to show that despite the generally well-preserved nature of MTS, MT microspar is not exempt from diagenetic recrystallization. By detailing the petrography of MTS collected across both time and space, I show how such detailed petrographic framework is therefore critical to properly assess geochemical interpretations.

CHAPTER 2: In chapter 2, I use detailed microscopic crystal size measurements and microprobe trace element geochemistry to test the hypothesized model for MT microspar formation that I developed in Chapter 1. I first investigate MT microspar crystal size distributions (CSD), which characterize crystalline materials utilizing the shape of the size frequency distribution curve to infer nucleation and growth (Cashman and Marsh 1988; Marsh 1988) and crystal ripening (cf. Berger et al. 2011). CSDs are traditionally used in igneous systems; however, this technique has also been used to interpret nucleation, growth, and recrystallization of chemical precipitates in aqueous systems (Kile and Eberl 2003; Kile et al. 2000; Eberl et al. 1998; Wilkin 1995). In addition to CSDs, I also include electron microprobe trace element analyses and X-ray elemental maps to elucidate the distribution of the major and minor elements Mg, Sr, Fe, and Mn between cores and rims of the MT microspar. Together, these studies clearly show that the observation of the distinct formational zones that comprise each single crystal (core and rim) is best represented by a distinct two-step nucleation and growth process separated by an episode of Ostwald ripening of the microspar cores (i.e., the dissolution of the smaller, less stable nuclei and reprecipitation of carbonate on more stable nuclei to form larger crystals). Microspar rims appear to have grown by surface-controlled processes, nucleating on the previously precipitated cores. This pattern is also observed in the trace element distribution, being very clear for Mg (which is depleted in the cores and concentrated in the rims) and is consistent with a hypothesis where the microspar formation initially involved the formation of hydrated amorphous calcium carbonate within a gel phase.

CHAPTER 3: In contrast to the first two chapters, in Chapter 3, I take a broader look at the formation of MTS by exploring the potential morphology of unusual MTS from the Neoproterozoic Zhangqu Formation (Qingyunshan National Geopark, Anhui Province, China) and hypothesizing

what this unusual morphology means in terms of substrate rheology. Molar-tooth structure here present a distinct, intricate, system of cracks occurring within meter-scale ellipsoidal bodies. These accumulations of MTS within clearly defined concretionary structures show commonly arcuate, thicker, and polygonal ribbons, often broken and nested with second order, smaller MTS. I provide detailed field observations of the stratigraphic record and the development of these enigmatic features within the Zhangqu Formation. I also provide evidence of bending of sedimentary beds, crosscutting relationships, later veins, and observations of differential physical behavior of sedimentary strata related to the concretions. All these observations suggest that formation of MT voids was constrained by spatial variation in local carbonate saturation and substrate rheological properties. I further hypothesize that the preservation of MTS within concretions, which has been observed only from later Neoproterozoic successions, may provide evidence of changing marine carbonate saturation states at this time.

SUMMARY: In sum, within this dissertation I provide the first thorough petrographic analysis of Proterozoic MTS. I also provide new constraints on its formation from a combination of geochemical analyses and interpretations of crystal size distributions. Finally, I provide a new set of field observations of unusual MTS from the Neoproterozoic of China. Together these elements expand our knowledge of MTS in the Precambrian record, its formation, preservation, and diagenetic evolution. My contributions will provide an empirical base from which further studies can arise to better understand ancient oceans and carbonate diagenesis. Synthetically, in Chapter 1, I review what is known about this carbonate fabric, and I propose a mechanism of formation by the precipitation of carbonate from an amorphous gel phase. In Chapter 2, I elaborate on this hypothesis by adding statistical methods based on empirical and geochemical data and observations. Finally, in Chapter 3, I look at a broader scale by analyzing the rheological conditions needed to form and emplace MTS within the stratigraphic record.

CHAPTER I

PRECAMBRIAN MOLAR-TOOTH STRUCTURE: A REVIEW OF ITS DEPOSITION AND DIAGENESIS

A version of this chapter was originally published by Agustin Kriscautzky, Linda C. Kah, and Julie K. Bartley, and it is reproduced here with permission from the Annual Review of Earth and Planetary Sciences, Volume 50; copyright 2022 Annual Reviews, https://www.annualreviews.org/:

Kriscautzky, A., Kah L.C., and Bartley J.K., 2022. Molar-Tooth Structure as a Window into the Deposition and Diagenesis of Precambrian Carbonate. Annual Review of Earth and Planetary Science 50:205-2030.

This publication was an invited submission to the Annual Review of Earth and Planetary Sciences. The article is a thorough review of a Precambrian carbonate structure called molar-tooth (MT). Additionally, to the literature review, this paper brings new hypotheses and data on how the carbonate fabric formed and its diagenetic process through time, incorporating detailed petrographic analyses. It also discusses if this carbonate precipitated from amorphous calcium carbonate within a gel phase. The manuscript was peer-reviewed anonymously both by external reviewers and by the editorial board of the specialized journal. I wrote the article with guidance and feedback from my advisor and coauthor of the paper, Dr. Linda Kah. Dr. Kah has one of the most extensive MT sample collections worldwide, and she participated in numerous field excursions on this matter, with invaluable knowledge in this regard. Dr. Julie Bartley participated in many of these field excursions and published articles on MT carbonates. She has a more chemical-oriented background, which was of great help. Both coauthors provided extensive literature and helped with editing, formatting, and correcting English grammar and spelling, and largely enriched the discussions given their knowledge and experience.

ABSTRACT

Molar-tooth structure (MTS) is an unusual carbonate fabric that is composed of variously shaped cracks and voids filled with calcite microspar. Despite a century of study, MTS remains enigmatic because it juxtaposes void formation within a cohesive yet unlithified substrate with the penecontemporaneous precipitation and lithification of void-filling carbonate microspar. MTS is broadly restricted to shallow marine carbonate strata of the Mesoproterozoic and Neoproterozoic, suggesting a fundamental link between the formation of MTS and the biogeochemical evolution of marine environments. Despite uncertainties in the origin of MTS, molar-tooth (MT) microspar remains a popular target for geochemical analysis and the reconstruction of Precambrian marine chemistry. Here we review models for the formation of MTS and show how detailed petrographic analysis of MT microspar permits identification of a complex process of precipitation and diagenesis that must be considered when the microspar phase is used as a geochemical proxy.

- Molar-tooth fabric is an enigmatic structure in Precambrian sedimentary rocks that is composed of variously shaped cracks and voids filled with carbonate microspar.
- Time restriction of this fabric suggests a link between this unusual structure and the biogeochemical evolution of marine environments.

- Petrographic analysis of molar-tooth fabric provides insight into fundamental processes of crystallization.

INTRODUCTION

Molar-tooth structure (MTS) was first reported from the Belt Supergroup of NW Montana and SE British Columbia, where the term was used to describe a diverse and complex array of structures that consist of variously planar, folded, and broken sheets of lithologically pure calcite that occur as a distinct phase within generally argillaceous carbonate host rock (Bauerman 1885, Daly 1912, Fenton & Fenton 1937, Rezak 1957, Ross 1959). Since these earliest descriptions, MTS has been widely recognized as a sedimentary structure without modern analog, with a complex structure that resists ready description and categorization and that defies straightforward explanation. Yet MTS continues to command the attention of geoscientists: Its spatial distribution in shallow marine systems, its temporal restriction to the Precambrian, and its striking similarity across the globe all suggest that MTS must have some as-of-yet undetermined importance in our understanding of the early Earth (James et al. 1998, Shields 2002, Fairchild et al. 2018, Cantine et al.2019, Kah & Bartley 2021).

More recently, a growing interest in the geochemical reconstruction of Precambrian marine environments (Lyons et al. 2009, Halverson et al. 2010, Fike et al. 2015) has renewed an overall interest in MTS and a specific interest in the microcrystalline calcite that comprises MTS. Because the calcite microspar associated with MTS has been inferred to be a synsedimentary precipitate that is little altered by diagenesis (Bishop & Sumner 2006, Pollock et al. 2006), it is commonly assumed to be an ideal target for geochemical analysis aimed at constraining marine isotopic and elemental composition (Wu et al. 2020, Zhou et al. 2020), redox (Frank & Lyons 1998, Shen et al. 2016, Hodgskiss et al. 2018), and marine pH, pCO_2, and carbonate saturation (Tosca et al. 2011, Strauss & Tosca 2020, Roest-Ellis et al. 2021). The origin of both molar-tooth (MT) voids and void-filling microspar, however, remains poorly constrained, and a comprehensive understanding of MTS is hampered by a paucity of fine-scale petrographic and geochemical analyses of these enigmatic carbonate textures.

Here we review the occurrence of MTS through Precambrian time and space and synthesize observations that provide evidence for the timing and mechanisms of void formation and carbonate precipitation. We then provide detailed petrographic analysis of MTS to illuminate the pathways of precipitation, neomorphism, and diagenesis recorded by the void-filling microspar. We argue that MTS, or more specifically its characteristic microspar infill, shares a set of primary and early diagenetic petrographic features that are observed across both time and space. Recognition of this common microstructure, established during initial precipitation and stabilization of MTS, enables us to more confidently trace the diverse diagenetic pathways experienced by individual MTS occurrences and to evaluate the fidelity of geochemical signals obtained from these phases. We argue that the void-filling microspar associated with MTS provides a unique window into the complex process of carbonate precipitation and stabilization, but is not unaffected

by diagenetic alteration, which must be taken into account when the microspar phase is used as a geochemical proxy.

Molar-Tooth Structure

What is Molar-Tooth Structure?

MTS consists of two discrete elements: (*a*) variously shaped voids and cracks within host sediments (which we group together and call MT voids) and (*b*) a characteristically homogeneous carbonate microspar that fills these voids (which we term MT microspar) (Fairchild et al. 1997, Furniss et al. 1998, Pollock et al. 2006) (Figure 1.1). In the field, MTS is typically visible on weathered rock surfaces as sharply bounded, light to dark gray features. MTS occurs within a wide variety of sediment lithologies but is most commonly observed in fine-grained, clayey to silty, mechanically or microbially laminated carbonate rocks (Furniss et al. 1998, Hodgskiss et al. 2018). MTS is recorded less commonly in fine-grained siliciclastic rocks (Bishop & Sumner 2006; Bishop et al. 2006; Gilleaudeau & Kah 2010; Pratt 2011; Stewart & Mauk 2017; L.C. Kah & J.K. Bartley, unpublished data) and occurs only rarely in coarse-grained carbonate and siliciclastic lithologies (Pratt 1998, Pollock et al. 2006).

MTS is characterized by widely diverse morphologies, both within and across individual occurrences, but is most often described in terms of its end member forms, which consist of sheet-like ribbons (Figure 1.1*a*) and discrete spheroidal blebs (Figure 1.1*b*). Whereas blebs are commonly only a few millimeters in diameter, ribbons can range from a few millimeters to several centimeters in width and a few to tens of centimeters in length. In many cases, MTS passes from one morphology to the other and intersects in three dimensions to form complex interconnected networks (Furniss et al. 1998, Pratt 1998, Long 2007, Smith 2016). A key feature of these networks, however, is that the homogeneous carbonate microspar typically appears to continue, without break, through interconnected voids (Frank & Lyons 1998, Furniss et al. 1998, Bishop & Sumner 2006, Pollock et al. 2006, Long 2007).

Detailed analysis of the morphology of MTS has also shown that MT ribbons exhibit a variety of morphologies both within single host lithologies and when features intersect lithologically distinct host sediments, suggesting substantial rheologic control on the morphology (Pollock et al. 2006). Within a given host lithology, thinner ribbons tend to be more sinuous and morphologically complex, whereas thicker ribbons are morphologically simpler (Figure 1.1*c*). Changes in orientation of MT ribbons commonly occur at the interface between host lithologies; for example, MT ribbons may shift orientation from vertical to horizontal beneath cohesive microbial laminae or clay layers (cf. Bishop & Sumner 2006, Pollock et al. 2006, Kuang 2014, Hodgskiss et al. 2018) (Figure 1.1*d*), may narrow or pinch within silt and fine sand interbeds (cf. Pratt 2011), and may become diffuse within or terminate at coarse-grained horizons (cf. Fairchild et al. 1997, Pratt 1998, Pollock et al. 2006).

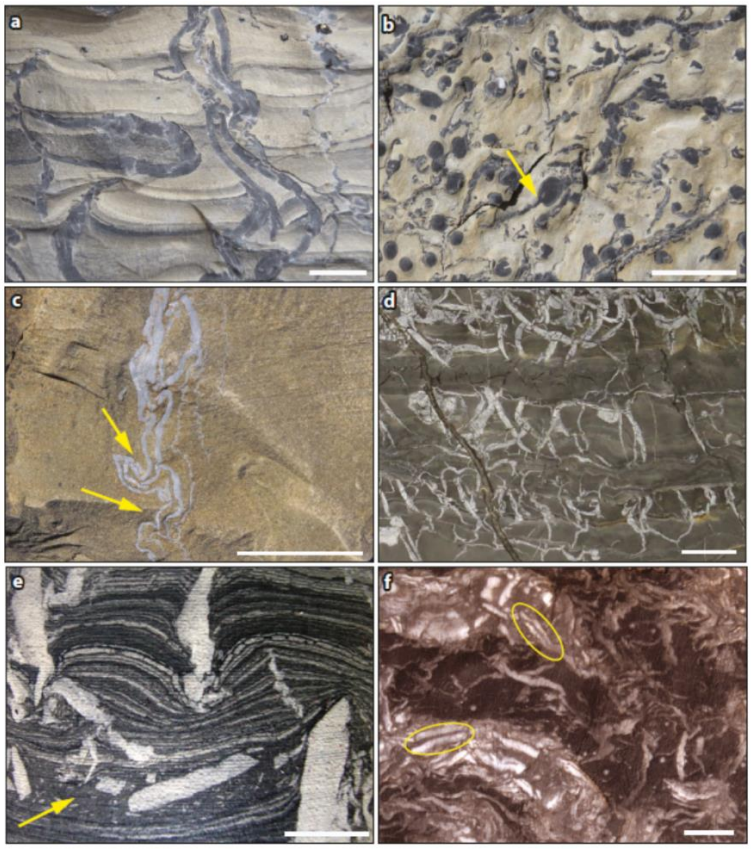


Figure 1.1. Field expression of MTS. (*a*) Broadly arcuate MT ribbons from the Mesoproterozoic Belt Supergroup, USA. MT ribbons crosscut host rock, which consists of variously clayey to silty carbonate that shows differential compaction around MTS. (*b*) MT blebs from the Mesoproterozoic Belt Supergroup, USA. Spheroidal blebs are best explained by gas expansion within the substrate; when gas pressures exceed the strength of the cohesive substrate, cracks form that penetrate the surrounding sediment (*arrow*). (*c*) Ptygmatic folds in MT ribbons from the Neoproterozoic Shandong Province, China. Apparent folding represents the differential behavior during crack propagation through a heterogeneous substrate wherein the morphology of thin cracks is more strongly affected by substrate heterogeneities than wider cracks. Note minor breakage (*arrows*) implying rigidity of MTS at the time of compaction of surrounding sediment. (*d*) MTS of the Neoproterozoic Anhui Province, China. Orientation of MT ribbons is commonly correlated with changes in substrate composition and indicates that crack-forming mechanisms are strongly affected by substrate rheology. (*e*) Interval of breccia (*arrow*) within strata of the Mesoproterozoic Atar Group, Mauritania. Breccia clasts are composed exclusively of locally derived MTS. (*f*) Multiple generations of MTS within tsunami deposits of the Mesoproterozoic Atar Group, Mauritania. Clasts (*white*) represent the first generation of MT, which is incorporated into a second generation of MT microspar (*gray*), and fluidized carbonate substrate (*dark gray*) is penetrated by a later generation of MTS. The scale bar is 1 cm in all panels.

Successions that bear MTS also frequently contain intraformational breccias that consist largely of clasts of MTS that may exhibit a combination of brittle and ductile deformation. These breccias record the erosional exhumation, deformation, and redeposition of MTS. Most commonly, breccia deposits occur as discontinuous millimeter- to centimeter-scale lenses containing clasts identifiable as reworked MTS (cf. Furniss et al. 1998; Pratt 1998, 2001) (Figure 1.1*e*). In the more extreme cases, MTS is preserved within fluidized beds both as nodular clusters of broken, contorted, and fragmented ribbons, and as intact ribbons (Moussine-Pouchkine & Bertrand-Sarfati 1997; Stagner et al. 2004; Kah et al. 2007, 2012) (Figure 1.1*f*).

Distribution of Molar-Tooth Structure in Space and Time

MTS has been recognized in a wide variety of Precambrian units, ranging in age from the Archean to the Ediacaran. In accordance with earlier findings (James et al. 1998, Pratt 1998, Kuang 2014, Smith 2016), MTS appears to be a Precambrian phenomenon. Figure 1.2 provides a summary of the distribution of known MTS occurrences and provides the best estimate—within 200 My bins—for the ages of these occurrences (see the Appendix I for a detailed tabulation of formations containing MTS). The oldest examples of MTS occur in Archean-aged shale of the Transvaal Supergroup (Bishop & Sumner 2006, Bishop et al. 2006), and the youngest examples occur within Ediacaran-aged cap carbonate deposits (Shields 2002, Shields-Zhou et al. 2012, Hodgskiss et al. 2018). The vast majority of MTS is recorded in the Mesoproterozoic and Neoproterozoic, in strata between 1.6 and 0.6 Ga (55 of 70 formations containing MTS, or 79%), with a clear peak in global abundance in the late Mesoproterozoic to early Neoproterozoic, between 1.2 and 0.8 Ga (41 of 70 formations, or 59%). Although observations of structures similar to MTS have also been reported from younger strata (Winston et al. 1999, Rossetti 2000, Rossetti & Góes 2000, Miller et al. 2018), we consider that these occurrences are best referred to as MT-like structures; whereas void morphology is similar to that of MTS, these features lack clear evidence of the characteristic carbonate microspar that is a fundamental component of Precambrian MTS (Fairchild et al. 1997, Pollock et al. 2006).

The apparent time restriction of MTS is generally interpreted as to reflect the global evolution of carbonate environments (Shields 2002, Pollock et al. 2006, Hodgskiss et al. 2018, Cantine et al. 2019, Kah & Bartley 2021). In this explanation, Archean and early Proterozoic environments were dominated by penecontemporaneous cementation of carbonate substrates (Grotzinger 1989; Sami & James 1996; Sumner 1997, 2000; Grotzinger & Knoll 1999), which prohibited void formation in carbonate-dominated substrates. It is important to note that Archean-aged examples of MTS occur within siliciclastic, rather than carbonate, substrates that may not have undergone synsedimentary lithification. By contrast, later Proterozoic environments were dominated by deposition of micritic carbonate produced in the water column (Grotzinger 1989, 1990) potentially reflecting a global decrease in marine carbonate saturation state (Bartley & Kah 2004), which would have favored the retardation of substrate cementation necessary for void formation. In this scenario, Mesoproterozoic to early Neoproterozoic strata that preserve the majority of MTS occurrences (Figure 1.2) represent a transitional interval (cf. Kah &

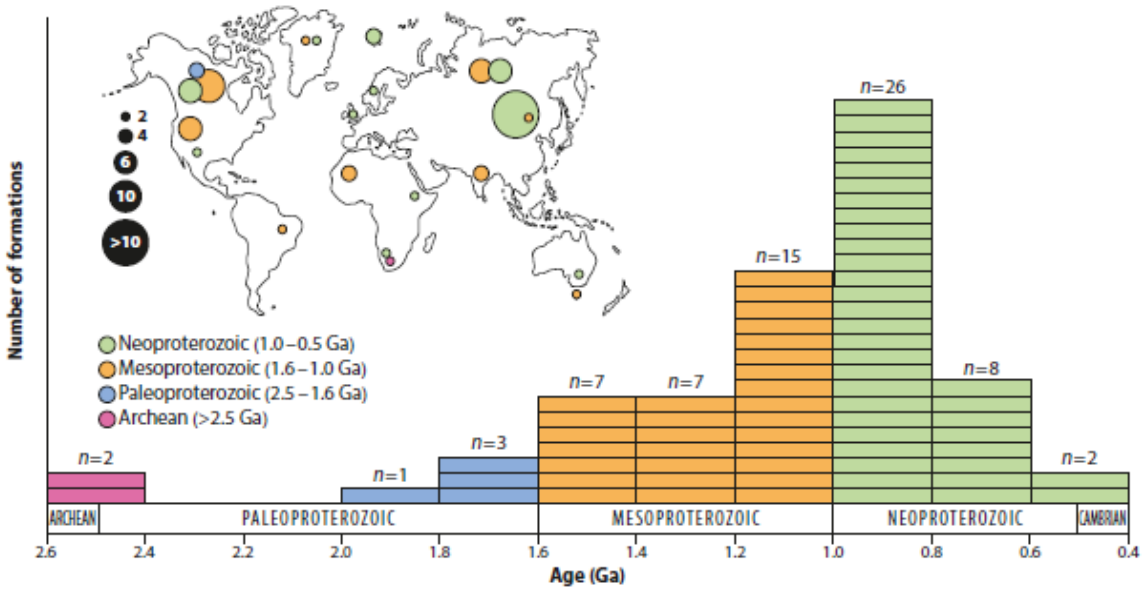


Figure 1.2. Distribution of MTS in time and space. Map inset shows the spatial distribution of MTS occurrences by region; the size of the circle represents the number of formations in which MTS is recorded, and the color of the circle represents age. The main panel shows the time distribution of MTS; formations are binned into 200 My intervals and color coded by era. See Appendix I for full list of occurrences.

Knoll 1996, Bartley & Kah 2004, Kah & Bartley 2021) that permitted both void formation within unlithified substrates and the penecontemporaneous precipitation of microspar within MT voids. A continued decrease in carbonate saturation (Shields 2002, Pollock et al. 2006, Hodgskiss et al. 2018) further inhibited the precipitation of microspar within MT voids, ultimately leading to the disappearance of MTS.

Timing of Molar-Tooth Structure Formation

The formation of fractures and voids within a host material clearly requires that MTS formed within the sedimentary substrate, and the lithologically distinct character of MT microspar, which typically lacks detrital infill (Furniss et al. 1998, Pollock et al. 2006), is consistent with MT microspar forming as an *in situ* precipitate predominantly beneath the sediment-water interface. Several lines of evidence further constrain the timing of MTS formation. Compaction of host laminae around microspar-filled voids (Smith 1968; Fairchild et al. 1997; Pratt 1998, 2001; Pollock et al. 2006) (Figure 1.1*a*,*c*,*e*), for example, demonstrates that both voids and subsequent microspar formed prior to sediment compaction. Additionally, although much of the apparent folding of MT ribbons is best ascribed to reorientation of fractures as they formed within a rheologically variable substrate (Pollock et al. 2006), some folding (Smith 1968, Calver & Baillie 1990) and *en echelon* breakage (Fairchild et al. 1997, Pratt 1998) (Figure 1.1*c*) can be ascribed to deformation during, and thus formation prior to, substrate compaction.

More telling is the observation that fully lithified MTS is commonly ripped up and redeposited as syndepositional breccia deposits. Occasionally, sheet-like ribbons are reserved as remnants projecting upward from the scoured surface (cf. O'Connor 1972, Furniss et al. 1998, Pratt 1998) (Figure 1.1*e*); such remnants indicate that the hydraulic energy associated with breccia deposition was not always sufficient to fracture and remobilize all MTS in the excavated substrate. The frequent occurrence of such breccias within MTS-bearing strata further suggests that the hydraulic energy responsible for disruption was likely associated with relatively common events of moderate intensity. Together, these observations suggest that MTS formed, and was present as a fully lithified feature, within the shallowest regions of the unlithified sediment column.

The behavior of the microspar that fills MT voids provides additional insight into the timing of lithification of MTS. In a spectacular example, Pollock et al. (2006) illustrated a MT ribbon that crosscut a layer of detrital quartz sand (Pollock et al. 2006, figure 7; see also Pratt 2011). In this example, the quartz sand appears to have collapsed into the underlying MT void yet did not reach the bottom of the void because MT microspar had already filled the lowermost portion of the void, approximately 6mmbeneath the sand layer. Through most of the void, MT microspar is observed intermixed with sand grains until the void becomes, once again, filled with MT microspar above the quartz sand layer. This illustrative example suggests that precipitation of MT microspar was penecontemporaneous with the formation of MT voids. Although rare, MT microspar has also been observed as a supporting matrix phase in oolite (Pollock et al. 2006) and grainstone (Pratt 1998) lithologies, and as the primary matrix supporting broken and fragmented ribbons of MTS within fluidized beds (Stagner et al. 2004) (Figure 1.1*f*). The

occurrence of MT microspar as a primary component of matrix-supported facies requires that MT microspar could also precipitate within the water column, likely near the sediment-water interface. Taken together, these observations require MT voids to have formed in unlithified sediment, near the sediment-water interface, and suggest that MT microspar precipitated at or near the sediment-water interface at the time of void formation.

Potential Mechanisms of Molar-Tooth Structure Formation

Any satisfactory hypothesis for the origin of MTS must consider three fundamental observations regarding the nature of MT voids and their fill: (*a*) MTS formed during earliest postdepositional diagenesis in unlithified sediment near the sediment-water interface, (*b*) MT voids formed in a variety of coexisting morphologies, and (*c*) MT microspar precipitated in situ within MT voids penecontemporaneously with void formation. When placed into a larger context, hypotheses for the origin of MTS must also be consistent with the observed distribution of MTS in time and space (see Section 2.2). Explanations for the genesis of MTS, however, typically focus on either categorizing the macroscale morphology of MTS or exploring the mechanisms that drive void generation.

A biological origin

Some of the earliest hypotheses for the formation of MTS noted the unusual morphology of MTS and the finely crystalline nature of MT microspar and proposed a biological origin. These hypotheses interpreted MTS as either remnants of algal thalli or organosedimentary structures comparable to stromatolites (Smith 1968, O'Connor 1972). Bilaterally symmetric layering of MT microspar preserved in MTS within a discrete horizon of the Mesoproterozoic Atar Group [termed vermicular structures (Moussine-Pouchkine & Bertrand-Sarfati 1997)] was provided as evidence of a stromatolitic or algal origin, yet researchers also noted that MTS in underlying strata lacked this feature (Bertrand-Sarfati et al. 1997). With additional examination, however, it was determined that MTS was unlikely to be of biological origin. Horodyski (1976) argued that MTS in the Belt Supergroup was petrographically distinct from that which was observed in stromatolites, noting that when observed to co-occur, MTS crosscut stromatolites, indicating that MTS postdated stromatolite growth. Independently, Hofmann (1985) argued that the range of morphologies displayed by MTS is inconsistent with interpretations of MTS as algal thalli or fronds. Similarly, detailed petrographic analysis of vermicular structures from the Atar Group revealed that, despite internal lamination, these features were composed of stereotypical MT microspar, which led to their reinterpretation as deformed and brecciated MTS within seismically fluidized beds (Stagner et al. 2004, Kah et al. 2012).

An evaporite origin

An evaporative replacement model for the formation of MTS was initially favored by Eby (1975), who noted that evaporite phases, such as CaSO4, commonly show complex

intersecting and variable morphologies (cf. Warren & Kendall 1985, Cody & Cody 1988). Eby (1975) further noted that such soluble phases could readily have been replaced by a secondary carbonate microspar and that evaporite molds had been recognized in shallow marine carbonate strata of the Belt Supergroup that also contained MTS (cf. Pratt 2011). MTS, however, is not known to preserve evidence of either remnant or diagenetically replaced evaporite minerals (Pratt 2002, Bishop & Sumner 2006), and MT microspar lacks the petrographic characteristics of a replacement mineral phase (Pollock et al. 2006), making an evaporitic origin unlikely.

Formation via sediment shrinkage

The complex morphology of MTS, particularly the crenulation observed in many vertical ribbons, has also led to the hypothesis that MTSs are deformed mudcracks (Horodyski 1976, Demicco & Hardie 1994). Desiccation cracks are typically V-shaped in cross section, terminate downward while remaining open at the sediment-water interface, and are filled with sediment from above (Plummer & Gostin 1981). The complex morphologies observed in most MTS occurrences, as well as clear indication that MTS can terminate both downward and upward within the sediment package (Horodyski 1976), suggest that desiccation is an unlikely mode of origin. These observations led others to hypothesize that MTS represents intrastratal shrinking, or synaeresis (Young & Long 1977, Calver & Baillie 1990, Knoll & Swett 1990, Petrov 2011). Synaeresis refers to the spontaneous separation of the solid and liquid components of a gel upon standing (Jüngst 1934), but in a geological sense it refers to subaqueous volume loss and shrinkage of an unconsolidated sediment potentially driven by sediment shrinkage following the expulsion of interlayer water from clay lattices during changes in salinity (Plummer & Gostin 1981, Astin & Rogers 1991, Tanner 1998) or with volume loss associated with the microbial reduction of iron-rich smectite to illite during early diagenesis (Hodgskiss et al. 2018). Mechanisms that invoke intrastratal cracking such as synaeresis, however, still fail to explain the full range of morphologies displayed by MTS.

Formation via stress-induced cracking

Uncertainty regarding the potential drivers of synaeresis (Plummer & Gostin 1981, Tanner 1998, Harazim et al. 2013), combined with early hypotheses that MTS formed through postdepositional tectonic crumpling and segregation of thin calcite layers (Daly 1912, Fenton & Fenton 1937, Rezak 1957), spurred a series of models for MTS genesis that involved physical stress imparted to the substrate.

Like synaeresis, diastasis is a mechanism by which intrastratal fractures form in subaqueous environments via the differential effects of hydraulic shear on cohesive mud layers interbedded with unconsolidated sand (Cowan & James 1992). The idea that substrate rheology is important in the formation of substrate fractures was a key contribution of this work, and one echoed in later literature regarding MTS (Fairchild et al. 1997, Pollock et al. 2006, Long 2007, Smith 2016). Although diastasis is capable of producing doubly terminated intrastratal fractures, a diastasis mechanism does little to

explain the full range of morphologies exhibited by MTS or the presence of void filling microspar rather than void filled with detrital material from adjacent sedimentary layers (Smith 2016). Hydraulic energy, however, has been hypothesized to play a broader role in the formation of MTS in the form of cyclic wave loading, which could have enhanced fluid flow through crack networks and aided in the precipitation of microspar within MTS (Bishop & Sumner 2006, Bishop et al. 2006, Long 2007).

An additional subset of models relates the formation of MT voids, or more specifically the fracturing of sedimentary substrates, to stresses capable of inducing liquefaction of the substrate, such as those related to hydraulic loading during storms and tsunami events, or seismic shaking. In these models, fractures are caused by a combination of substrate liquefaction (Bertrand-Sarfati et al. 1997, Fairchild et al. 1997, Moussine-Pouchkine & Bertrand-Sarfati 1997, Kah et al. 2007), fluidization, and dewatering (Qiao et al. 1994; Pratt 1998; Du et al. 2001; Pratt 2001; Jia et al. 2003, 2011), followed by deformation during sediment compaction. While some authors recognize that these hypotheses do not provide a mechanism for filling substrate voids with MT microspar (Fairchild et al. 1997), others suggest that the characteristic microspar associated with MTS originated within the host rock and was hydrodynamically sorted during fluidization, with microspar migrating (Pratt 1998, 2011) or being injected (Qiao et al. 1994) into cracks from the surrounding substrate. This model appears unlikely given the distinct petrographic character of MT microspar (Pollock et al. 2006, Kuang 2014) and is difficult to reconcile with instances of MTS that form within lithologies that lack lime mud (Bishop & Sumner 2006).

Formation via gas expansion and migration

To better explain the full diversity of shape recorded by MTS and its persistent association with MT microspar, more recent efforts have focused on the potential for MTS formation via migration of gases within the substrate. The idea of gas expansion and migration was first proposed to explain the occurrence of spheroidal blebs that are conspicuous elements of the MTS preserved in the Belt Supergroup (Eby 1975, Furniss et al. 1998). In this model, metabolic reactions associated with microbial decomposition of organic matter in the substrate (Young & Jefferson 1975, Horodyski 1976) produce voids via gas expansion (blebs) and migration (cracks), while simultaneously contributing to changes in fluid chemistry that could drive microspar precipitation (cf. Furniss et al. 1998, Higgins et al. 2009, Bergmann et al. 2013). Gas expansion and migration have been demonstrated to produce a wide array of void morphologies, similar to that observed in MTS, in both modern environments (Winston et al. 1999, Miller et al. 2018) and experimental simulations (Furniss et al. 1998, Boudreau 2012).

A gas expansion and migration model is compelling because it can satisfactorily explain a wide variety of void morphologies by a single mechanism, and because it provides a mechanism to produce voids within the shallow substrate, near the sediment-water interface, which is consistent with the inferred environments and timing of MTS formation. Linking a gas expansion model to the physical properties of the substrate, Pollock et al. (2006) proposed that the complex morphology of MTS was determined

largely by the balance between gas production and the strength of the surrounding substrate, and they predicted that MTS morphology would vary across distinct substrate facies. Documentation of discrete relationships between the morphology of MTS and changes in the lithologic character of the substrate (Pollock et al. 2006; cf. Pratt 1998, 2011; Bishop & Sumner 2006; Kuang 2014) further supports a gas expansion and migration model.

The composition of gases responsible for MTS, however, remains poorly constrained. It is generally accepted that gases responsible for the formation of MTS are related to microbial activity at the sediment-water interface and within the shallow substrate (cf. Frank & Lyons 1998, Shen et al. 2016, Strauss & Tosca 2020), either as substrate-produced gasses or from the explosive destabilization of CO_2 clathrates within the sedimentary substrate (Marshall & Anglin 2004). Microbial communities at the sediment-water interface and within the shallow subsurface exploit substantial gradients in pH, redox, and ionic composition (Morse & Mackenzie 1990, Santschi et al. 1990, Nealson 1997) that are reflected in depth-dependent production of substrate gasses including CO_2 (associated with the microbial oxidation of organic matter), H_2S (associated with microbial sulfate reduction), and CH_4 (associated with methanogenesis). Of these different metabolic processes, microbial sulfate reduction—along with associated iron and manganese reduction—is also associated with local increases in alkalinity that favor carbonate precipitation (cf. Bergmann et al. 2013). Assessment of the C isotope composition of MT microspar, however, does not reveal either ^{13}C-depleted or ^{13}C-enriched values that would be expected from either sulfate reduction or methanogenesis, respectively (Frank & Lyons 1998), which has led to little consensus as to the specific gas responsible for MTS formation. Despite such uncertainty, a gas expansion and migration model has generally been accepted as the most plausible mechanism for the formation of MTS (Kuznetsov 2003, Pope et al. 2003, Long 2007, Mei & Tucker 2011, Kuang 2014, Smith 2016).

Petrography of Molar-Tooth Structure

Petrographic Characteristics of Molar-Tooth Structure

Field observations of MTS record a dazzling array of complex and diverse morphologies, typically with sharp contact between MTS and host rock. Petrographic analysis with transmitted light microscopy supports that MT microspar is readily distinguishable from the fine-grained carbonate that usually comprises the sedimentary matrix of MTS (cf. Pratt 1998, Marshall & Anglin 2004, Bishop & Sumner 2006, Pollock et al. 2006, Long 2007). MT microspar is composed of uniform, equant, limpid crystals, averaging ~15 μm in diameter, that show generally planar, noninterlocking crystalline boundaries (Figure 1.3); these basic characteristics are shared regardless of the age, host rock lithology, or geographic locality of the occurrence. Crystal Size Distributions (CSDs) of MT microspar (Kile et al. 2000; Kile & Eberl 2003; Crawford & Kah 2004; A. Kriscautzky, unpublished data) are consistent with an interpretation that MT microspar formed via decay-rate nucleation and constant growth, with only minimal Ostwald ripening (Kile & Eberl 2003) (see sidebar titled Crystal Size Distributions).

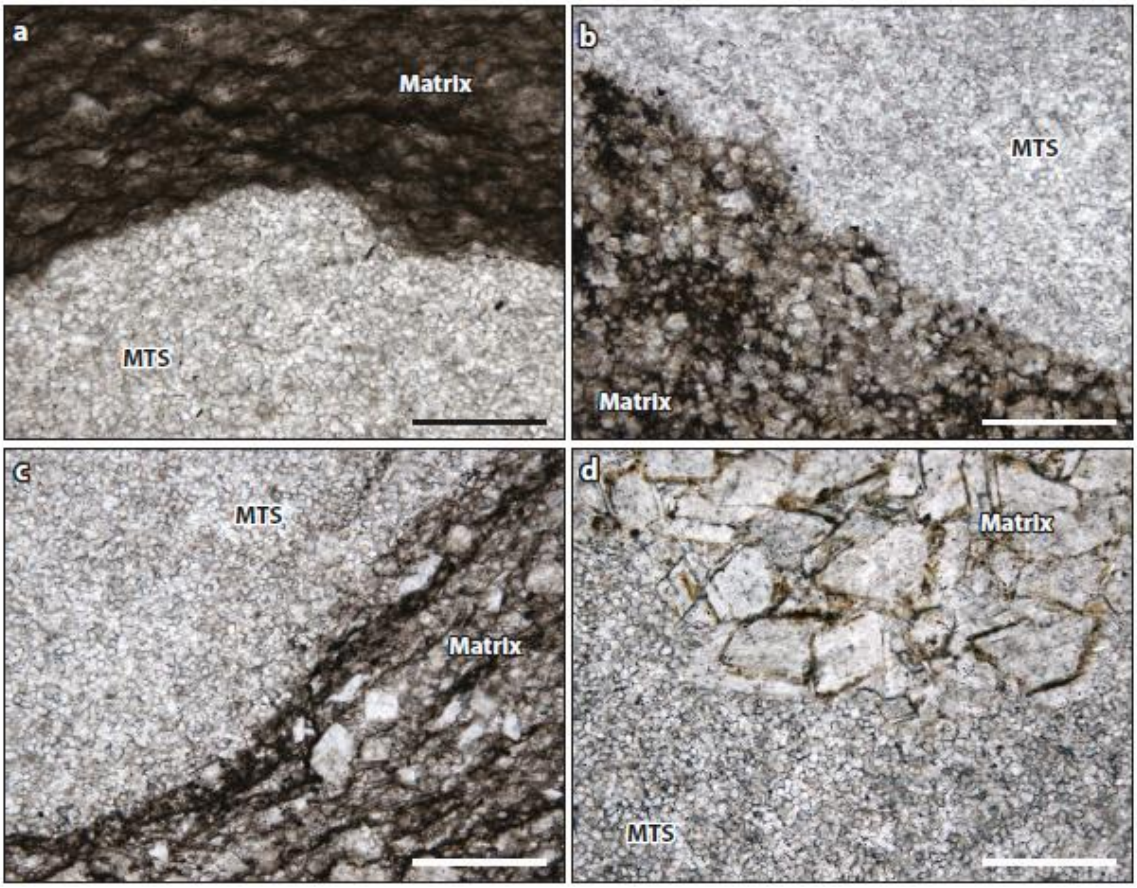


Figure 1.3. Petrographic character of MT microspar. In plane light, MT microspar (MTS) consists of characteristically homogeneous, equant, limpid crystals, regardless of the composition and diagenetic history of the host sediments (matrix). MT microspar and matrix are typically separated by a sharp boundary. (*a*) Mesoproterozoic Belt Supergroup, USA. (*b*) Mesoproterozoic Bylot Supergroup, Arctic Canada. (*c*,*d*) Mesoproterozoic Atar Group, Mauritania. The scale bar is 50 μm in all panels.

By contrast, the petrographic character of the sedimentary matrix of MTS is variable, both within individual occurrences and across time and space. The carbonate matrix that hosts MTS commonly contains substantial amounts of organic matter, clay, and quartz silt (Figure 1.3*a*–*c*). Carbonate within the matrix phase also preserves a much larger range of crystal sizes; these crystals are typically cloudy in appearance and have nonplanar crystal boundaries, indicating substantial neomorphic recrystallization. In other cases (Figure 1.3*d*), matrix carbonate is dolomitized and can consist largely of secondary, fabric-destructive, euhedral (often zoned) dolomite rhombs, even as MT microspar remains calcite.

Cathodoluminescence Characteristics of Molar-Tooth Structure

Cathodoluminescence (CL) petrography, which provides visual evidence of chemical differences between carbonate phases based on the relative incorporation of iron and manganese in the carbonate lattice, underscores the distinction between MT microspar and matrix carbonate phases (Figure 1.4) (see sidebar titled Cathodoluminescence). Under CL, MT microspar crystals consist of nonluminescent to dully luminescent cores (averaging ~8 μm in diameter) surrounded by more brightly luminescent rims (averaging ~3 μm in thickness); these basic characteristics are shared regardless of the age or geographic locality of the sample (Pollock et al. 2006, Kuang 2014, this study). The two-phase construction of MT microspar is not apparent by standard petrographic methods because core and rim phases are in crystallographic continuity and therefore optical alignment. The two-phase character of MT microspar has also been recognized during scanning electron microscopy (SEM) (Bishop & Sumner 2006), wherein compositional differences between core and rim phases affect the intensity of electron backscattering. Because of the distinctive nature of MT microspar, cathololuminescence microscopy reveals features that are not distinguishable via standard petrographic methods. In addition to revealing the two-phase nature of MT microspar, CL permits (*a*) detection of MT microspar in matrix phases, (*b*) recognition of variation in the structural details of MT microspar, and (*c*) identification of complex depositional and diagenetic processes that affect MT microspar.

As with petrographic relationships observed in plane light, we have observed that the luminescence character of MT microspar contrasts sharply with carbonate crystals within the sedimentary substrate, which typically display greater variability in grain size and grain shape, and which show variably dull to bright luminescence and may contain an array of euhedral dolomite rhombs with complex zonation, indicating a complex and multistage diagenetic history (Figure 1.4). The two-phase construction of MT microspar, however, also permits identification of microscale relationships between MTS and matrix sediment. For instance, although MT microspar occurs primarily within MT voids, it may also form a subsidiary phase within host lithologies, occurring as individual crystals (Figure 1.4*a*,*b*) to small patches (Figure 1.4*c*). The observation that MT microspar occurs as a distinct phase within matrix components was previously used to interpret MT microspar as a fine-grained detrital component that was mechanically segregated from the sediment matrix and transported to MT voids during seismic shaking and liquefaction

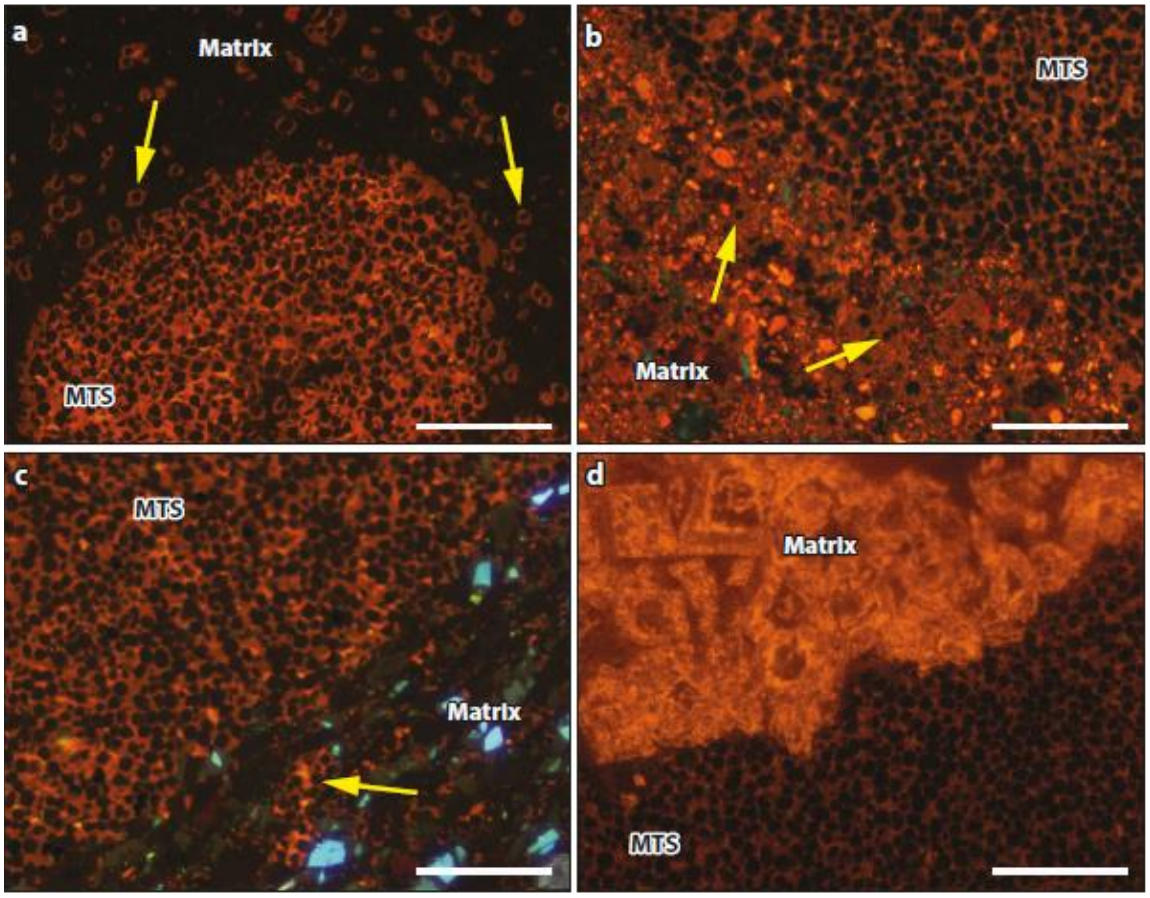


Figure 1.4. Petrographic character of MT microspar. Under cathodoluminescence, MT microspar (MTS) shows a characteristic two-phase structure consisting of dully luminescent cores and more brightly luminescent rims that are in optical continuity. MT microspar is similar, regardless of the petrographic character of host sediments (matrix). This two-phase structure permits identification of small pockets of MT microspar and individual MT microspar crystals (*arrows in panels a–c*) that are commonly unidentifiable in plane light. Samples are the same as shown in Figure 1.3. (*a*) Mesoproterozoic Belt Supergroup, USA. (*b*) Mesoproterozoic Bylot Supergroup, Arctic Canada. (*c*,*d*) Mesoproterozoic Atar Group, Mauritania. The scale bar is 50 μm in all images.

(Pratt 1998). The two-phase nature of the microspar, however, requires the MT cores to have been free of contact with other substrate particles prior to formation of MT rims and supports formation of MT microspar via in situ precipitation in pore spaces within the sediment matrix, consistent with the interpretation of MT microspar as a cement phase (Frank & Lyons 1998, Pollock et al. 2006).

CL petrography also permits identification of discrete variants of MT microspar—both within and across samples from different localities and ages. Most commonly, differences occur in the relative ratio of core and rim phases, but differences are also observed in the character of the MT microspar itself. As described above, the archetypal MT microspar consists of dully luminescent, subspherical cores with more brightly luminescent rims that directly surround the cores (cf. Pollock et al. 2006) (Figure 1.5*a*). Here we identify previously undocumented variation in which MT cores also occur as rhombs with discrete, luminescent rims that directly surround the rhombic cores (Figure 1.5*b*); as subspherical cores that show internal zoning under CL (Figure 1.5*c*); or even as subrhombic cores that preserve a discretely crescent-shaped luminescent phase that sits between core and rim phases (Figure 1.5*d*).

CL petrography also highlights the inherent complexity of MTS (Figure 1.6) by enabling the recognition of multiple stages of MT microspar within single samples. For instance, in outcrop, MTS is commonly described as complex networks containing a single phase of MT microspar (cf. Pratt 1998, Long 2007); under CL, it becomes apparent that only some networks have a continuous, single generation of MT microspar. Here we show that discrete phases of MT microspar can be readily identified under CL by differences in the size of microspar cores, the size ratio of core to rim phases, and the morphology of MT cores (cf. Stagner et al. 2004) (Figure 1.6*a*–*c*).CL petrography also permits identification of MT microspar alteration, specifically in rock samples that have undergone multiple stages of diagenesis. In these cases, single continuous phases of MT microspar can vary spatially between regions with a typical core and rim structure and regions where more rhombic cores are surrounded by multiple secondary phases of carbonate (Figure 1.6*c*,*d*). In these cases, MT microspar—as either individual cores or core-rim pairs—often occurs as the nucleus of secondary phases, resulting in dominance of a coarsely crystalline regions. Such alteration is not always apparent using standard petrographic methods, both because some original MT microspar is preserved and because later episodes of diagenetic carbonate formation commonly occur in optical alignment with preexisting cores. Interestingly, in diagenetically overprinted examples, cores (and less frequently rims) may also be preserved within secondary phases. Preservation of individual microspar elements is most obvious within large dolomite rhombs, where individual cores or core-rim pairs with distinct cathodoluminescent character are observed within secondary crystals (Figure 1.6*e, f*).

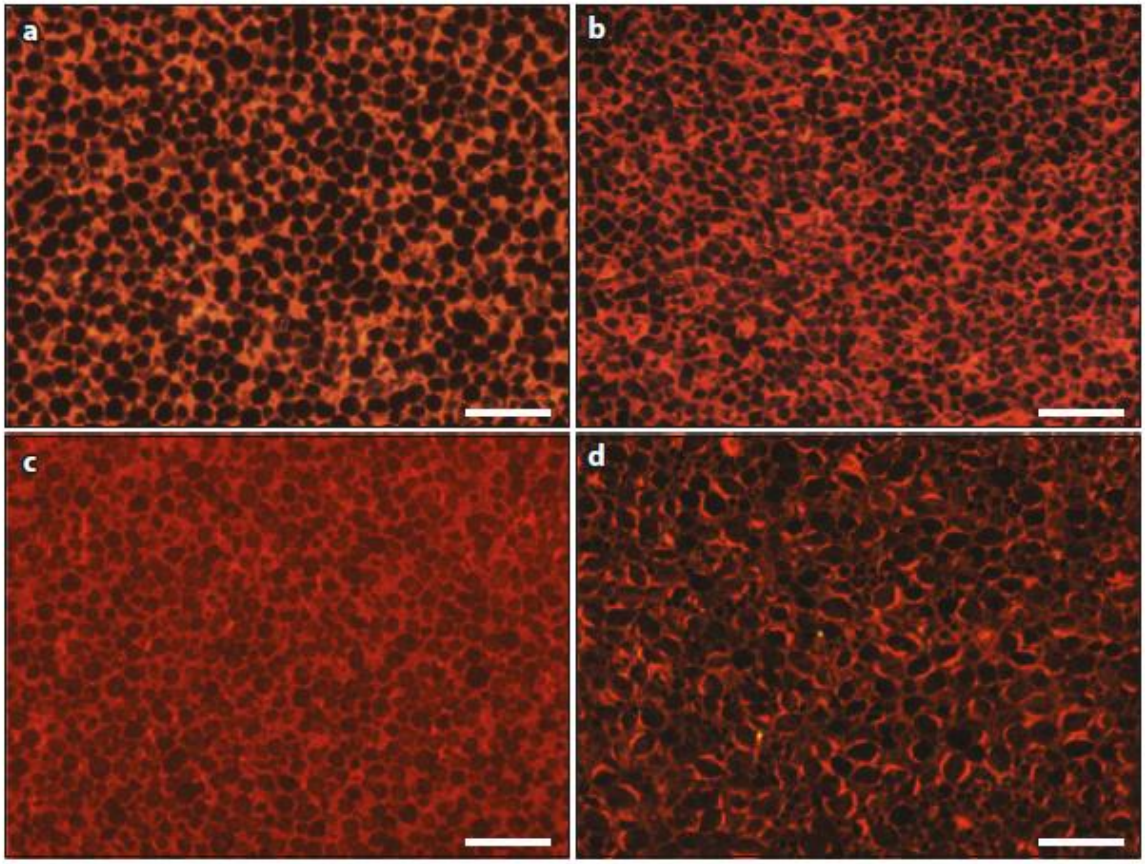


Figure 1.5. Cathodoluminescence highlights variability in MT microspar cores. (*a*) Largely rounded, dully luminescent cores; Mesoproterozoic Atar Group, Mauritania. (*b*) Largely rhombic, dully luminescent cores; Mesoproterozoic Atar Group, Mauritania. (*c*) Rounded, polygonal, and rhombic MT microspar cores that display internal zoning; Mesoproterozoic Kaltasy Formation, Russia. (*d*) Dully luminescent ellipsoidal rhombs with a secondary, brightly luminescence phase that appears as crescents along the long edges of the rhombs; Neoproterozoic Jiangsu Province, China. The scale bar is 25 μm in all images.

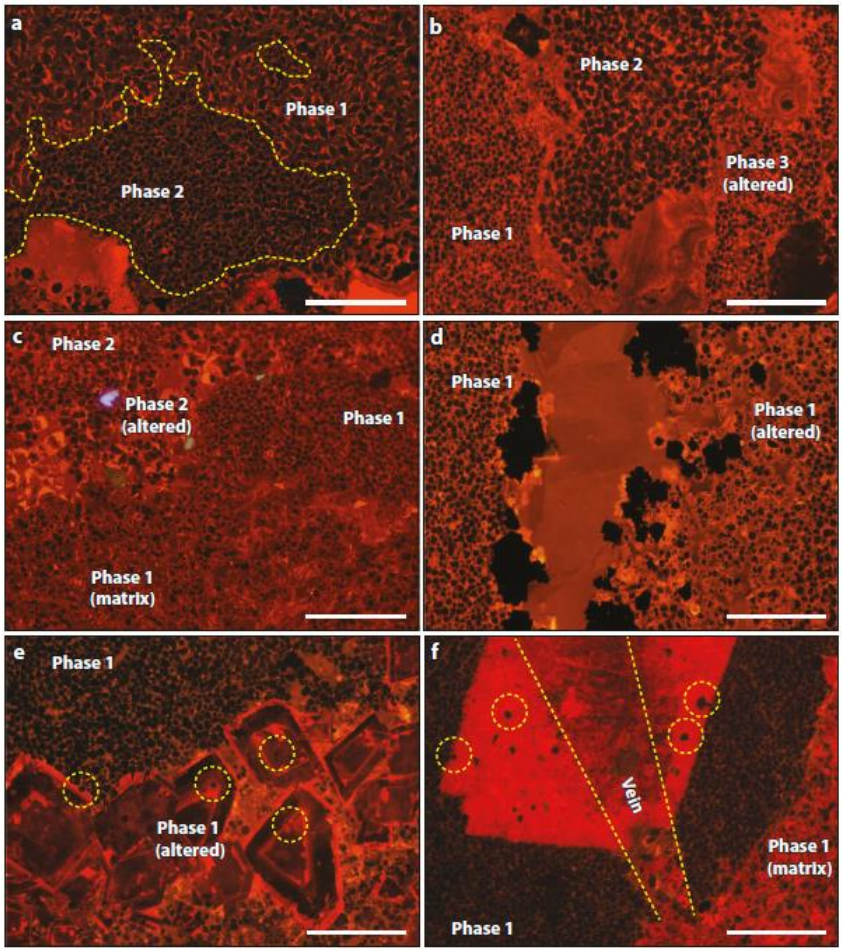


Figure 1.6. Cathodoluminescence highlights a complex depositional and diagenetic history of MT microspar. (*a*) Juxtaposition of discrete phases of MTS formation (*dotted line*), characterized by MT microspar with distinct crystal sizes and diagenetic histories; Neoproterozoic Jiangsu Province, China. (*b*) Three phases of MT microspar formation showing distinct differences in core size and shape; Mesoproterozoic Atar Group, Mauritania. (*c*) Multiple discrete phases of MT microspar showing differences in core size and shape, and the degree of secondary carbonate mineralization; Mesoproterozoic Atar Group, Mauritania. (*d*) A single episode of MT microspar precipitation that varies from little altered cores and rims to remnant cores encased in multiple stages of secondary carbonate precipitation; Mesoproterozoic Belt Supergroup, Montana. (e) A single episode of MT microspar precipitation that varies from little altered cores and rims to remnant cores encased in secondary carbonate precipitation. Later dolomitization further destroys primary MT microspar while preserving rare microspar cores during dolomite growth (*circles*); Mesoproterozoic Bylot Supergroup, Arctic Canada. (*f*) A single episode of MT microspar precipitation that records little altered cores and rims within a MT ribbon, altered cores embedded within strongly recrystallized MT matrix, and further recrystallization during late-stage vein formation and secondary recrystallization that preserves rare microspar cores and rims within a single, large, fabric-destructive dolomite rhomb; Neoproterozoic Anhui Province, China. The scale bar is 50 μm in all images.

DISCUSSION

Environments of molar-tooth structure genesis

As outlined above, a variety of mechanisms can result in void genesis in unlithified fine-grained sediment, and it cannot be ruled out that multiple processes might have produced voids associated with MTS. The morphological variability of MTS and the unique association between voids and microspar fill, however, favor a single mode of origin. Of the mechanisms that have been explored to date, gas production, expansion, and migration (Furniss et al. 1998, Pollock et al. 2006) best explain the range of morphologies observed in MTS occurrences and their relationship to host lithologies. Microbial activities associated with a gas expansion hypothesis also provide a mechanism for driving the synsedimentary precipitation of microspar that is critical to the preservation of MTS (Fairchild et al. 1997, Pope et al. 2003, Pollock et al. 2006) via increases in alkalinity (Frank & Lyons 1998, Hodgskiss et al. 2018) or the production of dissolved, colloidal, and particulate organic carbon (cf. Santschi et al. 1990) that may have fostered carbonate nucleation in supersaturated pore fluids (cf. Pollock et al. 2006).

It has long been argued that the temporal and spatial distribution (Figure 1.2) of MTS is a consequence of long-term evolution in carbonate saturation state (Grotzinger 1989, Bartley & Kah 2004), which controls both the rate of lithification of fine-grained sedimentary rocks and the geochemical conditions favorable to the formation of MT microspar. The genesis of MTS in any given environment is governed, firstly, by the ability to form cracks and voids within the substrate and, secondly, by the capacity for synsedimentary precipitation of carbonate microspar within those voids. Rapidly lithified carbonate substrates typical of elevated marine carbonate saturation in the Archean and Paleoproterozoic (Grotzinger 1990, Cantine et al. 2019) would likely have been too brittle to permit formation of complex void morphologies characteristic of MTS. Indeed, most of the early examples of MTS occur within fine-grained siliciclastic facies (Bishop & Sumner 2006, Bishop et al. 2006), which likely lithified more slowly than their carbonate counterparts. By contrast, the relative paucity of MTS in the later Neoproterozoic is consistent with carbonate saturation states insufficient to induce calcite precipitation within MT voids (Kah & Knoll 1996, James et al. 1998)—a situation that might be exacerbated by the increasingly oxic character of the seafloor, which would further drive a reduction in local carbonate saturation (Sumner & Grotzinger 1996, Higgins et al. 2009, Cantine et al. 2019, Present et al. 2021).A peak abundance of MTS between 1.2 and 0.8 Ga therefore suggests that this time interval sat at a critical environmental threshold where carbonate saturation was insufficient to result in widespread rapid lithification of the substrate, but where minor perturbations in the physiochemical environment could locally enhance carbonate saturation and drive synsedimentary precipitation of MT microspar (Frank & Lyons 1998, Pollock et al. 2006, Hodgskiss et al. 2018, Kah & Bartley 2021).

The environmental distribution of MTS also provides a key set of observations for understanding the origins of MT microspar. In addition to its temporal distribution, MTS occurs most frequently in intertidal to shallow subtidal environments (James et al. 1998, Kuang 2014) and is typically absent from both evaporitic settings that contain evidence for

rapid lithification of the sedimentary substrate (cf. Bartley et al. 2000, Kah et al. 2001) and deeper-water environments, except when associated with carbonate concretions (cf. Pope et al. 2003; A. Kriscautzky, unpublished data). Furthermore, within these environments, MTS forms at or near the sediment-water interface. Together, these observations underscore the potential importance of the interplay between ambient seawater chemistry and microbial modification of shallow subsurface porewaters in the genesis of MTS (cf. Frank & Lyons 1998, Shen et al. 2016, Hodgskiss et al. 2018).

The sediment-water interface is a biologically active zone, and geochemical conditions can change dramatically over short spatial scales (cf. Santschi et al. 1990, Canfield & Des Marais 1993, Walter et al. 1993, Nealson 1997). A typical Mesoproterozoic to early Neoproterozoic seafloor would have been overlain by carbonate-saturated seawater and contain a boundary zone that extended from just above to just below the sediment-water interface and through which oxygen levels would have decreased rapidly. In the absence of bioturbation, microbial activity would have rapidly consumed free oxygen within the upper few millimeters of the sediment column, resulting in porewaters that were both carbonate saturated and anoxic, and whose local trace element chemistry would be strongly linked to the microbial redox ladder (Bethke et al. 2011). Geochemical analysis of marine carbonate rocks also indicates that the Mesoproterozoic and early Neoproterozoic seafloor was variably oxic, dysoxic, euxinic, and ferruginous (cf. Lyons et al. 2009). Such a wide array of redox states at the sediment-water interface would result in a spatial distribution of the dominant microbial processes occurring in the shallow substrate and at the sediment-water interface. This variability would, in turn, affect the alkalinity and concentration of dissolved inorganic carbon (DIC)—and therefore the pH and carbonate saturation state—of local porewaters (Soetaert et al. 2007). Specifically, microbial manganese and iron reduction strongly elevate carbonate saturation, while denitrification, sulfate reduction, and anaerobic oxidation drive carbonate saturation only moderately higher (Bergmann et al. 2013). In addition, during these microbial processes the decomposition of organic matter, particularly extracellular polymeric substances, would release cations and DIC to porewater fluids, further promoting carbonate precipitation (Dupraz & Visscher 2005).

Genesis of molar-tooth microspar

Environmental conditions of the Mesoproterozoic and early Neoproterozoic eras, in which ambient seawater was highly saturated with respect to the precipitation of calcium carbonate and microbial activity within the shallow substrate could plausibly result in an additional increase in carbonate saturation, favored the rapid lithification of substrate voids. Luminescence characteristics suggest that MT microspar originated as micrometer-scale, spheroidal particles (cores) that remained in suspension within voids prior to precipitation of overgrowth phases (rims). Such a morphology is consistent with hypotheses that MT microspar may have initially precipitated as an amorphous calcium carbonate (ACC) phase (Goodman & Kah 2007, Smith 2016, Strauss & Tosca 2020, Roest-Ellis et al. 2021). ACC commonly forms in association with highly hydrated gels, within which initially spheroidal ACC rapidly converts to crystalline mineral phases (Bots et al. 2012, Ihli et al. 2014, Carino

et al. 2017). Following earlier experimental production of MT microspar (Goodman & Kah 2007), here we argue that a combined ACC-gel phase is consistent both with the observed two-phase construction of MT microspar and with the morphological variation observed across MT microspar occurrences. In this scenario, dully luminescent cores observed within MT microspar represent the initial ACC phase, and more brightly luminescent rims reflect carbonate precipitation associated with the gel phase. CSDs of MT microspar also record patterns of nucleation and growth that are consistent with the rapid onset and exponential decay of nucleation, diffusion-limited growth, and minimal Ostwald ripening that might be expected from an ACC-gel phase (Crawford et al. 2006). CSDs similar to those observed for MT microspar (Crawford & Kah 2004, Crawford et al. 2006) have been observed experimentally only in fluids with strongly elevated carbonate saturation [_>70 (Kile et al. 2000, Kile & Eberl 2003)], which exceeds the saturation state required for precipitation of ACC (Evans et al. 2019, 2020; Purgstaller et al. 2019). The hypothesis the MT microspar initiated as an ACC-gel phase can further be refined by observations that (*a*) the host substrate of MTS remained relatively unlithified, indicating insufficient carbonate saturation to support penecontemporaneous cementation of the substrate, and (*b*) MT microspar does not preserve carbon isotope signatures that can be linked directly to substrate microbial processes, suggesting marine waters are the dominant contributor to DIC. Taken together, these observations support the hypothesis proposed here that mixing of highly saturated surface waters with high alkalinity porewaters resulted in a rapid increase in local carbonate saturation, driving the nucleation and precipitation of MT microspar within MT voids. In this scenario, MT microspar clearly represents a cementing phase, even as it lacks fabrics typical of a void-filling carbonate cement, such as crystal orientation perpendicular to void walls, competitive growth boundaries, or inward-increasing grain size.

Stabilization of molar-tooth microspar

The recognition that MT microspar likely originated as ACC (Goodman & Kah 2007), which would have rapidly evolved to micritic crystalline carbonate, also provides a framework for interpreting the variable petrographic and CL character of MT microspar. In much the same way that diagenesis in Phanerozoic carbonate rocks can be inferred by using the petrography of well understood skeletal microfabrics (cf. Bruckschen et al. 1995), MT microspar provides an end member state for analysis of its precipitation and recrystallization pathway; such petrographic end members are rare in the Precambrian, particularly for facies without clear modern analogs. We propose here that once voids opened within the shallow subsurface, creating a network of MTS, new pore space filled with a mixture of fluids from both the sediment-water interface and sediment porewaters. These fluid interactions then triggered production of an ACC-gel phase—a colloidal semisolid that both preserved open voids associated with MTS and allowed the cores of MT microspar to remain suspended within MT voids. Initial ACC then dehydrated, rapidly transforming to a stable calcite phase, potentially via one or more unstable calcium carbonate polymorphs such as vaterite or aragonite (Pollock et al. 2006, Bots et al. 2012).

Inference of a gel phase associated with ACC precipitation derives directly from the two-phase structure of MT microspar and provides critical insight, as well, into the origin of its luminescence characteristics. ACC is highly hydrated and therefore has a greater surface area than traditional crystalline carbonate polymorphs. Experimental work has determined that an amorphous framework can both adsorb and structurally accommodate elements with larger ionic radii than Ca^{2+} (Littlewood et al. 2017), including typically incompatible elements at higher concentration than their crystalline counterparts (Rimstidt et al. 1998, Matsunuma et al. 2014). Backscattered electron microscopy (Bishop & Sumner 2006), secondary ion imaging (Crawford et al. 2006), and CL observations (Pollock et al. 2006, this study), show a clear two-phase structure of MT microspar. MT cores of various shapes are typically dully luminescent and contrast sharply with crystallographically coherent, yet chemically variable, luminescent rims. As with clearly diagenetic phases, such as dolomite rhombs that also show sharp zonation (Lee et al. 2018), these features are consistent with trace element partitioning between initial ACC, which is represented by the core of MT microspar, and a gel phase, which is represented by the rim phase of MT microspar. In this hypothesized scenario, as the ACC crystallizes, it dehydrates and expels trace elements such as Mn^{2+} and Fe^{2+} from the emerging crystalline phase (Rimstidt et al. 1998), thus increasing the concentration of these elements in the gel/fluid phase that surrounds the microspar cores. As rims develop, they adopt trace element characteristics inherited from this gel phase, producing distinctly bright luminescence, characteristic of elevated ratios of Mn^{2+} to Fe^{2+} (Hemming et al. 1989, Savard et al. 1995). SEM-EDS analysis (Bishop & Sumner 2006) also records elevated concentrations of Mn^{2+}, along with Fe^{2+} and Mg^{2+}, in rim phases. Partitioning of trace elements between ACC and the surrounding gel phase may also have been affected by the presence of organic acids within substrate porewaters, which reduce the incorporation of Mn^{2+} into ACC (Evans et al. 2020) and would result in preferential partitioning of Mn^{2+} into the gel phase.

A two-phase CL structure of MT microspar could plausibly arise from changes in redox state wherein microspar cores precipitate from an initially oxic fluid, and microspar rims precipitate as the fluid within MT voids becomes progressively more reduced. We suggest, however, that this scenario is unlikely because divalent Mn—the main activator of luminescence in carbonate phases—is readily exported from anoxic pore fluids to overlying oxic waters where it can be incorporated into precipitated carbonate phases (Sundby & Silverberg 1985, Thamdrup et al. 1994). Active transport of redox-sensitive phases across the sediment-water interface would inhibit the small-scale segregation of chemistry implied by the CL structure of MT microspar. By contrast, the model presented here predicts that trace element zonation is a direct consequence of the process of precipitation and neomorphic stabilization of MT microspar within a primary gel phase. In this scenario, although none of the individual phases within the microsparitic cement reflect precipitation directly from unmodified seawater, the combined mixture of core and rim phases would be expected to reflect the ambient fluid (i.e., marine and porewater mixture) from which the microspar precipitated.

Once precipitated, MT microspar stabilization appears to proceed via one of a number of specific pathways, resulting in the range of textures observed under CL. We

consider that the key step to the lithification of MTS was the precipitation of rim phases of MT microspar, and we observe several distinct textures that plausibly reflect differences in the timing of stabilization of MT cores relative to precipitation of rim phases. In the first case, unzoned spheroidal cores are directly surrounded by syntaxial cement (Figure 1.5*a*), which we interpret as reflecting rim formation simultaneous with ACC dehydration. This texture likely reflects the highest local carbonate saturation, and the growth of syntaxial rims during ACC dehydration would constrain the morphology of the core phase. In the second case, rhomb-shaped euhedral cores (Figure 1.5*b*), wherein the presence of sharp crystal faces reflects growth in an unconstrained environment, suggest that conversion of ACC to crystalline calcium carbonate occurred prior to precipitation of the rim phase. Later precipitation of rims relative to core stabilization suggests that this texture reflects ambient void-filling fluids that were less strongly saturated with respect to calcium carbonate. In this scenario, as cores convert from the amorphous state, expulsion of divalent cations from the carbonate crystal lattice would increase the saturation state of the surrounding gel/fluid, driving rim precipitation. In a third texture, largely spheroidal cores possess internal zonation visible under CL (Figure 1.5*c*). We propose that this texture results from recrystallization of the core phase after both initial dehydration and development of the rim cement. In this case, precipitation of rim cement at the latest stages of ACC dehydration constrains the shape of the core during later recrystallization, and fine-scale dissolution and reprecipitation of the core phase results in internal zonation. Finally, in an unusual fourth texture, cores are surrounded by crescent-shaped domains of brightly luminescent calcite, which together form broadly spheroidal morphologies (Figure 1.5*d*). This texture is best explained by formation of rims in the earliest stages of ACC conversion, which would be expected to constrain the morphology of cores during conversion of ACC to crystalline calcium carbonate. In this case, however, the main stage of ACC dehydration and mineralogical stabilization postdates rim formation, and volume loss during recrystallization of ACC would result in crescent-shaped voids developing between the core and the innermost portions of the rim. Water released during core dehydration would then remain trapped within the rim and become strongly enriched in trace elements expelled from the core phase during recrystallization. In this example, MT microspar reveals three distinct generations of carbonate precipitation (core, rim, and crescent-shaped domains) that precipitate in crystallographic and optical continuity, but whose trace element concentration is controlled by both the initial partitioning of ions between ACC and an initial gel phase, and then by the expulsion of cations during recrystallization of ACC. In all these cases, once stabilized, MT microspar appears to be substantially resistant to further water-rock interaction, resulting in preservation of a unique textural record of carbonate precipitation and its earliest diagenesis.

Molar-tooth microspar as a target for geochemical analysis

The hypothesis outlined above defines MT microspar as an early diagenetic cement that preserves micrometer-scale heterogeneity resulting directly from its mode of formation. With possible rare exception (cf. Stagner et al. 2004, Pollock et al. 2006), MT cement does not appear to precipitate from unmodified seawater but rather reflects a

mixture of both highly saturated, ambient seawater and shallow subsurface porewaters that have been modified by microbial activity. MT microspar also preserves, on the scale of micrometers to tens of micrometers, distinct luminescence characteristics that we hypothesize to reflect partitioning of trace elements during precipitation and stabilization of calcium carbonate in a closed system. Whereas it is likely that the average composition of MT cement approximates the isotopic and elemental composition of the fluid from which it formed, we argue that the precipitation of MT microspar requires a mixture of seawater and modified porewaters, making it perilous to directly equate the composition of MT microspar with seawater composition.

The distinctive two-phase construction of MT microspar, however, makes it possible to evaluate the degree of fluid-rock interaction during later-stage diagenesis. Backscatter SEM images document sharp differences between cores and overgrowths on a spatial scale of less than 500 nm, suggesting that significant cation exchange could not have occurred at scales greater than hundreds of nanometers (Bishop & Sumner 2006).We therefore expect that sampling of petrographically pristine MT microspar will provide a chemical composition that reflects the original mixture of local marine waters and sedimentary porewaters, and that chemical preservation likely extends to isotopic measurements, as proposed for other early stabilized Precambrian fabrics (Kaufman et al. 1991, Frank et al. 2003, Bartley et al. 2007).We have shown, however, that despite the generally well-preserved nature of MTS, MT microspar is not exempt from later diagenetic recrystallization (Figure 1.6). Like other traditional targets for geochemical characterization, fidelity of preservation must be established petrographically for each sample to assess the degree of postdepositional diagenesis prior to interpretation of chemical signals.

CONCLUSIONS

- Molar-tooth structure (MTS) is a complex fabric that consists of both a network of morphologically diverse voids and a microspar cement that fills those voids. Molar-tooth (MT) voids formed in the shallow portions of the sediment column, likely via gas expansion and migration. MT microspar is composed of spheroidal to rhombic cores and syntaxial overgrowths and precipitated from a mixture of seawater and pore fluids modified by microbial processes.
- Cathodoluminescence microscopy reveals a high degree of small-scale heterogeneity in MT microspar that records the earliest stages of mineral precipitation, stabilization, and neomorphism, during which MT microspar evolved from an amorphous calcium carbonate precursor.
- The preservation of stereotypical micron-scale distinctions between cores and rims demands that well-preserved MT microspar has undergone relatively little postdepositional diagenesis, and that original trace element and isotopic compositions likely record initial chemical conditions.
- When late-stage diagenesis disrupts primary micron-scale patterns, it leaves a telltale petrographic record. Like other early stabilized fabrics, fidelity of preservation must be established petrographically for each sample to assess the degree of postdepositional

diagenesis, and MT microspar cannot be used indiscriminately as a proxy for seawater chemistry.

AKNOWLEDGEMENTS

I thank the Geological Society of America and the Sedimentary Geology Division of the Geological Society of America. Linda C. Kah and Julie K. Bartley. thank the National Aeronautics and Space Administration, the National Science Foundation, and the National Geographic Society for funding previous field work.

We would like to thank Annual Review of Earth and Planetary Sciences for the invitation to publish this work in volume 50, along to the editorial board and the anonymous reviewers that have improved this manuscript.

REFERENCES

Astin, T., Rogers, D., 1991. “. "Subaqueous shrinkage cracks" in the Devonian of Scotland reinterpreted. Journal of Sedimentary Research 61, 850-859.

Bartley, J.K., Kah, L.C., 2004. Marine carbon reservoir, Corg-Ccarb coupling, and the evolution of the Proterozoic carbon cycle. Geology 32, 129-132.

Bartley, J.K., Kah, L.C., McWilliams, J.L., Stagner, A.F., 2007. Carbon isotope chemostratigraphy of the Middle Riphean type section (Avzyan Formation, Southern Urals, Russia): Signal recovery in a fold-and-thrust belt. Chemical Geology 237, 211-232.

Bartley, J.K., Knoll, A.H., Grotzinger, J.P., Sergeev, V.N., 2000. Lithification and fabric genesis in precipitated stromatolites and associated peritidal carbonates, Mesoproterozoic Billyakh Group, Siberia, In: Grotzinger, J.P., James, N.P. (Eds.), Carbonate Sedimentation and Diagenesis in the Evolving Precambrian World. Society for Sedimentary Geology (SEPM), Tulsa, pp. 60-73.

Bauerman, H., 1885. Report on the geology of the country near the forty-ninth parallel of north latitude west of the Rocky Mountains, Report of progress 1882-1884. Geological Survey of Canada, pp. B 1-42.

Bergmann, K.D., Grotzinger, J.P., Fischer, W.W., 2013. Biological influences on seafloor carbonate precipitation. Palaios 28, 99-115.

Bertrand-Sarfati, J., Plaziat, J., MoussinePouchkine, A., 1997. Vermicular structures in the Neoproterozoic of the West African Craton: Microbialites versus 'molar tooth'. Facies 36, 231-234.

Bethke, C.M., Sanford, R.A., Kirk, M.F., Jin, Q., Flynn, T.M., 2011. The thermodynamic ladder in geomicrobiology. American Journal of Science 311, 183-210.

Bishop, J.W., Sumner, D.Y., 2006. Molar tooth structures of the Neoarchean Monteville Formation, Transvaal Supergroup, South Africa. I: Constraints on microcrystalline CaCO3 precipitation. Sedimentology 53, 1049-1068.

Bishop, J.W., Sumner, D.Y., Huerta, N.J., 2006. Molar tooth structures of the Neoarchean Monteville Formation, Transvaal Supergroup, South Africa. II: A wave-induced fluid flow model. Sedimentology 53, 1069-1082.

Bots, P., Benning, L.G., Rodriguez-Blanco, J.-D., Roncal-Herrero, T., Shaw, S., 2012. Mechanistic Insights into the Crystallization of Amorphous Calcium Carbonate (ACC). Crystal Growth & Design 12, 3806-3814.

Boudreau, B.P., 2012. The physics of bubbles in surficial, soft, cohesive sediments. Marine and Petroleum Geology 38, 1-18.

Bruckschen, P., Bruhn, F., Veizer, J., Buhl, D., 1995. 87Sr86Sr isotopic evolution of Lower Carboniferous seawater: Dinantian of western Europe. Sedimentary Geology 100, 63-81.

Calver, C., Baillie, P., 1990. Early diagenetic concretions associated with intrastratal shrinkage cracks in an Upper Proterozoic dolomite, Tasmania, Australia. Journal of Sedimentary Petrology 60, 293-305.

Canfield, D.E., Des Marais, D.J., 1993. Biogeochemical cycles of carbon, sulfur, and free oxygen in a microbial mat. Geochimica et Cosmochimica Acta 57, 3971-3984.

Cantine, M.D., Knoll, A.H., Bergmann, K.D., 2019. Carbonates before skeletons: A database approach. Earth-Science Reviews 201, 103065.

Carino, A., Testino, A., Andalibi, M.R., Pilger, F., Bowen, P., Ludwig, C., 2017. Thermodynamic-kinetic precipitation modeling. A case study: The amorphous calcium carbonate (ACC) precipitation pathway unravelled. Crystal Growth & Design 17, 2006-2015.

Cody, R., Cody, A., 1988. Gypsum nucleation and crystal morphology in analog saline terrestrial environments. Journal of Sedimentary Research 58, 247-255.

Cowan, C.A., James, N.P., 1992. Diastasis cracks: mechanically generated synaeresis-like cracks in Upper Cambrian shallow water oolite and ribbon carbonates. Sedimentology 39, 1101-1118.

Crawford, J., Goodman, E., Kah, L., 2006. Origin of Precambrian molar-tooth microspar: A new look at an old problem. Geological Society of America Abstracts with Programs 38, 24.

Crawford, J.C., Kah, L.C., 2004. Investigating the origin of Precambrian molar-tooth carbonate. Geological Society of America Abstracts with Programs 36, 251.

Daly, R.A., 1912. Memoir 38, Geology of the North American Cordillera at the forty-ninth parallel. Department of Mines Geological Survey of Canada, Ottawa.

Demicco, R.V., Hardie, L.A., 1994. An Inventory of Common Sedimentary Structures and Early Diagenetic Features of Shallow Marine Carbonate Deposits. SEPM, Tulsa, Oklahoma.

Du, Y., Han, X., Gu, S., Lin, W., Zhang, C., 2001. Earthquake event deposits in Mesoproterozoic Kunyang Group in Central Yunnan Province and its geological implications. Science in China (Series D) 31, 283-289.

Dupraz, C., Visscher, P.T., 2005. Microbial lithification in marine stromatolites and hypersaline mats. Trends in Microbiology 13, 429-438.

Eby, D., 1975. Carbonate sedimentation under elevated salinities and implications for the origin of “molar-tooth” structure in the Middle Belt Carbonate interval (late Precambrian), northwestern Montana. Abstracts with Program 7, 1063.

Evans, D., Gray, W.R., Rae, J.W.B., Greenop, R., Webb, P.B., Penkman, K., Kröger, R., Allison, N., 2020. Trace and major element incorporation into amorphous calcium carbonate (ACC) precipitated from seawater. Geochimica et Cosmochimica Acta 290, 293-311.

Evans, D., Webb, P.B., Penkman, K., Kroger, R., Allison, N., 2019. The characteristics and biological relevance of inorganic amorphous calcium carbonate (ACC) precipitated from seawater. Crystal Growth & Design 19, 4300-4313.

Fairchild, I.J., Einsele, G., Song, T., 1997. Possible seismic origin of molar tooth structures in Neoproterozoic carbonate ramp deposits, north China. Sedimentology 44, 611-636.

Fairchild, I.J., Spencer, A.M., Ali, D.O., Anderson, R.P., Anderton, R., Boomer, I., Dove, D., Evans, J.D., Hambrey, M.J., Howe, J., 2018. Tonian-Cryogenian boundary sections of Argyll, Scotland. Precambrian Research 319, 37-64.

Fenton, C.L., Fenton, M.A., 1937. Belt series of the North: Stratigraphy, sedimentation, paleontology. Bulletin of the Geological Society of America 48, 1873-1970.

Fike, D.A., Bradley, A.S., Rose, C.V., 2015. Rethinking the ancient sulfur cycle. Annual Review of Earth and Planetary Sciences 43, 593-622.
Frank, T.D., Kah, L.C., Lyons, T.W., 2003. Changes in organic matter production and accumulation as a mechanism for isotopic evolution in the Mesoproterozoic Ocean. Geological Magazine 140, 397-420.
Frank, T.D., Lyons, T.W., 1998. “Molar-tooth” structures: A geochemical perspective on a Proterozoic enigma. Geology 26, 683-686.
Furniss, G., Rittel, J.F., Winston, D., 1998. Gas bubble and expansion crack origin of "molar-tooth" calcite structures in the Middle Proterozoic Belt Supergroup, Western Montana. Journal of Sedimentary Research 68, 104-114.
Gilleaudeau, G., Kah, L., 2010. Molar-tooth crack formation and the Proterozoic marine substrate: Insights from the Belt Supergroup, Montana and the Atar Group, Mauritania. Geological Society of America Abstracts with Programs 42, 137.
Goodman, E.E., Kah, L., 2007. Reassessing formation of Precambrian molar-tooth microspar: constraints from carbonate precipitation experiments. Geological Society of America Abstracts with Programs 39, 420.
Grotzinger, J.P., 1989. Facies and evolution of Precambrian carbonate depositional systems: Emergence of the modern platform archetype. SEPM Special Publications 44, 79-106.
Grotzinger, J.P., 1990. Geochemical model for Proterozoic stromatolite decline. American Journal of Science 290a, 80-108.
Grotzinger, J.P., Knoll, A.H., 1999. Stromatolites in Precambrian carbonates: evolutionary mileposts or environmental dipsticks? Annual Review of Earth and Planetary Sciences 27, 313-358.
Halverson, G.P., Wade, B.P., Hurtgen, M.T., Barovich, K.M., 2010. Neoproterozoic chemostratigraphy. Precambrian Research 182, 337-350.
Harazim, D., Callow, R.H., Mcilroy, D., 2013. Microbial mats implicated in the generation of intrastratal shrinkage (‘synaeresis’) cracks. Sedimentology 60, 1621-1638.
Hemming, N.G., Meyers, W.J., Grams, J.C., 1989. Cathodoluminescence in diagenetic calcites; the roles of Fe and Mn as deduced from electron probe and spectrophotometric measurements. Journal of Sedimentary Research 59, 404-411.
Higgins, J.A., Fischer, W., Schrag, D., 2009. Oxygenation of the ocean and sediments: consequences for the seafloor carbonate factory. Earth and Planetary Science Letters 284, 25-33.
Hodgskiss, M.S.W., Kunzmann, M., Poirier, A., Halverson, G.P., 2018. The role of microbial iron reduction in the formation of Proterozoic molar tooth structures. Earth and Planetary Science Letters 482, 1-11.
Hofmann, H., 1985. The mid-Proterozoic Little Dal macrobiota, Mackenzie Mountains north-west Canada. Palaeontology 28, 331-354.
Horodyski, R.J., 1976. Stromatolites of the upper Siyeh limestone (Middle Proterozoic), Belt Supergroup, Glacier National Park, Montana. Precambrian Research 3, 517-536.

Ihli, J., Wong, W.C., Noel, E.H., Kim, Y.-Y., Kulak, A.N., Christenson, H.K., Duer, M.J., Meldrum, F.C., 2014. Dehydration and crystallization of amorphous calcium carbonate in solution and in air. Nature communications 5, 1-10.

James, N.P., Narbonne, G.M., Sherman, A.G., 1998. Molar-tooth carbonate: Shallow subtidal facies of the Mid- to Late Proterozoic. Journal of Sedimentary Research 68, 716-722.

Jia, Z.H., Hong, T.Q., Zheng, W.W., Li, S.Y., 2003. The characters and environments of the seismites of the Neoproterozoic Wangshan Formation in North Anhui. Journal of Stratigraphy 27, 146-149, 158.

Jia, Z.H., Ning, X.F., Hong, T.Q., Zheng, W.W., 2011. The Neoproterozoic molar-tooth carbonate rock veins in northern Anhui and Jiangso Provinces and their forming mechanism. Journal of Paleogeography 13, 627-634.

Jüngst, H., 1934. Zur geologischen Bedeutung der Synärese. Geologische Rundschau 25, 312-325.

Kah, L.C., Bartley, J., Milam, K., 2007. Unusual breccias in the Proterozoic Atar Group, Mauritania-Mali-Algeria: potential deposition related to extraterrestrial impact and impact-related tsunamis. Geological Society of America Abstracts with Programs 39, 311.

Kah, L.C., Bartley, J.K., 2021. Carbonate fabric diversity and environmental heterogeneity in the late Mesoproterozoic Era. Geological Magazine, 1-27.

Kah, L.C., Bartley, J.K., Teal, D.A., 2012. Chemostratigraphy of the Late Mesoproterozoic Atar Group, Taoudeni Basin, Mauritania: Muted isotopic variability, facies correlation, and global isotopic trends. Precambrian Research 200-203, 82-103.

Kah, L.C., Knoll, A.H., 1996. Microbenthic distribution of Proterozoic tidal flats: Environmental and taphonomic considerations. Geology 24, 79-82.

Kah, L.C., Lyons, T.W., Chesley, J.T., 2001. Geochemistry of a 1.2 Ga carbonate-evaporite succession, northern Baffin and Bylot Islands: implications for Mesoproterozoic marine evolution. Precambrian Research 111, 203-234.

Kaufman, A.J., Hayes, J., Knoll, A.H., Germs, G.J., 1991. Isotopic compositions of carbonates and organic carbon from upper Proterozoic successions in Namibia: stratigraphic variation and the effects of diagenesis and metamorphism. Precambrian Research 49, 301-327.

Kile, D.E., Eberl, D.D., 2003. On the origin of size-dependent and size-independent crystal growth: Influence of advection and diffusion. American Mineralogist 88, 1514-1521.

Kile, D.E., Eberl, D.D., Hoch, A.R., Reddy, M.M., 2000. An assessment of calcite crystal growth mechanisms based on crystal size distributions. Geochimica et Cosmochimica Acta 64, 2937-2950.

Knoll, A., Swett, K., 1990. Carbonate deposition during the late Proterozoic Era: an example from Spitsbergen. American Journal of Science 290, 104-132.

Kuang, H.-W., 2014. Review of molar tooth structure research. Journal of Paleogeography 3, 359-383.

Kuznetsov, V., 2003. The "molar tooth" structure and its relation to bios evolution. Doklady Earth Sciences 392, 947-950.

Lee, M.R., Hodson, M.E., Langworthy, G.N., 2018. Crystallization of calcite from amorphous calcium carbonate: earthworms show the way. Mineralogical Magazine 72, 257-261.

Littlewood, J.L., Shaw, S., Peacock, C.L., Bots, P., Trivedi, D., Burke, I.T., 2017. Mechanism of Enhanced Strontium Uptake into Calcite via an Amorphous Calcium Carbonate Crystallization Pathway. Crystal Growth & Design 17, 1214-1223.

Long, D.G.F., 2007. Tomographic study of Paleoproterozoic carbonates as key to understanding the formation of molar-tooth structure. Gondwana Research 12, 566-570.

Lyons, T.W., Anbar, A.D., Severmann, S., Scott, C., Gill, B.C., 2009. Tracking euxinia in the ancient ocean: a multiproxy perspective and Proterozoic case study. Annual Review of Earth and Planetary Sciences 37, 507-534.

Machel, H.G., 1985. Cathodoluminescence in Calcite and Dolomite and Its Chemical Interpretation. Geoscience Canada 12, 139-147.

Marshall, D., Anglin, C., 2004. CO_2-clathrate destabilization: a new model of formation for molar tooth structures. Precambrian Research 129, 325-341.

Matsunuma, S., Kagi, H., Komatsu, K., Maruyama, K., Yoshino, T., 2014. Doping Incompatible Elements into Calcite through Amorphous Calcium Carbonate. Crystal Growth & Design 14, 5344-5348.

Mei, M., Tucker, M.E., 2011. Molar tooth structure: a contribution from the Mesoproterozoic Gaoyuzhuang Formation, Tianjin City, North China. Acta Geologica Sinica-English Edition 85, 1084-1099.

Miller, K., Simpson, E.L., Sherrod, L., Wizevich, M.C., Malenda, M., Morgano, K., Richardson, A., Livingston, K., Bogner, E., 2018. Gas bubble cavities in deltaic muds, Lake Powell delta, Glen Canyon National Recreation Area, Hite, Utah. Marine and Petroleum Geology 92, 904-912.

Morse, J.W., Mackenzie, F.T., 1990. Geochemistry of Sedimentary Carbonates. Elsevier, Amsterdam, The Netherlands.

Moussine-Pouchkine, A., Bertrand-Sarfati, J., 1997. Tectonosedimentary subdivisions in the Neoproterozoic to Early Cambrian cover of the Taoudenni Basin (Algeria-Mauritania-Mali). Journal of African Earth Sciences 24, 425-443.

Nealson, K.H., 1997. Sediment bacteria: who's there, what are they doing, and whaat's new? Annual Review of Earth and Planetary Sciences 25, 403-434’

O'Connor, M.P., 1972. Classification and environmental interpretation of the cryptalgal organosedimentay "molar-tooth" structure from the late Precambrian Belt-Purcell Supergroup. Journal of Geology 80, 592-610.

Petrov, P.Y., 2011. Molar tooth structures: Formations and specificity of carbonate diagenesis in the Late Precambrian, Middle Riphean Sukhaya Tunguska Formation of the Turukhansk Uplift, Siberia. Stratigraphy and Geological Correlation 19, 247-267.

Plummer, P.S., Gostin, V.A., 1981. Shrinkage cracks: disiccation or synaeresis? Journal of Sedimentary Petrology 51, 1147-1156.

Pollock, M.D., Kah, L.C., Bartley, J.K., 2006. Morphology of Molar-Tooth Structures in Precambrian Carbonates: Influence of Substrate Rheology and Implications for Genesis. Journal of Sedimentary Research 76, 310-323.
Pope, M.C., Bartley, J.K., Knoll, A.H., Petrov, P.Y., 2003. Molar tooth structures in calcareous nodules, early Neoproterozoic Burovaya Formation, Turukhansk region, Siberia. Sedimentary Geology 158, 235-248.
Pratt, B.R., 1998. Syneresis cracks: subaqueous shrinkage in argillaceous sediments caused by earthquake-induced dewatering. Sedimentary Geology 117, 1-10.
Pratt, B.R., 2001. Oceanography, bathymetry and syndepositional tectonics of a Precambrian intracratonic basin: integrating sediments, storms, earthquakes and tsunamis in the Belt Supergroup (Helena Formation, ca. 1.45 Ga), western North America. Sedimentary Geology, 371-394.
Pratt, B.R., 2002. Storms versus tsunamis: Dynamic interplay of sedimentary, diagenetic, and tectonic processes in the Cambrian of Montana. Geology 30, 423-426.
Pratt, B.R., 2011. Molar-tooth structure, In: Reitner, J., Thiel, V. (Eds.), Encyclopedia of Geobiology. Springer, University of Göttingen, Germany, pp. 662-666.
Present, T.M., Gomes, M.L., Trower, E.J., Stein, N.T., Lingappa, U.F., Naviaux, J., Thorpe, M.T., Cantine, M.D., Fischer, W.W., Knoll, A.H., 2021. Non-lithifying microbial ecosystem dissolves peritidal lime sand. Nature communications 12, 1-8.
Purgstaller, B., Goetschl, K.E., Mavromatis, V., Dietzel, M., 2019. Solubility investigations in the amorphous calcium magnesium carbonate system. CrystEngComm 21, 155-164.
Qiao, X., Song, T., Gao, L.Z., Peng, Y., Li, H., Gao, M., Song, B., Zhang, Q., 1994. Seismic Sequence in Carbonate Rocks By Vibrational Liquefaction. Acta Geologica Sinica-English Edition 7, 243-265.
Rezak, R., 1957. Stromatolites of the Belt series in Glacier National Park and vicinity, Montana. USGS Professional Paper 294(D), 127-154.
Rimstidt, D.J., Balog, A., Webb, J., 1998. Distribution of trace elements between carbonate minerals and aqueous solutions. Geochimica et Cosmochimica Acta 62, 1851-1863.
Roest-Ellis, S., Strauss, J.V., Tosca, N.J., 2021. Experimental constraints on nonskeletal CaCO3 precipitation from Proterozoic seawater. Geology 49, 561-565.
Ross, C.P., 1959. Geology of Glacier National Park and the Flathead region, northwestern Montana. US Geological Survey.
Rossetti, D.d.F., 2000. Molar-tooth carbonate: shallow subtidal facies of the Mid- to Late Proterozoic-Discussion. Journal of Sedimentary Research 70, 1246-1248.
Rossetti, D.d.F., Góes, A.M., 2000. Deciphering the sedimentological imprint of paleoseismic events: an example from the Aptian Codó Formation, northern Brazil. Sedimentary Geology 135, 137-156.
Sami, T.T., James, N.P., 1996. Synsedimentary cements as Paleoproterozoic platform building blocks, Pethei Group, northwestern Canada. Journal of Sedimentary Research 66, 209-222.
Santschi, P., Höhener, P., Benoit, G., Buchholtz-ten Brink, M., 1990. Chemical processes at the sediment-water interface. Marine Chemistry 30, 269-315.

Savard, M.M., Veizer, J., Hinton, R., 1995. Cathodoluminescence at low Fe and Mn concentrations: A SIMS study of zones in natural calcites. Journal of Sedimentary Research A65, 208-213.

Shen, B., Dong, L., Xiao, S., Lang, X., Huang, K., Peng, Y., Zhou, C., Ke, S., Liu, P., 2016. Molar tooth carbonates and benthic methane fluxes in Proterozoic oceans. Nature communications 7, 1-6.

Shields, G.A., 2002. 'Molar-tooth microspar': a chemical explanation for its disappearance ~ 750 Ma. Terra Nova 14, 108-113.

Shields-Zhou, G.A., Hill, A.C., Macgabhann, B.A., 2012. The cyogenian period, In: Gradstein, F.M., Ogg, J.G., Schmitz, M.D., Ogg, G.M. (Eds.), The Geologic Time Scale. Elsevier, Boston, pp. 393-411.

Smith, A., 2016. A review of molar-tooth structures with some speculations on their origin, In: MacLean, J.S., Sears, J.W. (Eds.), Belt Basin: Window to Mesoproterozoic Earth. Geological Society of America Special Paper, pp. 71-99.

Smith, G.A., 1968. The Origin and Deformation of Some "Molar-Tooth" Structures in the Precambrian Belt-Purcell Supergroup. Journal of Geology 76, 426-443.

Soetaert, K., Hofmann, A.F., Middelburg, J.J., Meysman, F.J., Greenwood, J., 2007. Reprint of "The effect of biogeochemical processes on pH". Marine Chemistry 106, 380-401.

Stagner, A.F., Bartley, J.K., Kah, L.C., 2004. Variation in deformation style of molar-tooth structure during fluidization: Tawaz Formation, Atar Group, Mauritania. Geological Society of America Abstracts with Programs 36, 88.

Stewart, E.K., Mauk, J.L., 2017. Sedimentology, sequence-stratigraphy, and geochemical variations in the Mesoproterozoic Nonesuch Formation, northern Wisconsin, USA. Precambrian Research 294, 111-132.

Strauss, J.V., Tosca, N.J., 2020. Mineralogical constraints on Neoproterozoic pCO_2 and marine carbonate chemistry. Geology 48, 599-603.

Sumner, D.Y., 1997. Carbonate precipitation and oxygen stratification in late Archean seawater as deduced from facies and stratigraphy of the Gamohaan and Frisco formations, Transvaal Supergroup, South Africa. American Journal of Science 297, 455-487.

Sumner, D.Y., 2000. Microbial vs environmental influences on the morphology of Late Archean fenestrate microbialites, In: Riding, R.E., Awramik, S.M. (Eds.), Microbial sediments. Springer, Berlin, pp. 307-314.

Sumner, D.Y., Grotzinger, J.P., 1996. Were kinetics of Archean calcium carbonate precipitation related to oxygen concentration? Geology 24, 119-122.

Sundby, B., Silverberg, N., 1985. Manganese fluxes in the benthic boundary layer 1. Limnology and Oceanography 30, 372-381.

Tanner, P., 1998. Interstratal dewatering origin for polygonal patterns of sand-filled cracks: a case study from late Proterozoic metasediments of Islay, Scotland. Sedimentology 45, 71-89.

Thamdrup, B., Fossing, H., Jørgensen, B.B., 1994. Manganese, iron and sulfur cycling in a coastal marine sediment, Aarhus Bay, Denmark. Geochimica et Cosmochimica Acta 58, 5115-5129.

Tosca, N.J., Macdonald, F.A., Strauss, J.V., Johnston, D.T., Knoll, A.H., 2011. Sedimentary talc in Neoproterozoic carbonate successions. Earth and Planetary Science Letters 306, 11-22.

Walter, L.M., Bischof, S.A., Patterson, W.P., Lyons, T.W., 1993. Dissolution and recrystallization in modern shelf carbonates: evidence from pore water and solid phase chemistry. Philosophical Transactions of the Royal Society of London. Series A: Physical and Engineering Sciences 344, 27-36.

Warren, J.K., Kendall, C.G.S.C., 1985. Comparison of sequences formed in marine sabkha (subaerial) and salina (subaqueous) settings—modern and ancient. AAPG Bulletin 69, 1013-1023.

Winston, D., Rittel, J.F., Furniss, G., 1999. Gas bubble and expansion crack origin of molar-tooth calcite structures in the Middle Proterozoic Belt Supergroup, western Montana-reply. Journal of Sedimentary Research 69, 1140-1145.

Wu, H., Wang, G., Ding, X., Wang, H., 2020. Geochemistry of the Neoproterozoic molar tooth carbonate in the Benxi Area, North China Craton: The paleo-ocean environment. Journal of Coastal Research 115, 446-450.

Young, G., Jefferson, C., 1975. Late Precambrian shallow water deposits, Banks and Victoria Islands, Arctic Archipelago. Canadian Journal of Earth Sciences 12, 1734-1748.

Young, G., Long, D., 1977. Carbonate sedimentation in a late Precambrian shelf sea, Victoria Island, Canadian Arctic Archipelago. Journal of Sedimentary Research 47, 943-955.

Zhou, Y., Pogge von Strandmann, P.A.E., Zhu, M., Ling, H., Manning, C., Li, D., He, T., Shields, G.A., 2020. Reconstructing Tonian seawater 87Sr/86Sr using calcite microspar. Geology 48, 462-467.

CHAPTER II

ORIGIN AND EARLY DIAGENESIS OF PRECAMBRIAN MOLAR-TOOTH MICROSPAR: EVIDENCE FROM CRYSTAL SIZE DISTRIBUTIONS AND GEOCHEMISTRY

ABSTRACT

Molar-tooth structure (MTS) is an enigmatic carbonate fabric composed of variously shaped cracks and voids, filled with calcite microspar, that occurs in the geologic record of the Precambrian. Detailed petrographic analysis of samples that span both in paleogeographic locality and time shows that the crack-filling calcite microspar records characteristic features that together define the texture: non-interlocking individual micrometer-size calcite crystals with planar boundaries, and the presence of an inner non-luminescent core surrounded by a luminescent rim when analyzed under cathodoluminescence microscopy (CL). Here we provide crystal size distributions (CSDs) to better understand the nucleation and growth processes suffered by these crystals, in addition to microprobe trace element analysis and X-ray elemental maps. Analysis is consistent with an interpretation that the cores result from nucleation in an open space at high carbonate saturation states with subsequent Ostwald ripening. In a distinct second phase of crystal growth, larger and more stable crystals continued growing in a more restricted space, with lower carbonate saturation, and incorporating the least compatible elements from the surrounding solution. We have also observed that the characteristic zoning seen under CL is consistent with contrasting compositions of minor elements, such as Mg and Sr, and not just the expected differences in Fe and Mn defined by the CL. We considered that previously published hypothesis for the precipitations of the micrite cement in a supersaturated environment by the formation of amorphous calcium carbonate and associated gel phase, and subsequent dehydration and formation of crystalline phases is suitable to explain the CSD behavior seen here.

INTRODUCTION

Molar-tooth Structure

Molar-tooth structure (MTS) is an enigmatic Precambrian carbonate fabric that is composed of variously shaped cracks and voids filled with calcite microspar (Kriscautzky et al., 2022; Smith, 2016; Kuang, 2014; Pollock et al., 2006). In the field, MTS occurs as an often-interconnected array of planar to crenulated, millimeter to centimeter-scale fractures and blobs, mainly within fine-grained, clayey to silty, mechanically or microbially laminated carbonate rocks (Figure 2.1) (Hodgskiss et al., 2018; Pratt, 2011; Furniss et al., 1998; Pratt, 1998), and more rarely within fine-grained siliciclastic rocks (Gilleaudeau and Kah, 2010; Bishop and Sumner, 2006; Bishop et al., 2006). Regardless of differences in host rock, the microspar that fills MTS is characteristically distinct (Long, 2007; Bishop and Sumner, 2006; Pollock et al., 2006; Marshall and Anglin, 2004; Pratt, 1998). MT microspar is represented by uniform, equant, limpid crystals, that average approximately 11 μm in diameter, and show generally planar, non-interlocking crystalline boundaries (Kriscautzky et al., 2022; Pollock et al., 2006). Evidence for compaction of host rock laminae around microspar-filled voids (Pratt, 2011; Pollock et al., 2006; Pratt, 1998;

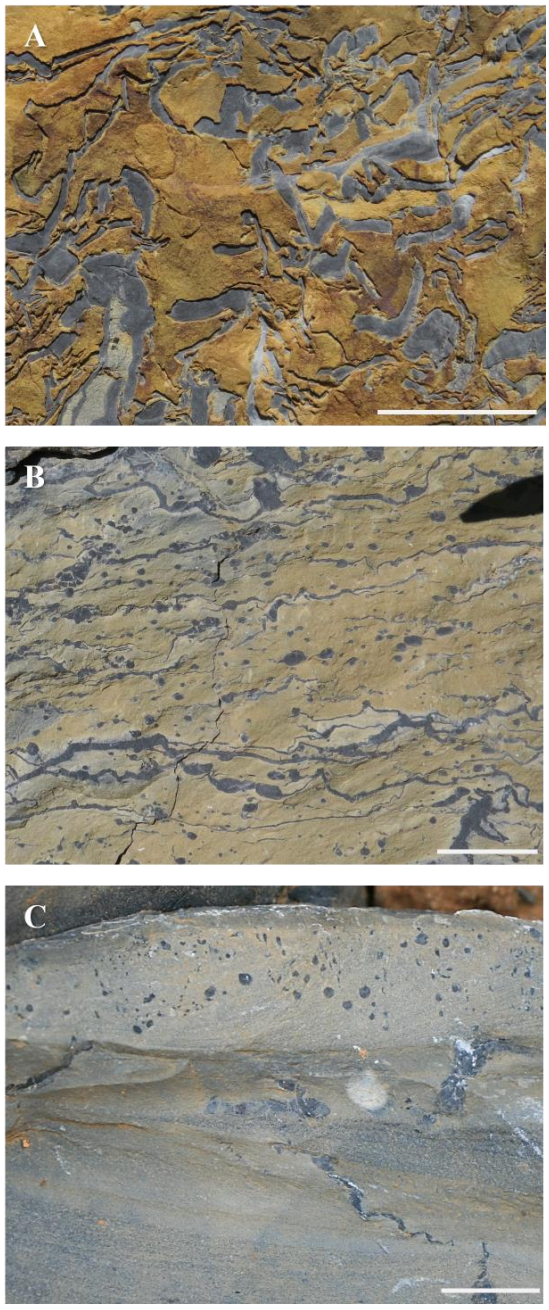


Figure 2.1. Outcrop photographs of molar-tooth structure exposed on weathered surfaces. MT microspar appears as dark grey, uniform, smooth features within a coarser-grained, yellowish, dolomite-rich matrix. A to C show a transition from traditional ribbons to spherical features. A) MT ribbons in all orientations from the Belt Supergroup, Montana, US. B) Subhorizontal elongated ribbons with tadpole-shaped blebs both within the ribbons and isolated in the host rock, from the Belt Supergroup, Montana, US. C) Spherical MT blebs within a coarser-grained, detritus-rich matrix from Northeast China. Scale bars are 2 cm.

Fairchild et al., 1997; Smith, 1968) and the presence of clasts composed of MT microspar within synsedimentary breccias (cf. Kriscautzky et al., 2022; Furniss et al., 1998; Pratt, 1998; O'Connor, 1972) indicate that both voids and void-filling cement formed at or near the sediment-water interface, undergoing full lithification prior to later sediment compaction.

This latter observation highlights the enigmatic nature of MTS. Molar-tooth structure juxtaposes void formation within a cohesive yet unlithified substrate while, at the same time, hosting the penecontemporaneous precipitation and lithification of void-filling carbonate microspar. Furthermore, MTS and its unusual void-filling microspar are known only from the Precambrian and lack suitable modern analogs. In a recently published review, Kriscautzky et al. (2022) compiled literature occurrences to analyze the distribution of MTS in time and space (Figure 2.2). The vast majority of MT occurrences are from shallow marine systems in the Meso- and Neoproterozoic eras, and most particularly between 1.2 and 0.8 Ga. Although this represents a significant interval in geologic time, the abundance of MTS at this time suggests a unique set of environmental conditions. For example, methane bubble formation (cf. Algar and Boudreau 2010; James et al., 2016) and crack formation in marine carbonates (cf. McMahon et al., 2016) are known to occur in sediments in the modern, yet not preserved. Fully understanding the mechanism of MT formation is therefore critical to the study and understanding of early Earth environments (Kriscautzky et al., 2022; Kah and Bartley, 2021; Cantine et al., 2019; Fairchild et al., 2018; Shields, 2002; James et al., 1998).

Models of Formation

Until recently, most evaluations of MTS have focused on the macroscale morphology of the cracks and the mechanisms driving crack formation. In a recent review, Kriscautzky et al. (2022) grouped these mechanisms into five main categories: Many of the early investigations of MTS tended to favor a potential biological origin (cf. Moussine-Pouchkine and Bertrand-Sarfati, 1997; O'Connor, 1972; Smith, 1968), wherein the calcite-filled voids represent either remains (or casts) of algal thalli or an organosedimentary deposit similar to stromatolites. Other early workers suggested an origin as under evaporitic conditions (cf. Eby, 1975), wherein the complex and variable morphologies of MTS were hypothesized to reflect primary deposition and deformation associated with an evaporite phase (Cody and Cody, 1988; Warren and Kendall, 1985) that was later dissolved and replaced by a secondary carbonate microspar.

More recent work, however, more often considers MTW to result from physical changes in the sediment package, such as sediment shrinkage (cf. Petrov, 2011; Demicco and Hardie, 1994; Calver and Baillie, 1990; Knoll and Swett, 1990; Young and Long, 1977; Horodyski, 1976), either via desiccation, or subaqueously by changes in salinity, which triggers the expulsion of water from clay lattice interlayers and a decrease in sediment volume, or by reduction of smectite to illite during early diagenesis and its associated volume loss (Hodgskiss et al., 2018). Because MT ribbons often occur parallel to each other within individual beds, others have suggested crack formation via stress-induced processes (cf. Pratt, 2011; Long, 2007; Bishop and Sumner, 2006; Bishop et al., 2006;

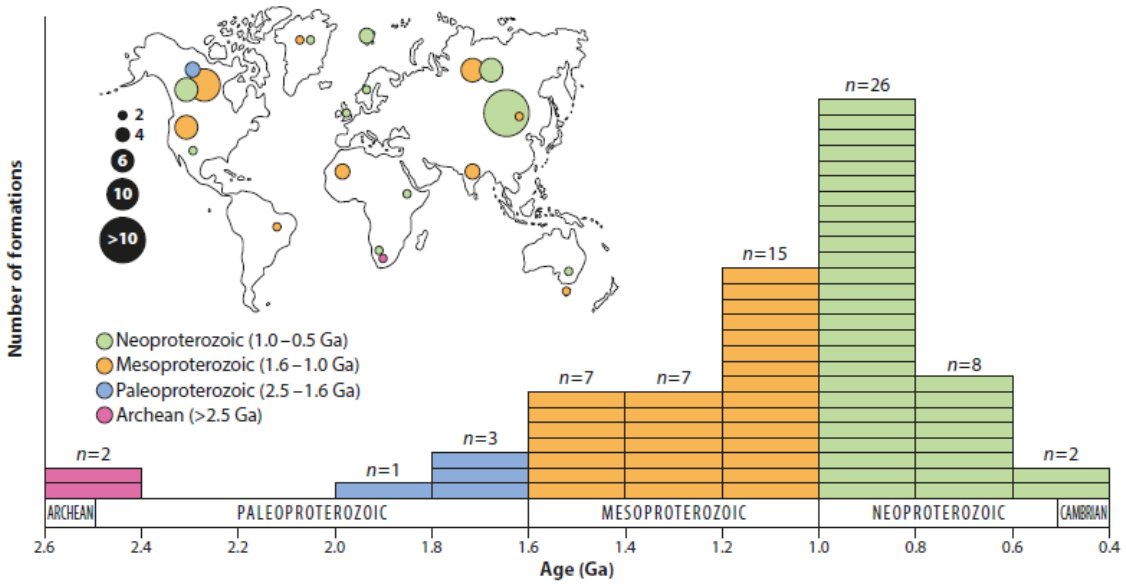


Figure 2.2. Distribution of MTS occurrences in space and time. The map at the top left shows the distribution of MTS occurrences by region. The size of the circles represents the number of formations in which MTS is been recorded. Colors represent age. The histogram in the main panel shows the time distribution of MTS. Bin size is 200 My, and colors are separated by era. After Kriscautzky et al. (2022).

Pratt, 1998; Qiao et al., 1994; Rezak, 1957; Fenton and Fenton, 1937; Daly, 1912). A variety of mechanisms have been proposed, including diastasis driven by hydraulic shear across a cohesive substrate (Cowan and James, 1992), substrate liquefaction by hydraulic loading (Kah et al., 2007; Bertrand-Sarfati et al., 1997; Fairchild et al., 1997; Moussine-Pouchkine and Bertrand-Sarfati, 1997), and earthquake-induced fluidization, dewatering, and compaction (Jia et al., 2011; Jia et al., 2003; Du et al., 2001; Pratt, 2001, 1998; Qiao et al., 1994).

The most widely considered mechanism for the formation of MTS, however, is gas expansion and migration (cf. Miller et al., 2018; Smith, 2016; Kuang, 2014; Boudreau, 2012; Mei and Tucker, 2011; Pratt, 2011; Long, 2007; Bishop and Sumner, 2006; Pollock et al., 2006; Kuznetsov, 2003; Pope et al., 2003; Winston et al., 1999; Furniss et al., 1998; Pratt, 1998; Horodyski, 1976; Young and Jefferson, 1975) which considers the movement of gasses within the substrate. Although there is little consensus about the gasses responsible for MTS formation (Frank and Lyons, 1998), most models consider gasses produced by microbial decomposition of organic matter (cf. Horodyski, 1976; Young and Jefferson, 1975). In this scenario, initial gas production is believed to be represented by MT blebs, and migration of gasses upward through the substrate is represented by vertical cracks. Pollock et al. (2006) linked gas expansion and migration to substrate rheology and suggested that MT morphology would change predictably with changes in the physical property of the substrate. Observations of morphological change across facies has since been made by several authors (cf. Kuang, 2014; Pratt, 2011; Bishop and Sumner, 2006; Pratt, 1998), which supports a gas expansion and migration model.

Although these models each provide a plausible explanation for the formation of MT cracks and voids, the majority of these models lack a mechanism to explain the penecontemporaneous precipitation of microspar within MT voids. A biological origin was dismissed by observations of cross-cutting relationships among MT and stromatolites (Horodyski, 1976), morphologies inconsistent with algal thalli or fronds (Hofmann, 1985), and reinterpretation as deformed and brecciated MTS (Kah et al., 2012; Stagner et al., 2004). Eby (1975), who considered MTS to represent original precipitation of a sulfate evaporite, suggested that the solubility of such phases would result in potential dissolution and recrystallization as carbonate. MTS, however, have not been reported to preserve either evaporite minerals (Bishop and Sumner, 2006; Pratt, 2002), and petrographic characteristics of replacement minerals (Pollock et al., 2006). Similarly, most models that suggest sediment shrinkage or stress-induced cracking do not provide a concurrent mechanism to explain the filling of the voids by microspar (cf. Fairchild et al., 1997). Pratt (2011), Pratt (1998), and Qiao et al. (1994), however, suggested that during seismic shaking, microspar might be segregated from the sediment matrix into the voids. These hypotheses seem unlikely when considering the petrographic character of the microspar (cf. Kuang, 2014; Pollock et al., 2006) and certainly are not applicable for lithologies lacking lime mud (Bishop and Sumner, 2006).

More convincingly, proponents of gas expansion models for MT genesis argue that precipitation of MT microspar within voids was triggered by gas-forming reactions (cf. Strauss and Tosca, 2020; Shen et al., 2016; Pollock et al., 2006; Marshall and Anglin, 2004; Frank and Lyons, 1998), that may have produced CO_2, H_2S, or CH_4, each of which may

trigger changes in local carbonate saturation state, thereby triggering carbonate precipitation (cf. Bergmann et al., 2013; Nealson, 1997; Morse and Mackenzie, 1990; Santschi et al., 1990). Consensus has not been reached, however, with respect to which of these gasses may be involved. Frank and Lyons (1998) did not find C-isotope evidence consistent with either sulfate reduction (H_2S) or methanogenesis (CH_4). Marshall and Anglin (2004) have also proposed destabilization of substrate CO_2-clathrates allowing both crack opening associated with the clathrate's breakdown and $CaCO_3$ precipitation by the combination of the expelled CO_2 with seawater. Additionally, redox changes (Hodgskiss et al., 2018) promote reduction of Fe-rich smectite increasing alkalinity which triggers carbonate precipitation along with releasing bicarbonate and silica (Vorhies and Gaines, 2009; Li et al., 2004) which could drive microspar precipitation within recently opened voids.

Investigation of MT microspar

Regardless of the mechanism of formation of MT voids, it is the precipitation of MT microspar that acts to preserve MTS in the geologic record, and demonstrates the critical nature of investigations that focus on the void-filling microspar that is contained within MTS. James et al. (1998) even suggested that the volume of carbonate precipitated as MT microspar during the Precambrian (ca. 5-25%) of individual platform successions, was analogous to the volume precipitated by invertebrates in the Phanerozoic in similar settings. Furthermore, because MT microspar does not appear to record the diagenetic changes experienced by host lithologies (cf. Kriscautzky et al., 2022), it has been commonly used to infer geochemical conditions within the Precambrian oceans, including marine isotopic and elemental compositions (Wu et al., 2020; Zhou et al., 2020), redox state (Hodgskiss et al., 2018; Shen et al., 2016; Frank and Lyons, 1998), and marine pH, pCO_2 and carbonate saturation state (Roest-Ellis et al., 2020; Strauss and Tosca, 2020; Tosca et al., 2011).

MT microspar, however, is not a single phase. Cathodoluminescence microscopy (CL; Kriscautzky et al., 2022; Bishop and Sumner, 2006; Crawford et al., 2006; Pollock et al., 2006), and scanning electron microscopy (Smith, 2016; Pratt, 2011) shows that MT microspar is actually composed of geochemically distinct two-phase crystals that occur in crystallographic continuity. Kriscautzky et al. (2022), using detailed CL petrography, also showed substantial variation within MT microspar that suggests the potential for substantial recrystallization early in the history of MT microspar formation. Here we suggest that a better understanding of the precipitation and early recrystallization of MT microspar, with a particular focus on its two-phase composition, may help constrain the chemical conditions under which it formed, and will provide key insights into carbonate formation in the Precambrian. Specifically, we will use a combination of CL petrography, crystal size distributions (CSDs), and electron microprobe point and element maps to further explore the origin and earliest diagenesis of MT microspar.

Crystal Size Distributions

Crystal size distributions (CSDs) represent the number of given crystals of a specific size within a determined volume (cf. Rannou and Caroff, 2010) and are commonly used to characterize crystalline materials. Most broadly developed within igneous petrology, CSD theory uses characteristic differences in frequency distribution to infer processes related to nucleation and growth (Cashman and Marsh, 1988; Marsh, 1988) and grain ripening (cf. Berger et al., 2011). Similarly, CSDs have also been used to aid in interpreting the nucleation, growth, and recrystallization behavior of chemical precipitates (Kile and Eberl, 2003; Kile et al., 2000; Eberl et al., 1998; Wilkin, 1995).

Fundamentally, the shape of a CSD curve reflects the behavior of crystal nucleation (Baronnet, 1982; Wagner, 1961). In igneous systems, nucleation of a particular mineral phase responds primarily to thermodynamic forcing related to magmatic cooling (Špillar and Dolejš, 2014) which triggers an increasing rate of nucleation. This increasing rate of nucleation results in an asymptotic distribution of crystal sizes with the smallest crystals occurring with the highest frequency (Figure 2.3A). Such asymptotic distributions are most often plotted on a semi-log plot (Marsh, 1988), which transforms the CSD into a straight line. Nucleation is then followed by surface-controlled growth (Kile et al., 2000), which does not result in observable changes in the asymptotic distribution curve.

By contrast, minerals precipitated at low temperature within aqueous systems (cf. Kile and Eberl, 2003) show a very different distribution. In aqueous systems, nucleation is driven largely by kinetics, and often requires a state saturation that far exceeds calculated thermodynamic thresholds. At elevated saturation states, pre-nucleation clusters (Bots et al., 2012; Gebauer and Cölfen, 2011) spontaneously and repeatedly form and dissolve, with only few growing to a size at which they can function as stable nuclei. When a critical threshold of oversaturation is reached, however, these pre-nucleation clusters are able to readily grow to a point at which they remain stable, and nucleation proceeds rapidly as mineral precipitation causes saturation state to fall. Such systems result in a lognormal distribution (Figure 2.3B), wherein the natural logarithms of the crystal sizes are normally distributed, yet when, instead, crystal sizes are plotted, the curve is skewed toward larger sizes (Kile et al., 2000).

Once nucleation occurs, growth then proceeds either by proportionate or surface-controlled growth. During proportionate growth (sometimes called size-dependent growth) the proportion of the crystals in each relative size category remains the same from the beginning to the end of the process; Therefore, the shape of the CSD curve remains the same, though the position of the curve shifts along the x-axis (Kile and Eberl, 2003).

Surface-controlled growth (or size-independent growth), on the other hand, is a process by which the larger crystals which have a proportionately larger surface in contact with the surrounding fluids, will grow faster than those crystals of a smaller size (Kile and Eberl, 2003). Kile and Eberl (2003) investigated both of these growth patterns during laboratory precipitation of carbonate and showed that proportionate growth occurred when reactants were supplied to the growth surface through advection, and that surface-controlled growth was more commonly associated with reactants supplied by diffusion.

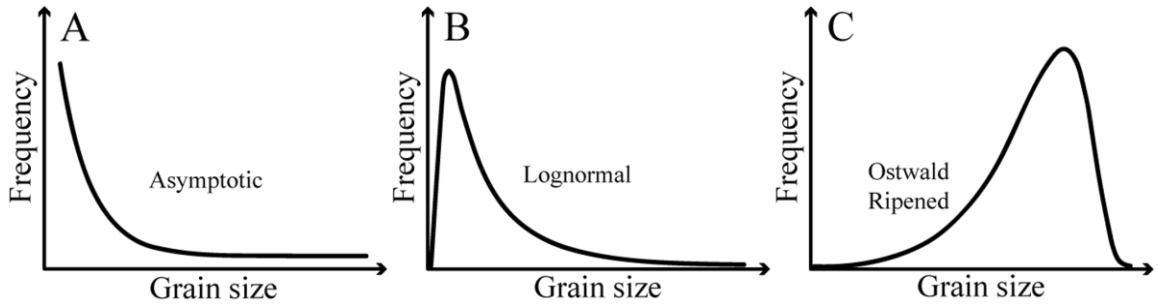


Figure 2.3. Standard shapes of CSDs. A) Asymptotic distribution: an increasing rate of nucleation results in a distribution of crystal sizes that show gratest frequencies of the smallest crystals. Most often seen in igneos systems (Cashman and Marsh, 1988; Marsh, 1988). B) Lognormal distribution: rapid nucleation followed by a decrease in supersaturation state show a distribution where the logarithms of the crystal sizes are normally distributed. If, instead, crystal sizes are plotted, the curve shows a positive skew toward larger sizes. C) Ostwald Ripening: Smaller crystals within a solution constanstly decreasing supersaturation dissolve releasing reactants back to the system to be used by larger, more stable, crystals to grow. Grain size distribution after Ostwald Ripening show a migration from a lognormal distribution to a negatively skewed histogram.

In addition to nucleation and growth, CSDs can also provide critical information on processes of recrystallization broadly referred to as Ostwald ripening (Voorhees, 1992). Ostwald ripening is the process by which larger crystals grow at the expense of smaller crystals, which dissolve and provide reactants back to the system. During the process of Ostwald ripening, the loss of smaller grain sizes and the addition to larger grain sizes results in a shift from the primary lognormal distribution to a negatively skewed histogram (Figure 2.3C; Lifshitz and Slyozov, 1961; Wagner, 1961). Here, smaller crystals with higher specific surface, within a solution constantly decreasing supersaturation, dissolve, releasing material to be used by larger crystals to grow (Kile et al., 2000).

Ostwald ripening in igneous systems results from grain migration and overgrowth during slow cooling and during metamorphism (Higgins, 2011). This crystal coarsening process results in a CSD plot that shows a small-scale downturn in fine grain sizes when CSDs are viewed on a semi-log plot (cf. Higgins, 2006; Marsh, 1998; Marsh, 1988). Ostwald ripening, however, is a much more common process in aqueous systems and can occur even during the earliest diagenesis of precipitated materials. Carbonates, in particular, are highly reactive and strongly affected by the composition of surrounding fluids. Dissolution and reprecipitation reactions likely dominate the early diagenetic stabilization of carbonate phases (Scoffin, 1987). Such reactions occur when chemical disequilibrium is generated in the system by fluids with different chemistry from the one from which carbonates precipitated (Fantle et al., 2020). Within such chemically active systems, continued recrystallization is expected to result in an evolution of the shape of the CSDs.

Crystal Size Distributions and Molar-Tooth Microspar

Because CSDs of chemical precipitates are extremely sensitive to parameters of nucleation, growth, and recrystallization (Kile and Eberl, 2003; Kile et al., 2000; Eberl et al., 1998), they provide a powerful tool to explore the origin of MT microspar. In fact, because of its uniform, limpid, equant, non-interlocking crystals (Kriscautzky et al., 2022; Pollock et al., 2006; Furniss et al., 1998), researchers have used MT as a geologic example of a chemical precipitate that should be readily described using CSDs (Kile and Eberl, 2003). Kile and Eberl (2003), however, were unaware of the two-phase structure of MT microspar.

In exploring the nature of MT microspar, Kriscautzky et al. (2022) used CL petrography to hypothesize several potential pathways for the precipitation and diagenesis of MT microspar. Pollock et al. (2006) described archetypical MT microspar as consisting of subspherical, dully-luminescent cores surrounded by a syntaxial luminescent rim (Figure 2.4A). Kriscautzky et al. (2022) notes, however, that a number of variations also occur. These variations include the presence of rhombic microspar cores surrounded by luminescent rims (Figure 2.4B), zoned sub-spherical to rhombic cores surrounded by luminescent rims (Figure 2.4C), and sub-rhombic cores with a distinct, crescent-shaped region of a different luminescence to that of both core and surrounding luminescent rims (Figure 2.4D). Such variations suggest that MT microspar may reflect discrete differences in the early diagenetic behavior, where different textures reflect differences in the timing

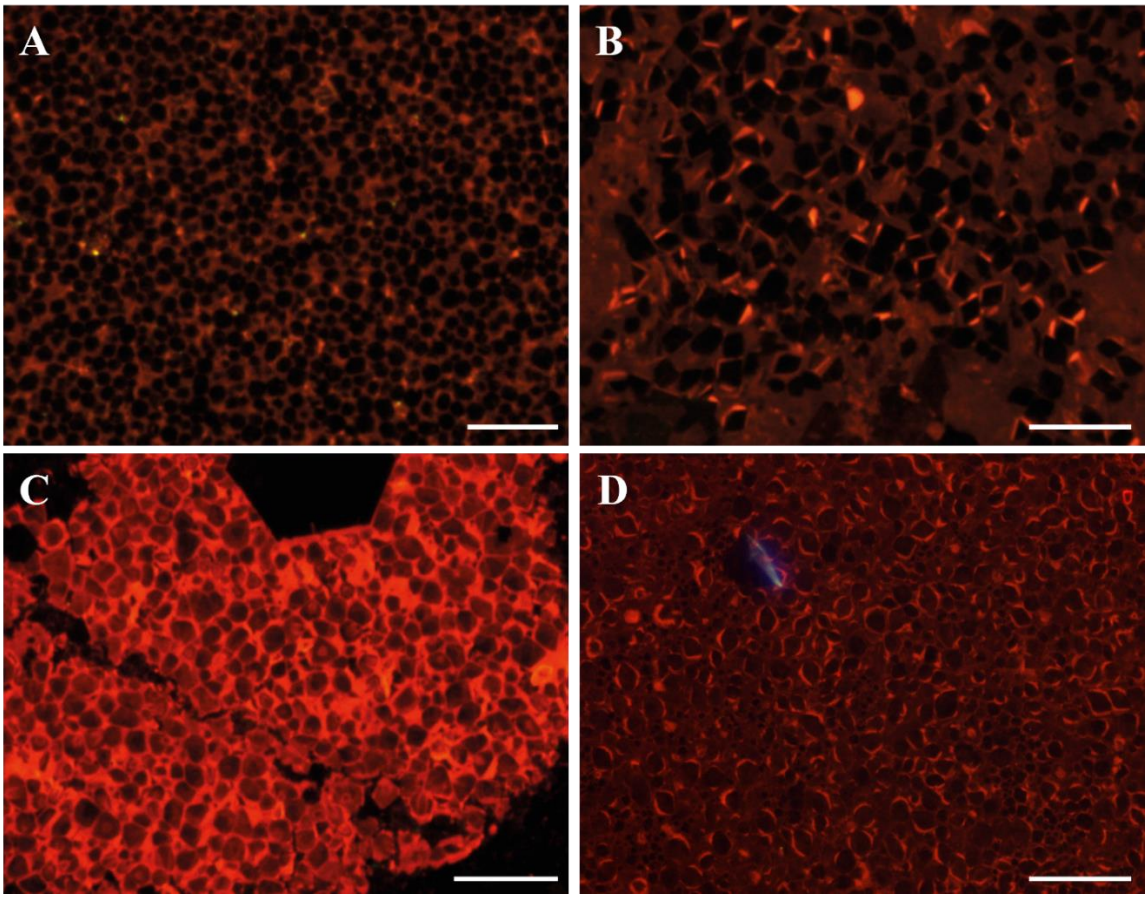


Figure 2.4. Cathodoluminescence photomicrographs. A) Archetypical MT microspar showing subspherical, dully-luminescent cores surrounded by a syntaxial luminescent rim. Mesoproterozoic, Atar Formation, Mauritania B) Rhombic MT microspar cores surrounded by luminescent rims. Mesoproterozoic, Atar Formation (Blue Bed), Mauritania C) Zoned sub-spherical to rhombic cores surrounded by luminescent rims. Also note isolated microspar crystals within the host rock. Mesoproterozoic, Belt Supergroup, Montana, US. D) Subrhombic cores showing a luminescent crescent-shaped region with a different luminescence to that of both the surrounding cement and the core. Upper Mesoproterozoic, Jiayuan Formation, China. Scale bars are 50 μm.

of formation of the cores relative to precipitation of the rims. Kriscautzky et al. (2022) hypothesized that spheroidal unzoned cores with syntaxial rims may represent precipitation of spheroidal amorphous calcium carbonate (ACC) with precipitation of syntaxial rims prior to recrystallization of cores. Rhombic cores (both zoned and unzoned) are then hypothesized to represent conversion of original ACC to a crystalline phase prior to formation of syntaxial rims. Finally, Kriscautzky et al. (2022) suggest that rhombic cores with discrete, luminescent crescental regions may reflect an ACC conversion after precipitation of rims, with crescental regions representing associated volume loss. Independently of the diagenetic process suffered by the MT microspar, once the texture is stable it is virtually nonporous, which makes it extremely resistant to fluid-rock interactions, therefore commonly preserving almost unaltered early diagenetic phases (Kriscautzky et al., 2022).

Samples and data collection

For this study we chose seven samples based on variability identified in the CL characterization of the MT microspar. CL results from light emitted when energy imparted by an electron beam aimed on the surface of a mineral is released. Cathodoluminescence microscopy has been used for decades in the study of carbonate diagenesis because it highlights changes in the trace element composition (Savard et al., 1995; Pierson, 1981) associated with variation in the redox potential (Braithwaite, 2016) and pH (Machel, 1985) of the fluids, among the most important ones. Although a variety of elements can induce luminescence, the main activator in carbonate minerals is Mn^{2+} while the main quencher is Fe^{2+} (Fairchild, 1983; Sommer, 1972; Medlin, 1968; Orgel, 1955). Different shades of the same color have been mostly related to the ratio of quencher to activator (i.e., Fe^{2+}/Mn^{2+}) in the samples (Machel and Burton, 1991; Machel et al., 1991). In this study, MT microspar cores are typically non-luminescent, which reflects a low concentration of both Fe^{2+} and Mn^{2+}, and syntaxial rims range from yellow to red, suggesting enhanced contribution of the primary activator, Mn^{2+} (Savard et al., 1995; Machel, 1985).

Samples were imaged under both CL (Figure 2.5A) and reflected light (RL; Figure 2.5B). Cathodoluminescence permit cores and rims to be clearly distinguished, despite their identical crystallographic structure. Unfortunately, because the rims of different crystals often have an identical CL signature, these images could not be used to identify the outer boundary of each individual microspar crystal. The same samples were therefore imaged under RL which images the surface of the thin section. Furthermore, RL results in images of the microspar that lack the high birefringence at grain boundaries that occurs in traditional transmitted light microscopy and therefore provide clear crystal boundaries that represent the outer edge of the syntaxial rim. From this set of images, ImageJ software (Schneider et al., 2012) was used to measure both cores and the entire microspar crystals (i.e., core plus syntaxial rim; herein referred to as ‘the rim measurements’), as well as the longest axis perpendicular to the primary axis to permit estimation of shape.

In addition to CSDs, we provide quantitative chemical analyses and elemental X-ray maps obtained using two electron microprobes: a JEOL JXA-8230 housed at LAMARX (National University of Córdoba, Argentina) and a CAMECA SX-100 located

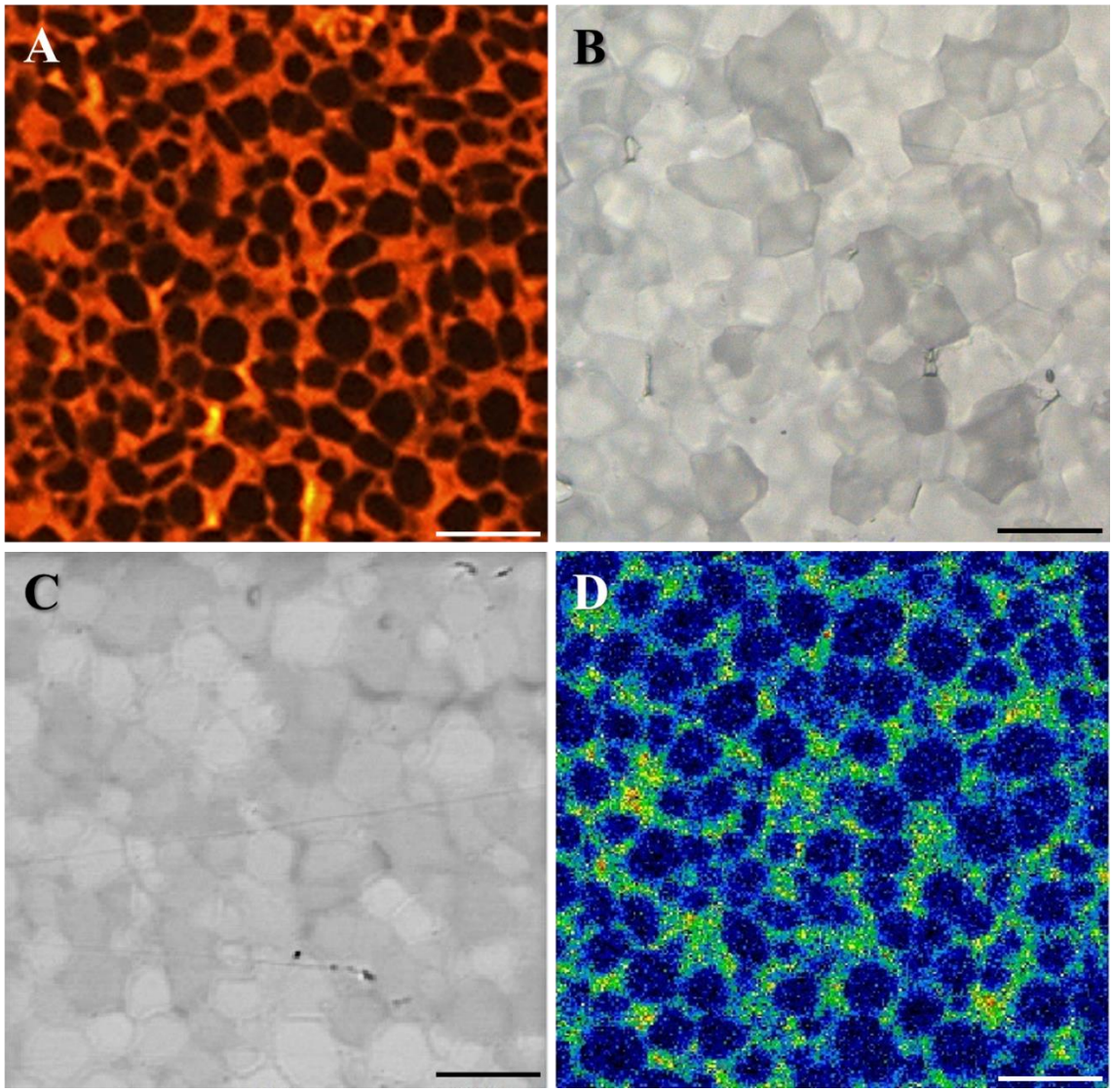


Figure 2.5. Comparison between MT images obtained with different techniques from polished thin section surfaces. A) Cathodoluminescence image where dully-luminescent, subspherical to polygonal cores are easily recognized from the luminescent matrix. Such difference represents variabilities in the trace element composition of each phase. B) Reflected light image with polarizer showing polygonal MT microspar crystal boundaries, not seen under CL. C) Backscattered electron image where crystal edges are recognized due to different shades of grey which are given by crystals oriented in all directions. In these cases, the colors are not related to composition (Lloyd, 1987). D) Elemental X-ray map highlighting Mg concentration variability between cores and rims. Blue cores (subspherical features) are depleted in Mg related to green and yellow areas (rims). Images are not from the same spot. Scale bars are 20 μm.

at the Department of Earth and Planetary Sciences (EPS, University of Tennessee, USA). Point analyses were performed with a voltage of 15 kV and a beam current of 10 nA (LAMARX) or 5kV and 20nA (EPS). The *K*α lines were used, except for Sr and Ba (*L*α) and Pb (*M*α). Counting time on peak and each background position was 5 and 2.5 s for Na, and 10 and 5 s for the other elements. Calcium carbonates are very sensitive to the beam and can lose CO_2 with heating at the point of beam impact. Therefore, two approaches were followed: a defocused beam (as much as 10 µm in diameter) was used whenever possible. However, some features required a focused spot (down to 1 µm) to avoid excitation of adjacent zones of different composition. In such cases, the standard was measured under the same conditions, minimizing the contrast. For carbonates, CO_2 was added (either as CO_2 wt.%= 100 - Σ_{cation} oxides, or by stoichiometry) for accurate matrix corrections. See Appendix II for detailed analytical conditions. Elemental maps were obtained at 15 kV and 1 s dwell time per point, with a beam current of 40 nA (CAMECA) or 50 nA (JEOL).

Results and interpretations

CSDs

Results of CSD measurements (CL and RL) are summarized in Table 1. Measured MT cores have average dimensions of 8.58 ± 2.30 µm (ranging from 2.70 to 17.86 µm), and 7.29 ± 2.05 µm (ranging from 1.94 to 14.55 µm) for their long and short axes, respectively. When long and short axes are plotted (Figure 2.6) the vast majority of the crystals have S/L > 0.66, suggesting a dominantly equant shape. Although care should always be taken when estimating three-dimensional shape from two-dimensional measurements, confidence in the equant nature of MT is supported by the absence of any clear crystallographic orientation: when observed under crossed polars, individual crystals go extinct at different angles and when observed in back-scatter, microspar crystals shows differenced in brightness not related to compositional variations, indicating differences in orientation. Additionally, two of our samples (MTHD-13A and MTHD-13B) are the same rock with thin sections cut perpendicularly to each other.

Similarly, full MT microspar crystals (i.e., core plus syntaxial rim) have average dimensions of 11.05 ± 3.13 µm (ranging from 2.95 to 30.08 µm), and 8.97 ± 2.50 µm (ranging from 2.50 to 23.84 µm) for their long and short axes respectively. Likewise, the cores, when long and short axes of rims are plotted (Figure 2.6) they largely clump between 0.75 to 1. This means the full microspar crystals tend less to be more elongate, although they remain dominantly within the equant field (S/L > 0.67), used in analysis of grain shape (Benn and Ballantyne, 1993; Kellerhals et al., 1975).

Although cores of MT microspar are more clearly equant, rims are not far from them. Cores global mean S/L ratios is 0.85 ± 0.10 (ranging from 0.82 ± 0.12 to 0.89 ± 0.08), whereas rims global mean is 0.82 ± 0.13 (ranging from 0.80 ± 0.15 to 0.85 ± 0.10). It is of special interest to recognize that both cores and rims show exactly repeated mean values with the same standard deviation among samples from different basins (Table 2).

Table 1: Long and short axis mean, median and mode values calculated for each sample in micrometers

Sample	MT Microspar Cores							MT Microspar Cores plus Rims						
	n	Mean		Median		Mode		n	Mean		Median		Mode	
		Long axis	Short axis	Long axis	Short axis	Long axis	Short axis		Long axis	Short axis	Long axis	Short axis	Long axis	Short axis
CHAN31	252	9.37	7.80	9.50	8.05	9.51	9.40	230	8.42	6.72	8.23	6.71	7.96	7.10
CHJI23	254	7.75	6.63	7.84	6.69	10.71	6.36	235	9.57	7.84	9.30	7.88	7.22	4.68
MTHD12	219	7.42	6.24	7.33	8.05	6.32	9.40	201	13.44	10.98	12.83	10.76	8.48	7.23
MTHD13 A	201	8.47	7.22	8.58	7.61	5.27	8.92	300	10.26	8.38	10.01	8.33	11.45	8.36
MTHD13 B	109	9.87	8.75	10.04	8.70	7.46	11.29	240	11.68	9.41	11.71	9.52	14.51	9.70
MTBY	229	9.04	7.31	8.89	7.26	11.72	5.45	143	12.75	9.98	12.10	9.69	13.62	6.98
MTCN3	200	8.15	7.05	8.39	7.30	10.76	7.14	186	11.26	9.50	10.87	9.32	8.59	6.29
Glob. Mean ± St. Dev.		8.58 ± 2.30	7.29 ± 2.05	8.65 ± 2.30	7.67 ± 2.05	8.82 ± 2.30	8.28 ± 2.05		11.05 ± 3.13	8.97 ± 2.5	10.72 ± 3.13	8.89 ± 2.50	10.26 ± 3.13	7.19 ± 2.50

CHAN31: Neoproterozoic, Anhui Province, China. CHJI21: Mesoproterozoic, Jiansu Province, China. MTHD12, MTHD13A, and MTHD13B: Mesoproterozoic, Belt Supergroup, Montana, US. MTBY: Mesoproterozoic, Angmaat Formation, Bylot Island, Canada. MTCN: Iqquittuq Formation, Baffin Island, Canada.

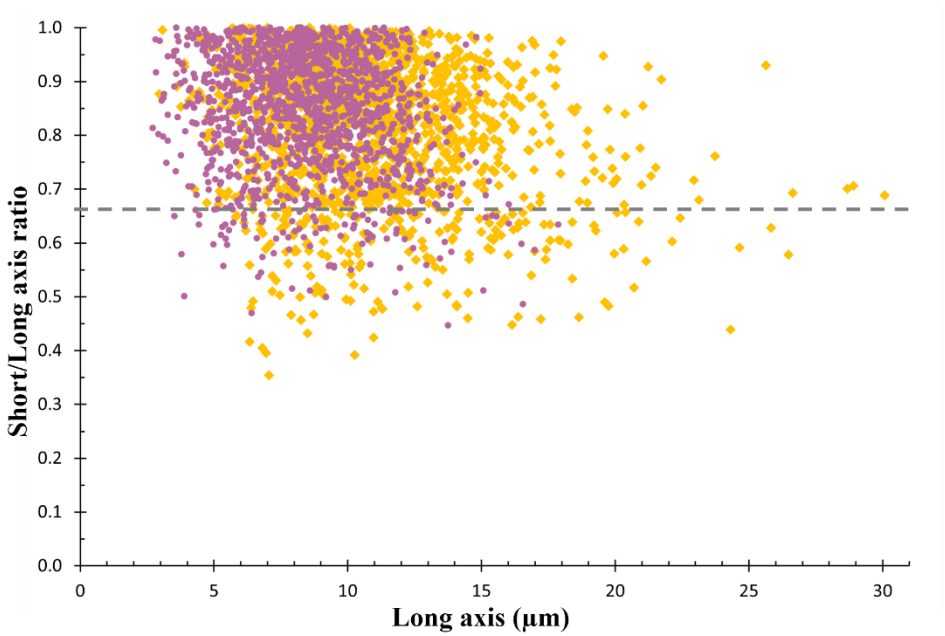


Figure 2.6. Distribution of the Short/Long axis ratio versus the long axis. Pink (circles) represent MT cores, and yellow (diamonds) represent the whole crystal (core plus rim). Observe how the distribution of the cores remains within the cloud of the whole crystal. Dotted line at 0.66 ratio shows the arbitrary limit from which higher values (closer to 1) are considered equant shapes, and lower values (closer to 0) are not equant. Although variability is observed, average core shapes are equant, with only a few dots falling out of this range. Whole crystals show a wider range, although, as with cores, the higher density of points falls within equant proportions. Refer to Appendix III (Figure 4.1) for graphs of individual samples.

Table 2. Mean short/long axis ratios and standard deviation of molar-tooth cores and cores plus rims.

Sample	Cores		Cores plus Rims	
	Mean	**St. Dev.**	**Mean**	**St. Dev.**
CHAN31	0.84	0.11	0.80	0.15
CHJI23	**0.86**	0.10	**0.83**	0.13
MTHD12	0.85	0.11	**0.83**	0.12
MTHD13A	**0.86**	0.11	**0.83**	0.12
MTHD13B	0.89	0.08	0.81	0.13
MTBY	0.82	0.12	0.80	0.13
MTCN	**0.86**	0.11	0.85	0.10
Global mean	0.85	0.10	0.82	0.13

CHAN31: Neoproterozoic, Anhui Province, China. CHJI21: Mesoproterozoic, Jiansu Province, China. MTHD12, MTHD13A, and MTHD13B: Mesoproterozoic, Belt Supergroup, Montana, US. MTBY: Mesoproterozoic, Angmaat Formation, Bylot Island, Canada. MTCN: Iqquittuq Formation, Baffin Island, Canada.
Bold: cores and rims show exactly repeated mean values with the same standard deviation among samples from different basins.

The similarity in S/L ratio in all samples further suggests that the three-dimensional shape of the cores tend to be close to spherical in shape. Samples MTHD13A and MTHD13B, which represent orthogonal sections of the same rock, show similar S/L ratios, with a slight variation of 0.03. In contrast with microspar cores, MT microspar rims show a slightly lower global mean; however not enough to consider these crystals anything other than equant. This slight difference in shape between cores and rims plausibly results from precipitation of syntaxial rims continuing until remaining open space is filled. Precipitation of carbonate continues until the crystal borders contact surrounding crystals, and pore space is fully occluded. That MT microspar crystals remain nearly equant also suggests that the cores of MT microspar crystals were evenly distributed within the available space.

Interestingly, when plotted as CSDs (Figure 2.7), MT microspar cores show a frequency distribution curve near symmetrical, or mesokurtic. Three out of the seven samples present a negative skew (i.e., the peak tends to be toward larger crystal sizes, with a tail to the left), while another is almost zero (Table 3). The other three, although positive, are less than 0.5. These values are in accordance with a normal steady-state distribution observed to occur as a result of Ostwald ripening growth processes: the CSD becomes more symmetrical as ripening occur, tending to a negative skew, until reaching universal state (Eberl et al., 1998).

By contrast, MT microspar rims (Figure 2.7,) show a subtle, yet positive skew (i.e., a peak toward smaller crystal sizes with a longer tail to the right toward larger crystal sizes); all samples yielding positive skew values. With the exception of one sample that shows a leptokurtic distribution (i.e., more peaked distribution; values are heavily concentrated in the peak, and less so in the tails), the rest are all mesokurtic (i.e., kurtosis closer to zero; data approaches a normal distribution) (Table 3). These results can be interpreted as lognormal distributions, where a positive skew toward larger sizes is observed when frequencies are plotted against crystal size, modified by surface-controlled growth (cf. Kile et al., 2000).

Based on the observed CSDs, nucleation of the MT microspar cores, which was the first step in the formation of MT microspar, likely resulted in a primary, lognormal distribution. This distribution, however, was overprinted during growth by a substantial component of Ostwald ripening. During this process, smaller, less stable cores dissolved to provide the system with reactants that aided in the growth of the larger, more stable cores. Recrystallization and associated Ostwald ripening of the MT microspar cores occurred very rapidly after initial precipitation, prior to the precipitation of syntaxial rims. These syntaxial rims appear to represent a discrete precipitation event, where rapid nucleation was favored (or controlled) by the presence of microspar cores and resulted in a largely lognormal distribution. This was followed by surface-controlled growth, that continued until the rims filled available open space. The filling of available pore space then inhibited later recrystallization, resulting in the maintenance of a lognormal CSD.

Elemental analyses and X-ray maps

Any hypothesis aiming to explain the genesis of MT microspar must consider both textural and chemical characteristics. The same CL petrography that demonstrated the

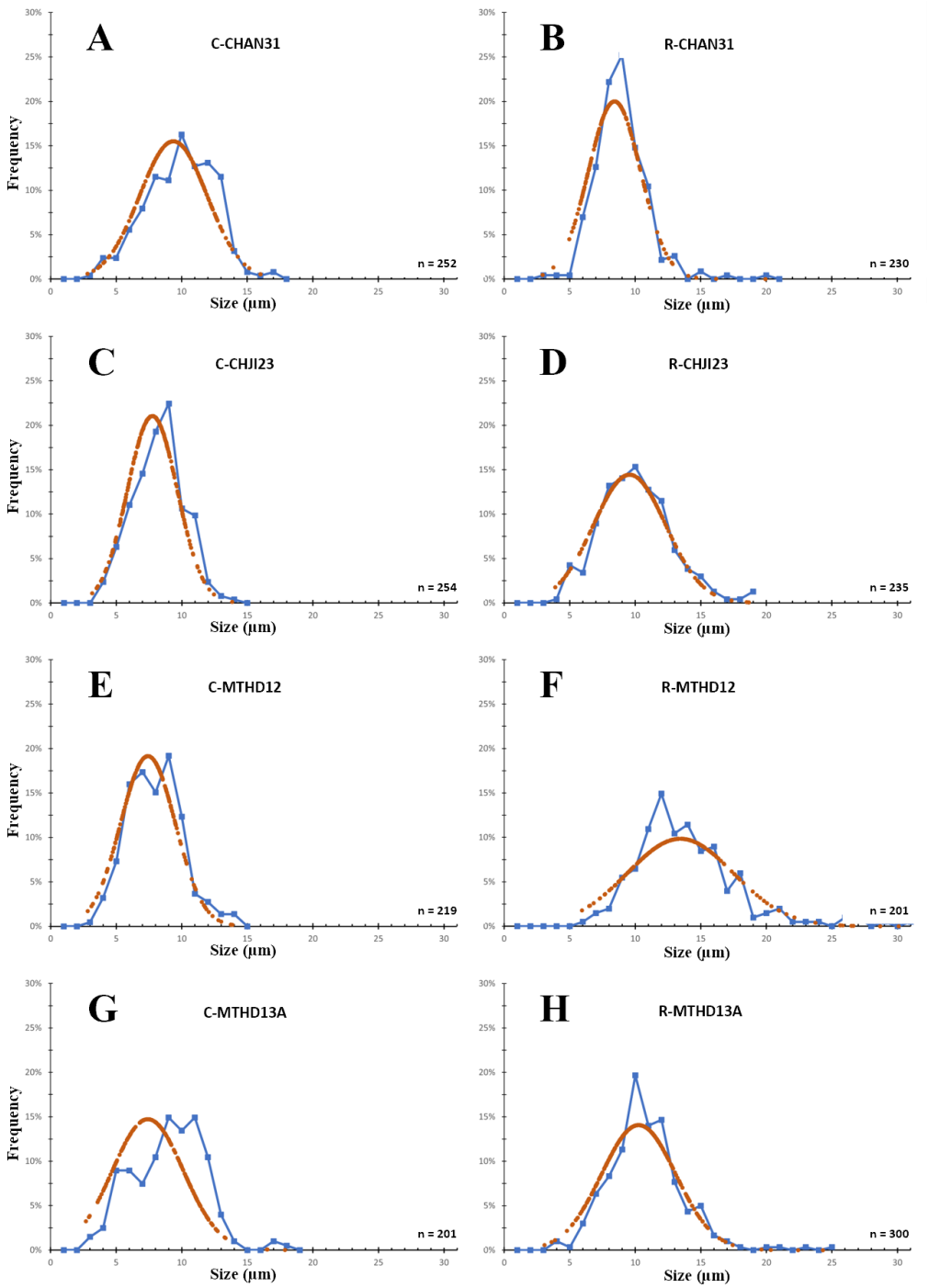


Figure 2.7. Crystal size distributions of MT microspar cores (left) and whole crystals (cores plus rims; right). Blue (continuous line segments) is the frequency distribution of the longest axis. Orange (dotted bell-shaped curve) is the normal distribution for each subset of data points considering the media and the standard deviation. Each horizontal pair of graphs represents one sample. **n,** number of measurements of long axes; **C**, core; **R**, rim (core plus rim).

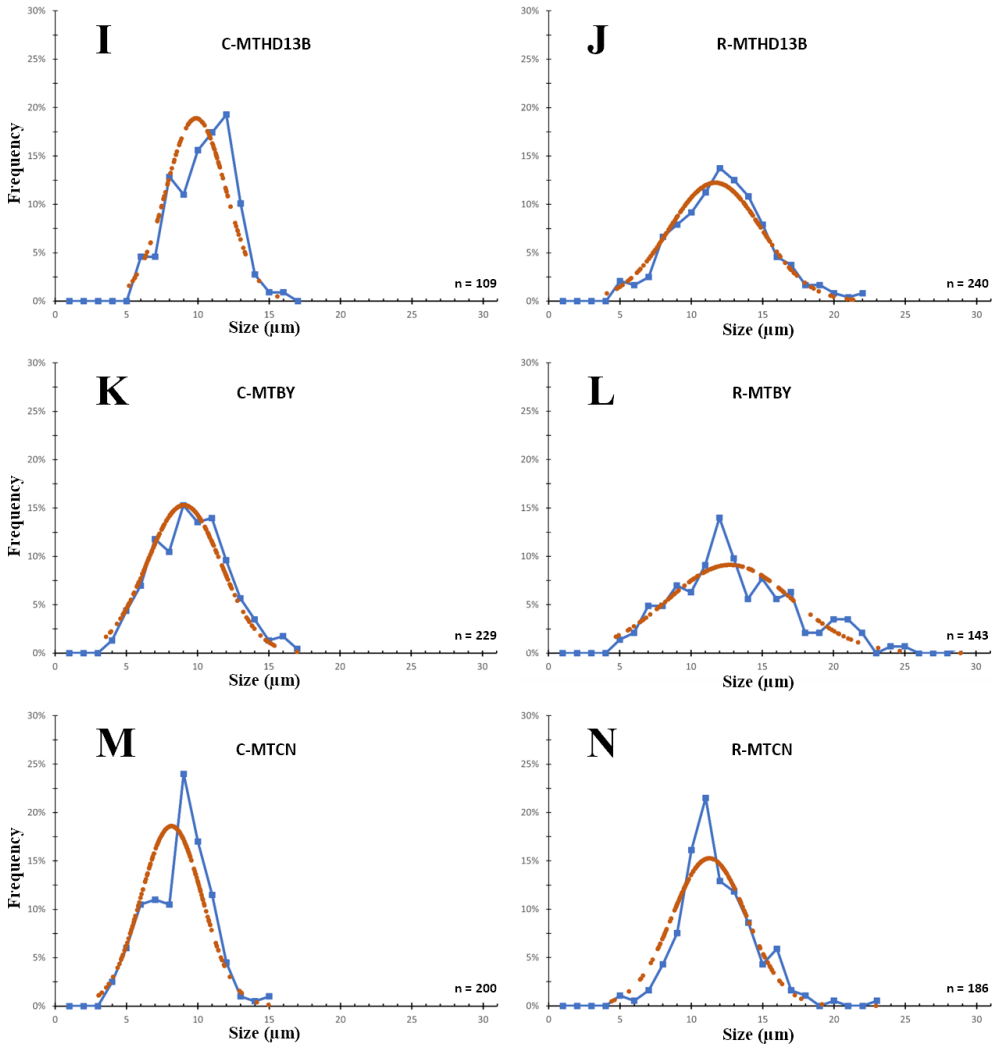


Figure 2.7 continued

Table 3. CSD's skewness and kurtosis of molar-tooth cores and cores plus rims

Sample	Cores		Cores plus Rims	
	Skewness	Kurtosis	Skewness	Kurtosis
CHAN31	-0.19	-0.30	1.29	0.74
CHJI23	0.01	-0.19	0.55	0.24
MTHD12	0.44	0.23	1.30	1.74
MTHD13A	0.15	0.15	0.92	-0.12
MTHD13B	-0.15	-0.33	0.29	-0.21
MTBY	0.29	-0.23	0.72	0.60
MTCN	-0.01	0.04	0.67	0.60
Global mean	0.08	-0.09	0.82	0.51

CHAN31: Neoproterozoic, Anhui Province, China. CHJI21: Mesoproterozoic, Jiansu Province, China. MTHD12, MTHD13A, and MTHD13B: Mesoproterozoic, Belt Supergroup, Montana, US. MTBY: Mesoproterozoic, Angmaat Formation, Bylot Island, Canada. MTCN: Iqquittuk Formation, Baffin Island, Canada.
CSD: Crystal size distribution

contrasting chemical nature of MT microspar, for instance, requires that there be a fundamental difference in chemistry between the cores and their syntaxial rims. Here we explore and quantify the compositional difference between core and rim phases using microprobe point analyses and X-ray elemental maps (Figure 2.8).

The composition of MT microspar from the different localities sampled in this study has subtle differences, but all of them share some common features. Regardless of the age or geographic locality of the sample, the MT microspar always shows the same nature with spheroidal to rhombic cores surrounded by a syntaxial rim. CL images show that the boundary between the core and rim is sharp (i.e., occurring over much less than 0.5 μm), at least for CL activators (cf. Figure 2.4A). However, the core-to-rim ratio (by volume) is not constant, nor is the width of the rim. Most commonly, when the core is rounded or rhombic, the rim width is approximately constant all around, but in the most extreme cases (cf. Figure 2.4B, D), the core of the MT microspar can be represented by a combination of a distinct rhomb with crescental segments.

Unfortunately, CL provides only a non-quantitative assessment of the relative contribution of activators and quenchers. Electron microprobe analysis provide the opportunity for a much more detailed look at the distribution of minor and trace metals within MT microspar (Figure 2.8). The composition of MT microspar from the different localities sampled in this study has subtle differences, but mainly share some common features. Figure 2.8 shows 3 maps of the same region, for two different microspar samples, accompanied with a backscattered electron (BSE) image.

In most cases BSE permits the identification of individual MT microspar crystals by showing different shades of grey due to different orientations of the crystals (Figure 2.8, top left; Lloyd, 1987). Microspar cores are shown by different concentrations of metals present in the calcite crystals: a general trend is observed among the samples where cores are depleted in Mg, and the surrounding rims are relatively enriched (Figure 2.8, top right). Strontium maps show variabilities, from clear cores depleted in Sr and rims relatively enriched, to the opposite, to even homogeneous Sr values (Figure 2.8, bottom left). Similarly, Fe shows a similar trend to Sr, showing cores depleted, and rims relatively enriched, although some samples produce a homogeneous map (Figure 2.8, bottom right).

Our microprobe data shows that calcite from MTS is rather pure $CaCO_3$, with minor amounts of Mg (up to 0.61 wt.% MgO, but more frequently in the 0.2-0.3 wt.% range), Mn (≤ 0.10 wt.% MnO), Fe (≤ 0.19 wt.% FeO) and Sr (≤ 0.43 wt.% SrO). The quantification of low abundance metals in MT microspar, however, is difficult for several reasons: First, calcite is unstable under the focused electron beam, due to loss of CO_2, and there is therefore a trade-off between spatial resolution and analysis quality. Second, the concentration of these metals is usually less than 0.1 wt. % range (except for Mg, that may be less than 0.1 wt.% range); typical errors for the microprobe introduce dispersion for such low quantities. Finally, grain boundaries at the outer edge of the rims are not clearly visible, in the element maps, as there is no compositional contrast. Fortunately, differential electron channelling for grains in various crystallographic orientations create a contrast which is not related to atomic number, so the localities of grain boundaries can be inferred from backscatter images (Lloyd, 1987). Calcite also occurs along with MTS but with an unrelated origin. It can be found as masses of lath-shaped prisms, growing perpendicular

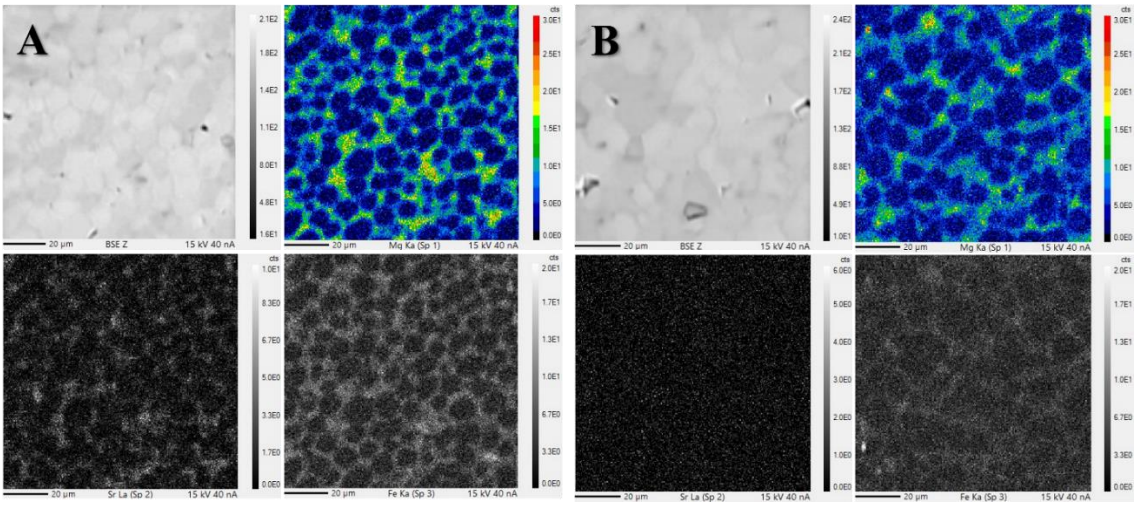


Figure 2.8. Backscattered electron images and elemental X-ray maps. Each panel presents a set with backscattered electron images (top right), and elemental X-ray maps of Mg (top right), Sr (bottom left), and Fe (bottom right). Observe how Mg maps highlight cores and rims constantly. Sr and Fe maps, however, are more subtle, and not as constant throughout all samples analyzed. A) CHAN31, Neoproterozoic, Anhui Province, China. B) MTHD12, Mesoproterozoic, Belt Supergroup, Montana, US.

to vein walls, between the matrix and the MTS filling. Veins of late granular calcite, crosscutting both MTS and matrix, are also texturally distinct, and lack the typical core-and-rim internal structure of MT. In addition to their textural features, late calcite (either tabular crystals or vein fillings) also shows distinct differences with MT calcite, being richer in Fe, Mg, Mn, and Sr.

In summary, from analysing maps and point analyses, minor and trace metals have a heterogeneous distribution: rims are enriched in Mg (with a single exception) and Fe. Strontium may be slightly enriched either in the rims or in the cores, or may be relatively homogeneous, whereas Mn is enriched in the rims. Calcite is pure with only minor concentrations of Mg, Mn, Fe, and Sr, and traverses made across veinlets show that there is no significant variation in chemical composition. Most often, however, cores show a general depletion in trace metals, while the syntaxial rims are generally enriched. The clear boundary existing between cores and rims, in addition to the different composition, indicates that cores crystallized prior the crystallization of the syntaxial rims. As cores crystallized and supersaturation decreased, less compatible elements remained in the fluid. Later crystallization of the rims, nucleating in the previously crystallized calcite cores, would incorporate the remaining trace elements.

It is interesting to note that the compositional patterns observed in MT cores and rims remain intact even when disrupted by clearly later diagenetic phases. Dolomite crystals crosscut the MT fabric, meaning they are of a late origin (Figure 2.9). Their chemical compositions vary according to the locality. MTBY dolomites contain some Fe (0.48-0.67 wt.% FeO; average 0.58) and traces of Mn (from below the microprobe detection limit up to 0.08 wt.% MnO; average 0.03). Other elements that may be present in dolomite (Ni, Zn) are usually below the detection limits. At this locality dolomite is slightly Ca-rich [1.07-1.08 Ca *apfu* (atoms per formula unit), compared to the ideal formula with 1.00 Ca *apfu*). Dolomite crystals have experienced a dissolution and reprecipitation process, with the development of porosity and formation of calcite blebs (with size inversely proportional to abundance; Figure 2.9Aa) within a matrix of dolomite which more closely approaches the ideal chemical formula (Ca between 1.00 and 1.04 *apfu*; Figure 2.9Ab).

By contrast, rims of dolomite crystals at MTCN are much more Fe-rich (5.98-6.79 wt.% FeO; average 6.48). Fe replaces Mg, as the Ca content (in *apfu*) is relatively even. They also contain more Mn (0.31-0.61 wt.% MnO; average 0.44). Dolomite from this area is slightly Ca-rich (1.02-1.09 Ca *apfu*, average 1.04), but there is no regular trend between core and rim. The chemical contrast, the irregular contacts between altered and unaltered zones, and the fact that the outer zone is euhedral and lacks alteration, suggests that there were at least two stages of dolomite precipitation, separated by an interval where the first crystals interacted with fluids that caused dissolution and reprecipitation, coupled with increased porosity. This is also shown by CL, with darker cores showing irregular, lobate contacts with a bright luminescent euhedral rim (Figure 2.9B). In some crystals these sequences appear more than once, indicating fluctuation of the fluid composition. These observations provide evidence that late diagenetic fluids responsible for dolomitization of the matrix can disrupt MT microspar (probably dissolving it by force of crystallization of

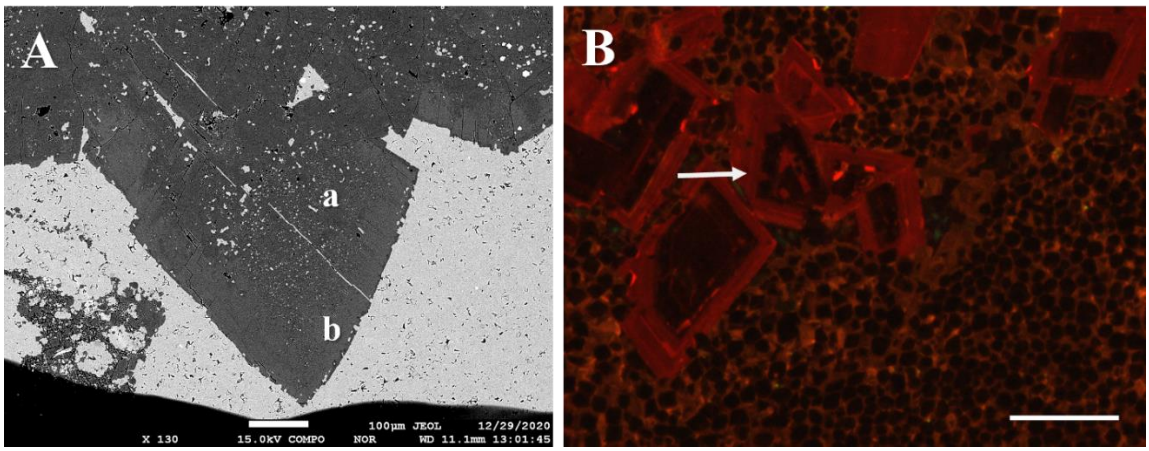


Figure 2.9. Backscattered electron image and CL photomicrograph of dolomite crystals crosscutting MT microspar. A) Zoned dolomite, slightly Ca-rich with some Fe and traces of Mn. **a**, core showing dissolution and reprecipitation of calcite within a matrix of dolomite. **b**, homogeneous euhedral dolomite rim not showing calcite blebs. B) Zoned dolomite crystals within vein filled with MT microspar. Arrow points to lobulated inner zones of the crystal showing dissolution processes before crystallization of the outer rims. Scale bar in B is 20 µm.

the dolomite), but that it is not associated with the wholesale recrystallization of the MT microspar.

DISCUSSION

Regardless of the initial mechanism responsible for the formation of MT voids, the microspar that fills these voids is incredibly similar in both morphology and in the incorporation of minor and trace metals. Samples examined in this study range in age from the Mesoproterozoic (Belt Supergroup, US, 1.4 Ga) to the early Neoproterozoic (Zhangqu Formation, China, ~0.94 Ga). During this nearly 500 million years interval, the Earth's oceans experienced large changes in redox structure and isotopic composition. Such changes reflect dramatic changes in the Earth's carbon cycle, represented by carbon isotope compositions that remain near 0‰ from 1.6 to 1.2 Ga, before showing moderate variation between -1‰ and +3‰ from 1.2 Ga to the end of the Mesoproterozoic, and a change to extreme fluctuations between -5‰ and +8‰ in the early Neoproterozoic (Kah and Bartley, 2021; Halverson et al., 2010; Halverson et al., 2005; Kaufman and Knoll, 1995). During this same time, the Sr isotope composition of the oceans—which reflects a balance between input of non-radiogenic strontium from weathering of young mid-ocean ridges and radiogenic strontium from weathering of ancient continental crust (Tan et al., 2021; Burns et al., 1994; Veizer, 1989)—experiences a dramatic shift from 87/86 Sr compositions near 0.7055 to 7095 (Halverson and Hurtgen, 2007). This period also includes at least one global oxygenation event that resulted in widespread changes in the composition and distribution of redox sensitive elements in the Earth's oceans (Gilleaudeau et al., 2016; Gilleaudeau and Kah, 2013; Reinhard et al., 2013; Lyons et al., 2009; Canfield et al., 2007).

Previous work using MT microspar demonstrates that the isotopic composition of MT microspar commonly reflects that of the global ocean signature at the time (Kah et al., 2012; Pope et al., 2003; Frank and Lyons, 1998). This observation suggests that the primary fluid responsible for the generation of MT microspar must be seawater (see also Bishop and Sumner, 2006; Pollock et al., 2006). Because MTS forms in the shallow substrate (Hodgskiss et al., 2018; Pollock et al., 2006; Marshall and Anglin, 2004; Frank and Lyons, 1998; Furniss et al., 1998), however, we must consider that the fluids from which MT microspar precipitated may also reflect a combination of oxic seawater, dysoxic seawater, and anoxic pore fluids. Microprobe elemental analysis of Mn and Fe, the most widely used indicators for diagenesis in the presence of reducing fluids (Brand and Veizer, 1980), shows that both elements are relatively enriched in the syntaxial rims, and depleted in the cores. Manganese and Fe are essentially absent from MT cores and restricted primarily to the rims of the MT microspar. In addition, Mn is less abundant than Fe, but Mn is a strong activator, which is apparent from the activation of bright orange luminescence observed in the regions surrounding the cores. MT calcite shows Sr $\leq$ 4300 ppm, Mg up to 6100 ppm, Fe $\leq$ 1900 ppm, and Mn $<$ 1000 ppm. As Sr is mostly seen in the rims, it can be interpreted that early crystallization of the cores expelled Sr to the remaining fluid, but later diagenetic processes did not affect the cores already crystallized (Gilleaudeau and Kah, 2013). The absence of elevated concentrations of Mn and Fe therefore suggest that dysoxic to oxic seawater is the primary constituent of microspar-forming fluids (seawatewer or formational

porewaters; Gilleaudeau and Kah, 2013; Kah et al., 2012). This is also consistent with preliminary data looking at the Ca/I ratios of MT microspar (Dalton Hardisty, personal communication) and with the inferred environmental setting of MTS within shallow, wave-swept carbonate platforms (James et al., 1998).

This scenario, however, fails to explain why MT microspar precipitated rapidly (i.e., prior to closure of fractures) to fill substrate voids, when the substrate itself remained cohesive, yet unlithified. Here, I suggest it appears to be the mixing of seawater with small amounts of substrate pore fluid that may be responsible for triggering the immediate precipitation of carbonate cement within substrate voids. Microbial reactions within the substrate can result in changes in pH, alkalinity, and dissolved inorganic carbon. Bergmann et al. (2013) provides a detailed analysis of these processes, from which the most important ones related to a change in alkalinity (ΔALK) and carbonate saturation are summarized as follows. Iron reduction is the process that increases alkalinity the most (ΔALK = 9.7), with a subsequent increase in the carbonate saturation state of the substrate, followed by Mn reduction (ΔALK = 4.9). Both processes produce, therefore, alkaline pH values. Others, in the neutral to slightly negative pH values, are sulfate reduction (ΔALK = 1.2) and denitrification (ΔALK = 1.0). Finally, anaerobic oxidation of methane gives a slightly alkaline pH with an increase in alkalinity (ΔALK = 1.2). Reactions that involve the degradation of microbial EPS can also release metal cations such as Ca and Mg to the surrounding pore fluid (Dupraz et al., 2009; Visscher and Stolz, 2005), which will also increase local carbonate saturation. The presence of organic matter within pore fluids can also act as a substrate for carbonate precipitation that aids in the stabilization of nuclei (Bots et al., 2012). The combination of these factors all favor to an increased carbonate saturation within voids that experience a mix of oxic seawater and primarily anoxic pore fluids. The spontaneous mixing of fluids with contrasting pH and alkalinity in absence of inhibitors (such as SO_4; Bots et al., 2012) and in presence of dissolved organic matter (cf. Goodman and Kah, 2007) would be expected to trigger the carbonate nucleation. In samples where MT microspar is observed within the host rock matrix (cf. Kriscautzky et al., 2020) the density of MT microspar in the matrix is highest near the edges of MT ribbons, suggesting that locally enhanced permeability permits diffusion of seawater from the cracks into the matrix, triggering MT microspar precipitation within the host rock matrix. In all cases, the generally outstanding petrographic preservation of MT microspar suggests that permeability was readily occluded and that regions dominated by MT microspar remained almost impermeable to later diagenetic recrystallization.

Kriscautzky et al. (2022) hypothesized that MT microspar may have precipitated from or within a gel phase. Such gels can form naturally upon the rapid precipitation of carbonate minerals, where they often occur as amorphous calcium carbonate (ACC)—a hydrated metastable precursors to crystalline calcium carbonate phases (Rodriguez-Blanco et al., 2012). In addition to preserving MTS voids due to their semisolid nature, gels would have also allowed the cores of MT microspar to remain suspended while the rims formed around them. In this scenario, rapid precipitation of hydrated ACC incorporates a variety of non-Ca ions, including Mg^{2+}. The rapidity of precipitation, however, precludes Mg from dehydration prior to incorporation into the ACC, resulting in a hydrated carbonate phase surrounded by bound water (cf. experimental results of Goodman and Kah, 2007).

Combined results of CSD and geochemical analyses provided here lend support to the hypothesis of a gel phase as a precursor. First, petrographic observations suggest that the cores of MT microspar originated as a spheroidal carbonate, which are prevalent in the precipitation of ACC (Bots et al. 2012). Research shows that calcium carbonate crystal nuclei form as nanoparticles that later grow, by aggregation to form polycrystalline spheres (Shen et al., 2006; Vacassy et al., 2000), or the dehydration and recrystallization of ACC (Rodriguez-Blanco et al., 2012; Pouget et al., 2010; Andreassen, 2005). Both petrographic observations and CSDs then confirm that cores underwent rapid recrystallization and Ostwald ripening, which would be expected during the transformation of ACC—via a combination of dehydration and dissolution and reprecipitation, to a more stable calcite mineralogy (Bots et al. 2012).

A model of MT microspar precipitation within a gel phase is also supported by the relative behavior of cores and rims during crystal growth. In lab experiments, Kile and Eberl (2003) showed that micrometer-sized calcite crystals (which is the scale observed in MT microspar cements) were most often produced by proportionate growth, in which ions are supplied to the site of precipitation by advection. Such growth process produces a lognormal CSD. CSD's of the syntaxial rims of MT microspar are dominantly lognormal and show no evidence of Ostwald ripening. This pattern is therefore consistent with the nucleation of this secondary carbonate growth phase (rim) limited by the availability of cores, and growth within a gel environment that reduced fluid motion resulted in diffusion-controlled growth. Together, these observations suggest that the MT cores nucleated from a supersaturated solution and favored production of a gel that resulted from the incorporation of hydrated ions into the ACC. Recrystallization and Ostwald ripening of this nucleation phase would have expelled minor elements from the stabilized carbonate crystal lattice, resulting in metal enrichment of the surrounding non-crystalline phase. The even distribution of MT cores within available space—with cores only rarely touching each other and generally uniformly separated by only a few microns—suggests that a gel phase was likely retained at this stage. Following this initial process, a later cement phase grew in crystallographic continuity upon the cores. The syntaxial nucleation of these latter growth stages also supports that the driving force behind the nucleation of MT rim cements was the presence of precursor cores, rather than a critical level of supersaturation. MT rims could, therefore, have grown at lower levels of saturation. The maintenance of the lognormal CSD through growth of the rims, with no evidence of modification by Ostwald ripening, suggests that this phase filled the remaining open void space, effectively occluding both porosity and permeability of the MT voids.

Interestingly, Kile and Eberl (2003) described preliminary CSDs from MT of the Mesoproterozoic Belt Supergroup—samples analogous to the ones in this study. Kile and Eberl (2003), however, used only plane light petrographic images of MT microspar for their study—they were unaware at the time that MT microspar represented crystal growth in two episodes, cores and syntaxial rims. The authors observed evidence for surface-controlled growth, although their CSD graphs were not fully consistent with this observation: the curves appeared to reflect an element of Ostwald ripening but were generally more narrow than would be expected for a phase undergoing Ostwald ripening. To explore this inconsistency, Kile and Eberl (2003) assumed "breaking points" where the

crystallization process changed from nucleation with proportionate growth, to Ostwald ripening, ending with surface-controlled growth. They based this hypothesized pathway on results obtained from mathematical simulations and subtracted the final crystal size from the point at which surface controlled growth would have to start to support the shape of their CSD. By doing this, they restored the Ostwald steady-state normal shape and concluded that the final CSD shape would be obtained by a process in which rapid nucleation occurred under high degrees of supersaturation and was followed by minor proportional growth and Ostwald ripening. Once the supply of available ions became limited, surface-controlled growth would continue.

This prescient work by Kile and Eberl (2003)—which relied on the theoretical understanding of CSD form—has largely been confirmed by a combination of petrographic observation, elemental analyses, and the measurement of CSDs of both the core and rim phases of MT microspar. MT cores nucleated rapidly in a supersaturated medium and underwent Ostwald ripening processes (cf. Fig 7). These cores produce a steady-state curve slightly skewed toward smaller crystal sizes indicative of Ostwald ripening. The CSD's of MT microspar cores are therefore analogous to the hypothetical results obtained by Kile and Eberl (2003). Eberl and Kile (2005) even suggest that this initial phase would have halted when crystals reached approximately 5 microns in diameter, which is close to the average size of 8.58 ± 2.30 and 7.29 ± 2.05 (long and short axis, respectively) of MT cores (Table 1). The CSD of the final MT microspar crystals (MT cores plus syntaxial rims) ultimately produce CSDs consistent with lognormal curves yet shifted a bit closer to the gaussian curve (cf. Fig 7). This pattern is consistent with a limited nucleation followed by surface-controlled growth, with crystallization ending with the closure of the remaining pore space.

Finally, detailed cathodoluminescence analysis (Kriscautzky et al., 2022, this work) show that the MT microspar consists of non- to dully-luminescent cores surrounded by a luminescent syntaxial rim typically in shades of orange to red. Elemental maps show that microspar cores are depleted in Mg, Sr, and Fe, and rims enriched in these elements. These observations support the hypothesis proposed by Kriscautzky et al. (2022) that syntaxial rims may incorporate ions released by ACC cored during recrystallization and stabilization as low magnesium calcite.

ACC is water-rich, containing up to 20% water by weight (Michel et al., 2008). Therefore, the crystallization to anhydrous carbonate must have released an important volume of fluids containing water and metals (Fe, Mn, Mg, Sr) that favored the precipitation of the rims, and at the same time the voids must have collapsed to adjust to the volume loss. CSDs suggests that the crystal growth history of MT microspar started with rapid nucleation and Ostwald ripening, leading to the dissolution of the smaller nuclei. The remaining crystals then grew by a proportionate growth mechanism, where larger nuclei had higher growth rates, further skewing the CSD toward larger crystals. In most cases, petrographic evidence suggests that this ripening process occurred prior to the formation of syntaxial rims. These syntaxial rims are compositionally distinct from initial cores, showing both luminescence and enrichment in Mg, Sr, Fe, and Mn which plausibly reflect expulsion of these elements from the primary ACC phase during recrystallization. This scenario also aids in the explanation of unusual MT crystals that show three phases:

cores, rims, and distinct luminescent crescent patches that occur between cores and rims. In the scenario provided here, syntaxial rims would have formed prior to the stabilization of MT cores. Continued dehydration and stabilization of MT cores then resulted in a volume loss and fluids trapped spaced the cores and the respective rims. These fluids would be expected to be highly enriched in trace metals, which is consistent with their strongly yellow luminescence.

Despite the evidence presented here for early diagenetic recrystallization history of MT microspar, we suggest that the combination of core and rim phases reflect a single primary fluid composition. The dynamics of precipitation and recrystallization presented here demonstrate the complexity of carbonate formation and diagenesis during early seafloor stabilization. Combined, however, these two features, cores and syntaxial rims, should adequately represent the bulk composition of the fluid from which it precipitated. Furthermore, the abrupt shift in composition between core and rim phases indicates that neither dissolution nor diffusion played an important role after the formation of these microsparitic grains, and that the dissolution and reprecipitation processes experienced by the microspar cores occurred prior to the precipitation of the rims and acted as a mechanism for chemically segregating the void fluids. The micron-scale preservation of this segregation favors earlier interpretation that MT microspar (when measured as a bulk phase) may preserve evidence of primary Proterozoic fluid chemistries (Kriscautzky et al., 2022; Kah et al., 2012; Bishop and Sumner, 2006; Pollock et al., 2006; Pope et al., 2003).

CONCLUSIONS

- Molar-tooth microspar is clearly composed of two features easily distinguishable by their differences in trace elements composition: subspherical to polygonal, equant cores, and syntaxial rims. Cathodoluminescence and X-ray elemental maps provide useful ways to recognize these differences at a relatively low cost.

- Crystal size distributions of MT micrite cores show a generalized subtle Ostwald Ripened growth, where after precipitation of original cores, the smaller, less stables ones dissolved to allow larger, more stable crystals to grow. Additionally, CSD of the whole crystals (cores and core plus rims) yield a lognormal to normal distribution, indicating surface-controlled growth from the already precipitated cores, until all the available open space was filled.

- Elemental analyses of MT microspar shows a clear, sharp edge between cores and rims, with no diffusion in between them. This is also observed qualitatively under CL. This, together with other petrographic observations, suggest that the cores were fully crystalline before the rims precipitated.

- Fabric destructive zoned dolomite crystals present a porous, recrystallized core, with a non-porous, homogenous rim. The zones, observed under CL, also present lobulated areas. These features indicate dissolution-reprecipitation processes that occurred

during the diagenesis of these rocks and has been clearly recorded by the dolomites. Surprisingly, MT microspar related to these crystals do not show such clear visual indications of diagenetic processes. This can be related to the extremely low porosity and permeability of the MT microspar after precipitation.

- Elemental analysis further support precipitation of MT microspar from ACC within a gel phase. The distribution of trace elements (Fe, Mg, Mn, and Sr) shows a generalized trend with relatively low concentrations in the cores, and higher concentrations in the rims. These particular concentrations can be related to expulsion of less compatible elements when the cores precipitated in an open, supersaturated environment. As supersaturation decreased, the rims, in a fluid enriched in trace elements, nucleated on the surface of the previously precipitated cores, and grew by surface-controlled processes. Whether ACC precipitates directly from amorphous to calcite, or this happens through an unstable polymorph requires further investigation.

ACKNOWLEDGEMENTS

I want to thank my advisor, Dr. Linda Kah, and my committee members, Dr. Anna Szynkiewicz, Dr. Molly McCanta, and Dr. Julie Bartley, for their time and commitment to improving this chapter. In addition, I would like to thank Dr. Fernando Colombo for their invaluable knowledge and the time he advocated to help me interpret the vast microprobe database collected both in LAMARX and EPS. Finally, I want to acknowledge Allan Patchen for his technical support and data collection.

REFERENCES

Andreassen, J., 2005. Formation mechanism and morphology in precipitation of vaterite—nano-aggregation or crystal growth? Journal of Crystal Growth 274, 256-264.

Algar, C.K., Boudreau, B.P., 2010. Stability of bubbles in the linear elastic medium: Implications for bubble growth in marine sediments. Journal of Geophysical Research: Earch Surface 115, 1-12.

Baronnet, A., 1982. Ostwald ripenning in solution: the case of calcite and mica. Estudios geológicos 38, 185-198.

Benn, D.I., Ballantyne, C.K., 1993. The description and representation of particle shape. Earth Surface Processes and Landforms 18, 665-672.

Berger, A., Herwegh, M., Schwarz, J.-O., Putlitz, B., 2011. Quantitative analysis of crystal/grain sizes and their distributions in 2D and 3D. Journal of Structural Geology 33, 1751-1763.

Bergmann, K.D., Grotzinger, J.P., Fischer, W.W., 2013. Biological influences on seafloor carbonate precipitation. Palaios 28, 99-115.

Bertrand-Sarfati, J., Plaziat, J., MoussinePouchkine, A., 1997. Vermicular structures in the Neoproterozoic of the West African Craton: Microbialites versus 'molar tooth'. Facies 36, 231-234.

Bishop, J.W., Sumner, D.Y., 2006. Molar tooth structures of the Neoarchean Monteville Formation, Transvaal Supergroup, South Africa. I: Constraints on microcrystalline $CaCO_3$ precipitation. Sedimentology 53, 1049-1068.

Bishop, J.W., Sumner, D.Y., Huerta, N.J., 2006. Molar tooth structures of the Neoarchean Monteville Formation, Transvaal Supergroup, South Africa. II: A wave-induced fluid flow model. Sedimentology 53, 1069-1082.

Bots, P., Benning, L.G., Rodriguez-Blanco, J.-D., Roncal-Herrero, T., Shaw, S., 2012. Mechanistic Insights into the Crystallization of Amorphous Calcium Carbonate (ACC). Crystal Growth & Design 12, 3806-3814.

Boudreau, B.P., 2012. The physics of bubbles in surficial, soft, cohesive sediments. Marine and Petroleum Geology 38, 1-18.

Braithwaite, C.J.R., 2016. Cathodoluminescence in Quaternary carbonate deposits. Sedimentary Geology 337, 29-35.

Brand, U., Veizer, J., 1980. Chemical diagenesis of multicomponent carbonate systems-1: Trace elements[1]. Journal of Sedimentary Petrology 50, 1219-1236.

Burns, S.J., Haudenschild, U., Matter, A., 1994. The strontium isotopic composition of carbonates from the late Precambrian (~ 560-540 Ma) Huqf Group of Oman. Chemical Geology 111, 269-282.

Calver, C., Baillie, P., 1990. Early diagenetic concretions associated with intrastratal shrinkage cracks in an Upper Proterozoic dolomite, Tasmania, Australia. Journal of Sedimentary Petrology 60, 293-305.

Canfield, D.E., Poulton, S.W., Narbonne, G.M., 2007. Late-Neoproterozoic deep-ocean oxygenation and the rise of animal life. Science 315, 92-95.

Cantine, M.D., Knoll, A.H., Bergmann, K.D., 2019. Carbonates before skeletons: A database approach. Earth-Science Reviews 201, 103065.

Cashman, K.V., Marsh, B.D., 1988. Crystal size distribution (CSD) in rocks and the kinetics and dynamics of crystallization II: Makaopuhi lava lake. Contributions to Mineralogy and Petrology 99, 292-305.

Cody, R., Cody, A., 1988. Gypsum nucleation and crystal morphology in analog saline terrestrial environments. Journal of Sedimentary Research 58, 247-255.

Cowan, C.A., James, N.P., 1992. Diastasis cracks: mechanically generated synaeresis-like cracks in Upper Cambrian shallow water oolite and ribbon carbonates. Sedimentology 39, 1101-1118.

Crawford, J., Goodman, E., Kah, L., 2006. Origin of Precambrian molar-tooth microspar: A new look at an old problem. Geological Society of America Abstracts with Programs 38, 24.

Daly, R.A., 1912. Memoir 38, Geology of the North American Cordillera at the forty-ninth parallel. Department of Mines Geological Survey of Canada, Ottawa.

Demicco, R.V., Hardie, L.A., 1994. An Inventory of Common Sedimentary Structures and Early Diagenetic Features of Shallow Marine Carbonate Deposits. SEPM, Tulsa, Oklahoma.

Du, Y., Han, X., Gu, S., Lin, W., Zhang, C., 2001. Earthquake event deposits in Mesoproterozoic Kunyang Group in Central Yunnan Province and its geological implications. Science in China (Series D) 31, 283-289.

Dupraz, C., Reid, R.P., Braissant, O., Decho, A.W., Norman, R.S., Visscher, P.T., 2009. Processes of carbonate precipitation in modern microbial mats. Earth-Science Reviews 96, 141-162.

Eberl, D., Drits, V., Srodon, J., 1998. Deducing growth mechanisms for minerals from the shapes of crystal size distributions. American Journal of Science 298, 499-533.

Eberl, D., Kile, D., 2005. Crystal growth rate law identified from changes in variance of crystal size distributions. Geochimica et Cosmochimica Acta Supplement 69, A402.

Eby, D., 1975. Carbonate sedimentation under elevated salinities and implications for the origin of “molar-tooth” structure in the Middle Belt Carbonate interval (late Precambrian), northwestern Montana. Abstracts with Program 7, 1063.

Fairchild, I.J., 1983. Chemical controls of cathodoluminescence of natural dolomites and calcites: new data and review. Sedimentology 30, 579-583.

Fairchild, I.J., Einsele, G., Song, T., 1997. Possible seismic origin of molar tooth structures in Neoproterozoic carbonate ramp deposits, north China. Sedimentology 44, 611-636.

Fairchild, I.J., Spencer, A.M., Ali, D.O., Anderson, R.P., Anderton, R., Boomer, I., Dove, D., Evans, J.D., Hambrey, M.J., Howe, J., 2018. Tonian-Cryogenian boundary sections of Argyll, Scotland. Precambrian Research 319, 37-64.

Fantle, M.S., Barnes, B.D., Lau, K.V., 2020. The role of diagenesis in shaping the geochemistry of the marine carbonate record. Annual Review of Earth and Planetary Sciences 48, 549-583.

Fenton, C.L., Fenton, M.A., 1937. Belt series of the North: Stratigraphy, sedimentation, paleontology. Bulletin of the Geological Society of America 48, 1873-1970.

Frank, T.D., Lyons, T.W., 1998. “Molar-tooth” structures: A geochemical perspective on a Proterozoic enigma. Geology 26, 683-686.
Furniss, G., Rittel, J.F., Winston, D., 1998. Gas bubble and expansion crack origin of "molar-tooth" calcite structures in the Middle Proterozoic Belt Supergroup, Western Montana. Journal of Sedimentary Research 68, 104-114.
Gebauer, D., Cölfen, H., 2011. Prenucleation clusters and non-classical nucleation. Nano Today 6, 564-584.
Gilleaudeau, G., Kah, L., 2010. Molar-tooth crack formation and the Proterozoic marine substrate: Insights from the Belt Supergroup, Montana and the Atar Group, Mauritania. Geological Society of America Abstracts with Programs 42, 137.
Gilleaudeau, G.J., Kah, L.C., 2013. Oceanic molybdenum drawdown by epeiric sea expansion in the Mesoproterozoic. Chemical Geology 356, 21-37.
Gilleaudeau, G.J., Frei, R., Kaufman, A.J., Kah, L.C., Azmy, K., Bartley, J.K., Chernyavskiy, P., Knoll, A.H., 2016. Oxygenation of the mid-Proterozoic atmosphere: clues from chromium isotopes in carbonates. Geochemical Perspectives Letters, 178-187.
Goodman, E.E., Kah, L., 2007. Reassessing formation of Precambrian molar-tooth microspar: constraints from carbonate precipitation experiments. Geological Society of America Abstracts with Programs 39, 420.
Halverson, G., Hurtgen, M., 2007. Ediacaran growth of the marine sulfate reservoir. Earth and Planetary Science Letters 263, 32-44.
Halverson, G.P., Hoffman, P.F., Schrag, D.P., Maloof, A.C., Rice, A.H.N., 2005. Toward a Neoproterozoic composite carbon-isotope record. Geological Society of America Bulletin 117.
Halverson, G.P., Wade, B.P., Hurtgen, M.T., Barovich, K.M., 2010. Neoproterozoic chemostratigraphy. Precambrian Research 182, 337-350.
Higgins, M.D., 2006. Verification of ideal semi-logarithmic, lognormal or fractal crystal size distributions from 2D datasets. Journal of Volcanology and Geothermal Research 154, 8-16.
Higgins, M.D., 2011. Textural coarsening in igneous rocks. International Geology Review 53, 354-376.
Hodgskiss, M.S.W., Kunzmann, M., Poirier, A., Halverson, G.P., 2018. The role of microbial iron reduction in the formation of Proterozoic molar tooth structures. Earth and Planetary Science Letters 482, 1-11.
Hofmann, H., 1985. The mid-Proterozoic Little Dal macrobiota, Mackenzie Mountains north-west Canada. Palaeontology 28, 331-354.
Horodyski, R.J., 1976. Stromatolites of the upper Siyeh limestone (Middle Proterozoic), Belt Supergroup, Glacier National Park, Montana. Precambrian Research 3, 517-536.
James, N.P., Narbonne, G.M., Sherman, A.G., 1998. Molar-tooth carbonate: Shallow subtidal facies of the Mid- to Late Proterozoic. Journal of Sedimentary Research 68, 716-722.
James, R.H., Bousquet, P., Bussmann, I., Haeckel, M., Kipfer, R., Leifer, I., Niemann, H., Ostrovsky, I., Piskozub, J., Rehder, G., Treude, T., Vielstädte, L., Greinert, J., 2016.

Effects of climate change on methane emissions from seafloor sediments in the Arctic Ocean: A review. Limnology and Oceanography 61, S283-S299.
Jia, Z.H., Hong, T.Q., Zheng, W.W., Li, S.Y., 2003. The characters and environments of the seismites of the Neoproterozoic Wangshan Formation in North Anhui. Journal of Stratigraphy 27, 146-149, 158.
Jia, Z.H., Ning, X.F., Hong, T.Q., Zheng, W.W., 2011. The Neoproterozoic molar-tooth carbonate rock veins in northern Anhui and Jiangso Provinces and their forming mechanism. Journal of Paleogeography 13, 627-634.
Kah, L.C., Crawford, D.C., Bartley, J.K., Kozlov, V.I., Sergeeva, N.D., Puchkov, V.N., 2007. C- and Sr-isotope chemostratigraphy as a tool for verifying age of riphean deposits in the Kama-Belaya Aulacogen, the East European Plarform. Stratigraphy and Geological Correlation 15, 15-34.
Kah, L.C., Bartley, J.K., Teal, D.A., 2012. Chemostratigraphy of the Late Mesoproterozoic Atar Group, Taoudeni Basin, Mauritania: Muted isotopic variability, facies correlation, and global isotopic trends. Precambrian Research 200-203, 82-103.
Kah, L.C., Bartley, J.K., 2021. Carbonate fabric diversity and environmental heterogeneity in the late Mesoproterozoic Era. Geological Magazine, 1-27.
Kaufman, A.J., Knoll, A.H., 1995. Neoproterozoic variations in the C-isotopic composition of seawater: stratigraphic and biogeochemical implications. Precambrian Research 73, 27-49.
Kellerhals, R., Shaw, J., Arora, V.K., 1975. On grain size from thin sections. The Journal of Geology 83, 79-96.
Kile, D.E., Eberl, D.D., Hoch, A.R., Reddy, M.M., 2000. An assessment of calcite crystal growth mechanisms based on crystal size distributions. Geochimica et Cosmochimica Acta 64, 2937-2950.
Kile, D.E., Eberl, D.D., 2003. On the origin of size-dependent and size-independent crystal growth: Influence of advection and diffusion. American Mineralogist 88, 1514-1521.
Knoll, A., Swett, K., 1990. Carbonate deposition during the late Proterozoic Era: an example from Spitsbergen. American Journal of Science 290, 104-132.
Kriscautzky, A., Kah, L.C., Bartley, J.K., 2022. Molar-Tooth Structure as a Window into the Deposition and Diagenesis of Precambrian Carbonate. Annual Review of Earth and Planetary Sciences 50, 205-230.
Kuang, H.-W., 2014. Review of molar tooth structure research. Journal of Paleogeography 3, 359-383.
Kuznetsov, V., 2003. The "molar tooth" structure and its relation to bios evolution. Doklady Earth Sciences 392, 947-950.
Li, Y.-L., Vali, H., Sears, S.K., Yang, J., Deng, B., Zhang, C.L., 2004. Iron reduction and alteration of nontronite NAu-2 by a sulfate-reducing bacterium. Geochimica et Cosmochimica Acta 68, 3251-3260.
Lifshitz, I.M., Slyozov, V.V., 1961. The kinetics of precipitation from supersaturated solid solutions. Journal of physics and chemistry of solids 19, 35-50.
Lloyd, G.E., 1987. Atomic number and crystallographic contrast images with the SEM: a review of backscattered electron techniques. Mineralogical Magazine 51, 3-19.

Long, D.G.F., 2007. Tomographic study of Paleoproterozoic carbonates as key to understanding the formation of molar-tooth structure. Gondwana Research 12, 566-570.

Lyons, T.W., Anbar, A.D., Severmann, S., Scott, C., Gill, B.C., 2009. Tracking euxinia in the ancient ocean: a multiproxy perspective and Proterozoic case study. Annual Review of Earth and Planetary Sciences 37, 507-534.

Machel, H.G., 1985. Cathodoluminescence in Calcite and Dolomite and Its Chemical Interpretation. Geoscience Canada 12, 139-147.

Machel, H.G., Burton, E.A., 1991. Factors governing cathodoluminescence in calcite and dolomite, and their implications for studies of carbonate diagenesis, In: Barker, C.E., Koppp, O.C. (Eds.), Luminescence Microscopy and Spectroscopy: Qualitative and Quantitative Applications. SEPM Short Course 25, pp. 9-25.

Machel, H.G., Mason, R.A., Mariano, A.N., Mucci, A., 1991. Causes and emission of luminescence in calcite and dolomite, In: Barker, C.E., Koppp, O.C. (Eds.), Luminescence Microscopy and Spectroscopy: Qualitative and Quantitative Applications. SEPM Short Course 25, pp. 9-25.

Marsh, B.D., 1988. Crystal size distribution (CSD) in rocks and the kinetics and dynamics of crystallization. Contributions to Mineralogy and Petrology 99, 277-291.

Marsh, B.D., 1998. On the interpretation of crystal size distributions in magmatic systems. Journal of Petrology 39, 553-599.

Marshall, D., Anglin, C., 2004. CO_2-clathrate destabilization: a new model of formation for molar tooth structures. Precambrian Research 129, 325-341.

McMahon, S., van Smeerdijk Hood, A., McIlroy, D., 2016. The origin and occurrence of subaqueous sedimentary cracks, In: Brasier, A.T., McIlroy, D., McLoughlin, N. (Eds.), Earth System Evolution and Early Life: a Celebrtion of the Work of Martin Brasier. Geological Society of London, Special Publication 448, London 448, pp. 285-309.

Medlin, W., 1968. The nature of traps and emission centers in thermoluminescent rock materials, In: McDougal, W. (Ed.), Thermoluminescence of geological materials. Academic Press, New York, pp. 193-223.

Mei, M., Tucker, M.E., 2011. Molar tooth structure: a contribution from the Mesoproterozoic Gaoyuzhuang Formation, Tianjin City, North China. Acta Geologica Sinica-English Edition 85, 1084-1099.

Michel, F.M., MacDonald, J., Feng, J., Phillips, B.L., Ehm, L., Tarabrella, C., Parise, J.B., Reeder, R.J., 2008. Structural characteristics of synthetic amorphous calcium carbonate. Chemistry of Materials 20, 4720-4728.

Miller, K., Simpson, E.L., Sherrod, L., Wizevich, M.C., Malenda, M., Morgano, K., Richardson, A., Livingston, K., Bogner, E., 2018. Gas bubble cavities in deltaic muds, Lake Powell delta, Glen Canyon National Recreation Area, Hite, Utah. Marine and Petroleum Geology 92, 904-912.

Morse, J.W., Mackenzie, F.T., 1990. Geochemistry of Sedimentary Carbonates. Elsevier, Amsterdam, The Netherlands.

Moussine-Pouchkine, A., Bertrand-Sarfati, J., 1997. Tectonosedimentary subdivisions in the Neoproterozoic to Early Cambrian cover of the Taoudenni Basin (Algeria-Mauritania-Mali). Journal of African Earth Sciences 24, 425-443.

Nealson, K.H., 1997. Sediment bacteria: who's there, what are they doing, and what's new? Annual Review of Earth and Planetary Sciences 25, 403-434.

O'Connor, M.P., 1972. Classification and environmental interpretation of the cryptalgal organosedimentary "molar-tooth" structure from the late Precambrian Belt-Purcell Supergroup. Journal of Geology 80, 592-610.

Orgel, L., 1955. Phosphorescence of solids containing the manganous or ferric ions. The Journal of Chemical Physics 23, 1958-1958.

Petrov, P.Y., 2011. Molar tooth structures: Formations and specificity of carbonate diagenesis in the Late Precambrian, Middle Riphean Sukhaya Tunguska Formation of the Turukhansk Uplift, Siberia. Stratigraphy and Geological Correlation 19, 247-267.

Pierson, B.J., 1981. The control of cathodoluminescence in dolomite by iron and manganese. Sedimentology 28, 601-610.

Pollock, M.D., Kah, L.C., Bartley, J.K., 2006. Morphology of Molar-Tooth Structures in Precambrian Carbonates: Influence of Substrate Rheology and Implications for Genesis. Journal of Sedimentary Research 76, 310-323.

Pope, M.C., Bartley, J.K., Knoll, A.H., Petrov, P.Y., 2003. Molar tooth structures in calcareous nodules, early Neoproterozoic Burovaya Formation, Turukhansk region, Siberia. Sedimentary Geology 158, 235-248.

Pouget, E.M., Bomans, P.H., Dey, A., Frederik, P.M., de With, G., Sommerdijk, N.A., 2010. The development of morphology and structure in hexagonal vaterite. Journal of the American Chemical Society 132, 11560-11565.

Pratt, B.R., 1998. Molar-tooth structure in Proterozoic carbonate rocks: Origin from synsedimentary eartquakes, and implications for the nature and evolution of basins and marine sediment. GSA Bulletin 110, 1028-1045.

Pratt, B.R., 2001. Oceanography, bathymetry and syndepositional tectonics of a Precambrian intracratonic basin: integrating sediments, storms, earthquakes and tsunamis in the Belt Supergroup (Helena Formation, ca. 1.45 Ga), western North America. Sedimentary Geology, 371-394.

Pratt, B.R., 2002. Storms versus tsunamis: Dynamic interplay of sedimentary, diagenetic, and tectonic processes in the Cambrian of Montana. Geology 30, 423-426.

Pratt, B.R., 2011. Molar-tooth structure, In: Reitner, J., Thiel, V. (Eds.), Encyclopedia of Geobiology. Springer, University of Göttingen, Germany, pp. 662-666.

Qiao, X., Song, T., Gao, L.Z., Peng, Y., Li, H., Gao, M., Song, B., Zhang, Q., 1994. Seismic Sequence in Carbonate Rocks By Vibrational Liquefaction. Acta Geologica Sinica-English Edition 7, 243-265.

Rannou, E., Caroff, M., 2010. Crystal size distribution in magmatic rocks: Proposition of a synthetic theoretical model. Journal of Petrology 51, 1087-1098.

Reinhard, C.T., Planavsky, N.J., Robbins, L.J., Partin, C.A., Gill, B.C., Lalonde, S.V., Bekker, A., Konhauser, K.O., Lyons, T.W., 2013. Proterozoic ocean redox and

biogeochemical stasis. Proceedings of the National Academy of Sciences 110, 5357-5362.
Rezak, R., 1957. Stromatolites of the Belt series in Glacier National Park and vicinity, Montana. USGS Professional Paper 294(D), 127-154.
Rodriguez-Blanco, J., Shaw, S., Bots, P., Roncal-Herrero, T., Benning, L.G., 2012. The role of pH and Mg on the stability and crystallization of amorphous calcium carbonate. Journal of Alloys and Compounds 536, S477-S479.
Roest-Ellis, S., Strauss, J.V., Tosca, N.J., 2020. Experimental constraints on nonskeletal $CaCO_3$ precipitation from Proterozoic seawater. Geology 49, 561-565.
Santschi, P., Höhener, P., Benoit, G., Buchholtz-ten Brink, M., 1990. Chemical processes at the sediment-water interface. Marine Chemistry 30, 269-315.
Savard, M.M., Veizer, J., Hinton, R., 1995. Cathodoluminescence at low Fe and Mn concentrations: A SIMS study of zones in natural calcites. Journal of Sedimentary Research A65, 208-213.
Schneider, C.A., Rasband, W.S., Eliceiri, K.W., 2012. NIH Image to ImageJ: 25 years of image analysis. Nature methods 9, 671-675.
Scoffin, T., 1987. An Introduction to Carbonate Sediments and Rocks. Blackie, Chapman and Hall, New York.
Shen, B., Dong, L., Xiao, S., Lang, X., Huang, K., Peng, Y., Zhou, C., Ke, S., Liu, P., 2016. Molar tooth carbonates and benthic methane fluxes in Proterozoic oceans. Nature communications 7, 1-6.
Shen, Q., Wei, H., Zhou, Y., Huang, Y., Yang, H., Wang, D., Xu, D., 2006. Properties of amorphous calcium carbonate and the template action of vaterite spheres. The Journal of Physical Chemistry B 110, 2994-3000.
Shields, G.A., 2002. 'Molar-tooth microspar': a chemical explanation for its disappearance ~ 750 Ma. Terra Nova 14, 108-113.
Smith, A., 2016. A review of molar-tooth structures with some speculations on their origin, In: MacLean, J.S., Sears, J.W. (Eds.), Belt Basin: Window to Mesoproterozoic Earth. Geological Society of America Special Paper 522, pp. 71-99.
Smith, G.A., 1968. The Origin and Deformation of Some "Molar-Tooth" Structures in the Precambrian Belt-Purcell Supergroup. Journal of Geology 76, 426-443.
Sommer, S.E., 1972. Cathodoluminescence of carbonates, 1. Characterization of cathodoluminescence from carbonate solid solutions. Chemical Geology 9, 257-273.
Špillar, V., Dolejš, D., 2014. Kinetic model of nucleation and growth in silicate melts: Implications for igneous textures and their quantitative description. Geochimica et Cosmochimica Acta 131, 164-183.
Stagner, A.F., Bartley, J.K., Kah, L.C., 2004. Variation in deformation style of molar-tooth structure during fluidization: Tawaz Formation, Atar Group, Mauritania. Geological Society of America Abstracts with Programs 36, 88.
Strauss, J.V., Tosca, N.J., 2020. Mineralogical constraints on Neoproterozoic pCO_2 and marine carbonate chemistry. Geology 48, 599-603.
Tan, C., Lu, Y., Li, X., Song, H., Lv, D., Ma, X., Fan, R., Deng, S., 2021. Carbon, oxygen and strontium isotopes of the Mesoproterozoic Jixian System (1.6-1.4 Ga in the

southern margin of the North China Craton and the geological implications. International Geology Review 63, 1951-1968.
Tosca, N.J., Macdonald, F.A., Strauss, J.V., Johnston, D.T., Knoll, A.H., 2011. Sedimentary talc in Neoproterozoic carbonate successions. Earth and Planetary Science Letters 306, 11-22.
Vacassy, R., Lemaitre, J., Hofmann, H., Gerlings, J., 2000. Calcium carbonate precipitation using new segmented flow tubular reactor. AIChE Journal 46, 1241-1252.
Veizer, J., 1989. Strontium isotopes in seawater through time. Annual Review of Earth and Planetary Sciences 17, 141.
Visscher, P.T., Stolz, J.F., 2005. Microbial mats as bioreactors: populations, processes, and products. Palaeogeography, Palaeoclimatology, Palaeoecology 219, 87-100.
Voorhees, P.W., 1992. Ostwald ripening of two-phase mixtures. Annual Review of Materials Science 22, 197-215.
Vorhies, J.S., Gaines, R.R., 2009. Microbial dissolution of clay minerals as a source of iron and silica in marine sediments. Nature Geoscience 2, 221-225.
Wagner, C., 1961. Theorie der alterung von niederschlägen durch umlösen (Ostwald-reifung). Zeitschrift für Elektrochemie, Berichte der Bunsengesellschaft für physikalische Chemie 65, 581-591.
Warren, J.K., Kendall, C.G.S.C., 1985. Comparison of sequences formed in marine sabkha (subaerial) and salina (subaqueous) settings—modern and ancient. AAPG Bulletin 69, 1013-1023.
Wilkin, R.T., 1995. Size distribution in sediments, synthesis, and formation mechanism of framboidal pyrite, The Pennsylvania State University.
Winston, D., Rittel, J.F., Furniss, G., 1999. Gas bubble and expansion crack origin of molar-tooth calcite structures in the Middle Proterozoic Belt Supergroup, western Montana-reply. Journal of Sedimentary Research 69, 1140-1145.
Wu, H., Wang, G., Ding, X., Wang, H., 2020. Geochemistry of the Neoproterozoic molar tooth carbonate in the Benxi Area, North China Craton: The paleo-ocean environment. Journal of Coastal Research 115, 446-450.
Young, G., Jefferson, C., 1975. Late Precambrian shallow water deposits, Banks and Victoria Islands, Arctic Archipelago. Canadian Journal of Earth Sciences 12, 1734-1748.
Young, G., Long, D., 1977. Carbonate sedimentation in a late Precambrian shelf sea, Victoria island, Canadian Arctic Archipelago. Journal of Sedimentary Research 47, 943-955.
Zhou, Y., Pogge von Strandmann, P.A.E., Zhu, M., Ling, H., Manning, C., Li, D., He, T., Shields, G.A., 2020. Reconstructing Tonian seawater $^{87}Sr/^{86}Sr$ using calcite microspar. Geology 48, 462-467.

CHAPTER III

EVIDENCE OF THE ROLE OF SUBSTRATE RHEOLOGY AND LOCAL CARBONATE SATURATION ON THE FORMATION OF CARBONATE MOLAR-TOOTH STRUCTURE

ABSTRACT

Molar-tooth structure (MTS) is an enigmatic carbonate fabric restricted to the Precambrian. In the field, it is characterized by a wide variety of morphologies, ranging from blebs, to elongated ribbons filled with calcite microspar. These features occur most commonly within shallow marine carbonate environments where a semi-rigid, yet not fully lithified, substrate constrains the behavior of gasses produced in the substrate by microbially metabolisms. In this study we investigate the origin of an unusual, 'circular' morphology of MTS from the upper Zhangqu Formation, Qingyunshan National Geopark, China. Detailed field observations show that a critical aspect to the formation of these unusual MTS morphologies is their formation in association with early diagenetic carbonate concretions. Similar structures have been described previously in the Neoproterozoic Burovaya Formation, Russia, where these concretions have been considered responsible for aiding in the precipitation of carbonate within MTS, allowing their preservation. We observe that within the upper Zhangqu Formation, the formation of MT cracks occurs primarily within concretions, and conclude that crack orientation was governed by the difference in substrate strength inside and outside of the concretion. These observations, when combined with the difference in associated facies between the MTS in the lower and upper Zhangqu Formation that indicate an upward-deepening environment, suggest that the formation of concretions resulted in a critical change in the rheology of the deeper-water substrate that favored the formation of MTS.

INTRODUCTION

Molar-Tooth Structure

Molar-tooth structure (MTS) is an enigmatic carbonate texture composed of a complex network of variously shaped cracks and voids filled with calcite microspar, and generally hosted within an argillaceous carbonate rock (Ross, 1959; Rezak, 1957; Fenton and Fenton, 1937; Daly, 1912; Bauerman, 1885). In the field, MTS is characterized by a wide range of void morphologies (Pollock et al., 2006; Pope et al., 2003; Furniss et al., 1998; Horodyski, 1976; O'Connor, 1972) that occur within a variety of sediment lithologies including fine-grained, clayey to silty, mechanically or microbially laminated carbonates (Hodgskiss et al., 2018; Furniss et al., 1998), and less often in fine-grained siliciclastic lithologies (Stewart and Mauk, 2017; Pratt, 2011; Gilleaudeau and Kah, 2010; Bishop and Sumner, 2006; Bishop et al., 2006; Pratt, 1998). MTS is recognizable in the field by visible surfaces showing differential weathering of the recessive crack-filling molar-tooth (MT) microspar relative to the buffed-colored and often dolomitic host rock (Pollock et al., 2006). Void morphologies, when abundant in sedimentary successions, commonly record distinct morphologies with facies. These distinct morphologies can be traced through individual successive depositional cycles and laterally for long distances within the same

facies (Frank and Lyons, 1998; James et al., 1998; Fairchild et al., 1997; Winston, 1986; O'Connor, 1972).

Void morphologies range from spheroidal blebs (Pollock et al., 2006; Frank and Lyons, 1998; Furniss et al., 1998; Ross, 1959), to sheet-like ribbons (Kuang et al., 2009; Meng and Ge, 2002; James et al., 1998; Smith, 1968; cf. Figure 3.1). Blebs typically range from 1 mm to about 5 mm in diameter, with some exceptional samples where blebs have been reported up to 15 mm in diameter (cf. Table 2 in Kuang, 2014). These features are generally smooth and spheroidal and may have one or more small protrusions; more rarely, they may occur as discrete mm-sized bodies with irregular boundaries (Kuang, 2014). Ribbons typically range from less than 1 mm to up to 2 cm wide, with rare examples of even wider features. Ribbon lengths are variable; most typically extending from a few millimeters to a few centimeters, although these features can extend over 15 cm and often intersect lithologic boundaries. Additionally, MT ribbons can be straight, to ptygmatically folded, to fragmented, (often with *en echelon* breakage; Pratt, 2001, 1998; Fairchild et al., 1997). When observed in multiple dimensions in either outcrop or via X-ray computer tomography (Long, 2007), these various MT morphologies can form complex networks.

Field description of MTS morphologies (cf. Bishop and Sumner 2006; Pratt 2001; James et al., 1998; Kah and Knoll 1996; Calver and Baillie 1990; Horodyski 1976) provide the most fundamental dataset that constraints any hypothesis of MT origin. Despite the complexity of MT morphologies recognized in the field, in regions with abundant MTS the morphologies are often similar within beds of uniform lithology and can be laterally persistent (Fairchild et al., 1997; O'Connor, 1972). In these cases, however, MTS are variable between beds of different lithologies; MTS may shift from vertical to horizontal when they reach cohesive clay- rich layers or microbial mats (Hodgskiss et al., 2018; Kuang, 2014; Bishop and Sumner, 2006; Pollock et al., 2006), may pinch out when reaching silt or fine sand laminae (Pratt, 2011; Pollock et al., 2006), and may abruptly terminate, or become diffuse, at intersections with coarse-grain horizons (Pollock et al., 2006; Pratt, 1998; Fairchild et al., 1997). These observations suggest that the morphology of MTS are, at least in part, controlled by substrate rheology (Pollock et al., 2006).

Hypothesized MTS Formation mechanisms

A wide range of formation mechanisms has been proposed to explain the origin of the voids and cracks that characterize MTS (cf. Hodgskiss et al., 2018; Bishop and Sumner, 2006; Pollock et al., 2006; Marshall and Anglin, 2004; Pratt, 1998; Moussine-Pouchkine and Bertrand-Sarfati, 1997; Demicco and Hardie, 1994; Calver and Baillie, 1990; Eby, 1975). Smith (2016), and more recently Kriscautzky et al. (2022), published thorough reviews of these mechanisms. The most common phenomenon hypothesized for the formation of MTS include sediment shrinkage, stress-induced cracking, and gas expansion and migration.

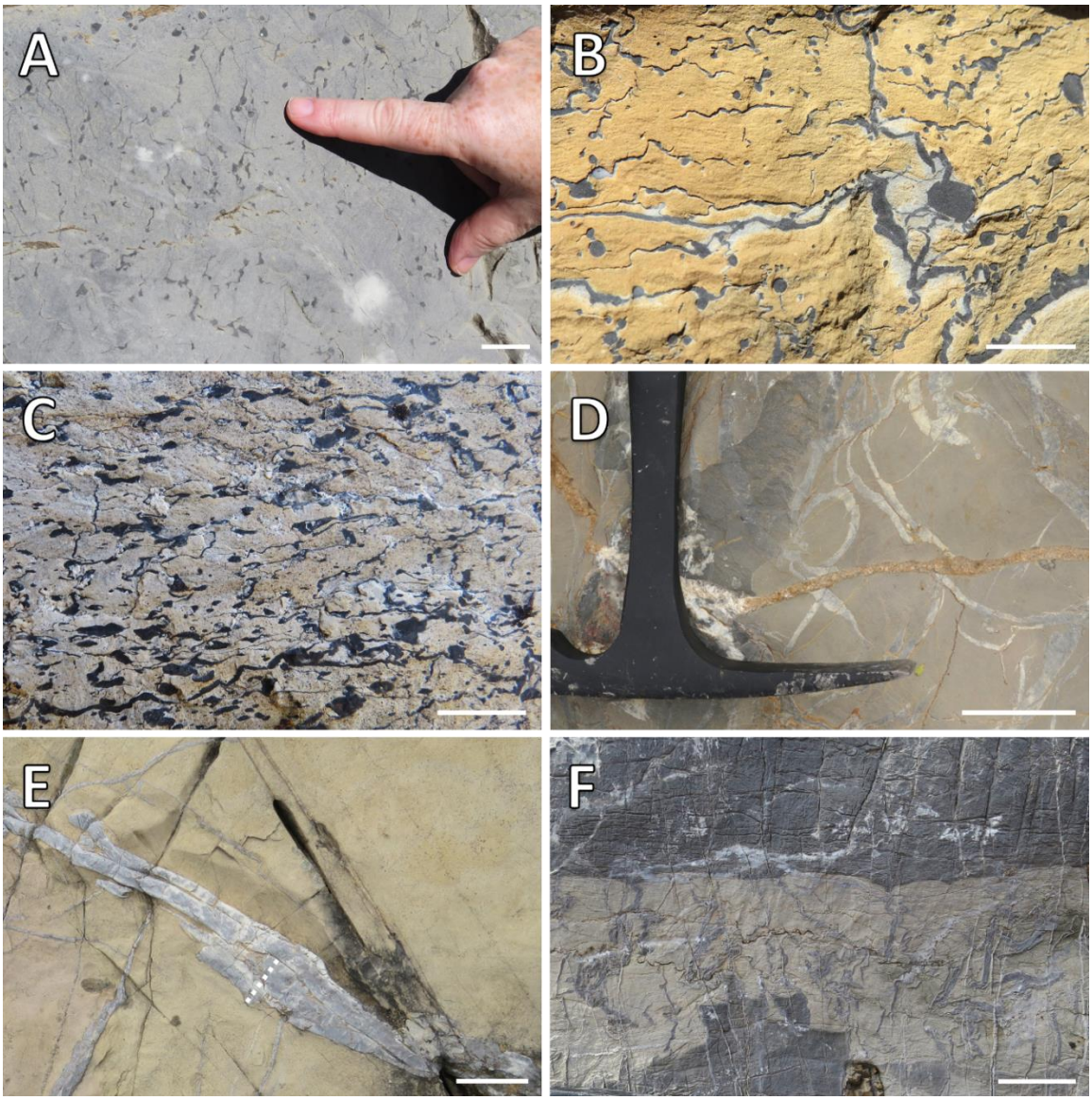


Figure 3.1. Outcrop view of MTS on weathered surface. Blebs and ribbons are MT micrite within a coarser grain dolomitic matrix, often showing a different color due to weathering. A) Isolated blebs with one or two protrusions, Mesoproterozoic Belt Supergroup, US. Scale bar 5 cm. B) Network of blebs and ribbons showing a higher density of features than A. Mesoproterozoic Belt Supergroup, US. Scale bar 1 cm. C) Elongated and interconnected network of ptygmatic MTS. Mesoproterozoic Belt Supergroup. Scale bar 1 cm. D) Curved thick ribbons crosscut by a later vein. Observe how in the fresh surface, both crack and matrix are similar and difficult to recognize. Neoproterozoic, Wangshan Formation, China. Scale bar 5 cm. E) Large size MTS. Dotted line is 2.7 cm long. Neoproterozoic, North Shandong, China. Scale bar is 5 cm. F) MTS going across two sedimentary beds that can be distinguished by their different in weathering colors. Neoproterozoic, Zhangqu Formation, China. Scale bar 5 cm.

Sediment shrinkage mechanisms include those suggested to occur as the result of desiccation (Demicco and Hardie, 1994; Plummer and Gostin, 1981; Horodyski, 1976). Desiccation cracks, however, should be V-shaped in cross section, open upwards toward the sediment-water interface, and be filled with detrital sediment from above. Such characteristics, however, are not found in MTS, which typically pinches out both downward and upward within the substrate and is filled with chemically precipitated carbonate. Such characteristics are more commonly attributed to synaeresis (Petrov, 2011; Calver and Baillie, 1990; Knoll and Swett, 1990; Young and Long, 1977), although synaeresis fails to explain both the relatively common occurrence of MTS in pure carbonate lithologies, and the range of morphologies expressed by MTS (Kriscautzky et al., 2022).

Stress-induced cracking, which arises from the application of physical stressors to the substrate, represents a wide range of hypotheses regarding the origin of MTS. An origin via diastasis (Cowan and James, 1992) forwarded the idea that substrate rheology was important in the formation of MTS and suggests that hydraulic shear on cohesive substrate was the key to forming MT cracks. Diastasis may explain the formation of certain spindle-shaped MTS; however, this idea fails to explain both the formation of the microspar cement as well as the full range of crack morphologies. Hydraulic energy may have been important, however, in cyclic wave loading to enhance fluid flow through crack networks in MTS and aid in the precipitation of MT microspar (Long, 2007; Bishop and Sumner, 2006; Bishop et al., 2006). The motion of fluids within the substrate has also been considered in a suite of hypotheses that consider substrate deformation via hydraulic loading during storms and tsunamis, or seismic shaking (Jia et al., 2011; Kah et al., 2007; Jia et al., 2003; Du et al., 2001; Pratt, 2001, 1998; Bertrand-Sarfati et al., 1997; Fairchild et al., 1997; Moussine-Pouchkine and Bertrand-Sarfati, 1997; Qiao et al., 1994). Most of these models, however, do not provide a mechanism to precipitate the MT microspar, although some propose that microspar migrated from the host rock (Pratt, 2011; Pratt, 1998) or was injected from the surrounding substrate (Qiao et al., 1994). These mechanisms, however, are inconsistent with the unique petrographic signature of MT microspar (Kriscautzky et al., 2022; Kuang, 2014; Pollock et al., 2006) and cannot explain MT within lithologies that lack a components of calcite microspar (Bishop and Sumner, 2006).

The hypothesis for the origin of MTS that is most consistent with the sum of characteristics observed within MTS is that of gas expansion and migration (cf. Kriscautzky et al., 2022; Smith, 2016; Kuang, 2014; Mei and Tucker, 2011; Long, 2007; Pollock et al., 2006; Kuznetsov, 2003; Pope et al., 2003; Furniss et al., 1998). The gas expansion hypothesis attributes the formation of voids to the migration of gasses within a semi-lithified substrate. Substrate gasses would have been produced by metabolic reactions associated with microbial organic matter within the substrate and the accumulation, or expansion, of gas would initially form blebs; gas production that exceeds the strength of the host rock would lead to gas migration and the formation of cracks. The presence of these gasses, or the metabolic reactions from which they form, are hypothesized by some to influence the chemistry of the fluids, potentially triggering MT microspar precipitation

(cf. Bergmann et al., 2013; Higgins et al., 2009; Furniss et al., 1998). Observations in both modern analogs and laboratory simulations support this model by showing a wide range of void morphologies produced by gas expansion and migration (Miller et al., 2018; Boudreau, 2012; Winston et al., 1999; Furniss et al., 1998), as well as the potential to rapidly form MT microspar (Goodman and Kah, 2007; Furniss et al., 1998). Detailed investigation of the shape of MTS and their relationship to the surrounding host rock (Pollock et al., 2006; Pope et al., 2003) then linked the morphology of the blebs and cracks with the rheology of the substrate, proposing MT morphologies would differ among different facies. Although further studies are needed to define the gasses responsible for this process, H_2S is most frequently cited as a possibility, because microbial sulfate reduction is associated with increases in alkalinity that would favor local carbonate precipitation (cf. Bergmann et al., 2013).

Regardless of the mechanism of crack formation, observations indicate that the host substrate was semi-lithified at the time of void formation, and that MT microspar fill precipitated prior to the compaction and lithification of the host material. MT microspar has also independently been shown to have formed penecontemporaneous with the formation of the voids, typically near the sediment-water interface (Kriscautzky et al., 2022), and even occasionally precipitating within the water column (Pollock et al., 2006).

MTS in the geologic record

One of the most striking elements of MTS, however, is that it shows a discrete pattern of occurrence though geologic time. Although MTS has been observed in shallow-marine strata across the world, it is restricted in time to the Precambrian. Furthermore, despite the rare occurrence of MTS from successions as old as ca. 2.6 Ga (McMahon et al., 2016; Bishop and Sumner, 2006; Bishop et al., 2006; Shields, 2002), it is most often recorded in late Mesoproterozoic to early Neoproterozoic strata, between 1.2 and 0.8 Ga (Kriscautzky et al., 2022; Figure 3.2).

Because the preservation of MTS, regardless of the mechanisms of void formation, requires the presence of void-filling microspar, the apparent restriction in time of MTS suggests that the void-filling MT microspar marks an interval in time when geochemical conditions were optimal for its precipitation. These occurrence and behavior of MTS, therefore, may provide key data for better understanding, seawater composition and the early diagenetic processes active within ancient oceans.

This paper focuses on an unusual morphology of MTS from the Qingyunshan National Geopark, Anhui province, China (Kuang, 2014; Liu et al., 2005). Unlike the planar to ptygmatically folded MT ribbons typically observed, MTS in the Neoproterozoic Zhangqu Formation consist of an intricate system of nested rings and septae (Figure 3.3). Here we describe the unusual nature of this MT occurrence, discuss the potential formation mechanisms of these features, and explore how these unusual morphologies may provide key information regarding the changing ocean chemistry of the Neoproterozoic.

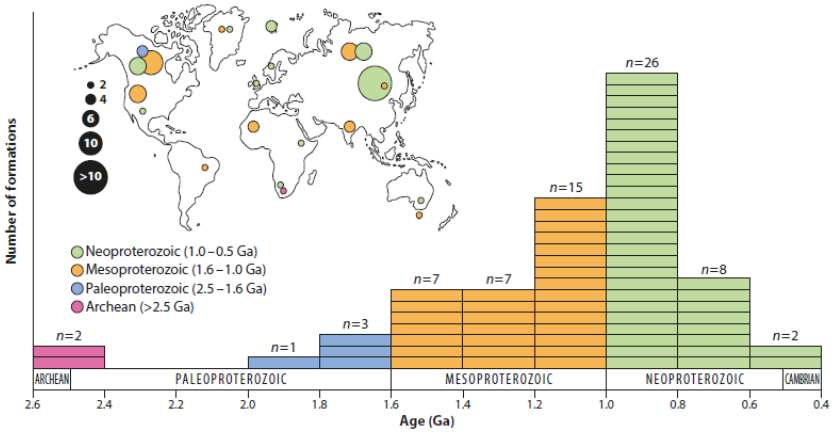


Figure 3.2. Distribution of MTS occurrences in space and time. The map at the top left shows the distribution of MTS occurrences by region. The size of the circles represents the number of formations in which MTS is been recorded. Colors represent age. The histogram in the main panel shows the time distribution of MTS. Bin size is 200 My, and colors are separated by era. From Kriscautzky et al. (2022).

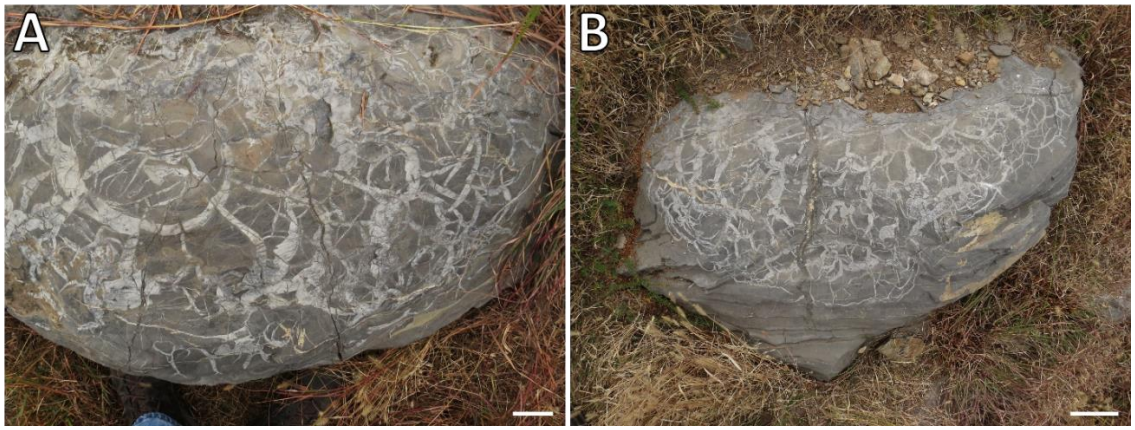


Figure 3.3. Field view of nested rings and septae in MTS from the Zhangqu Formation, China. Scale bars are 10 cm. A) Top view of an interconnected system of MT cracks showing a dense concentration of features within an elliptical body that has been exposed by weathering processes. B) Concentration of MTS within a broadly elliptical body. Host rock layers show clear bending and compaction around the MT-bearing area.

Geology and Age of the Qingyunshan National Geopark

The Qingyunshan National Geopark is located at Northeast of Suzhou, in the Anhui Province (Figure 3.4). Strata exposed within the park include Meso- to Neoproterozoic-aged formations of the Huaihe Group in the Xuhuai Basin (Figure 3.5). Molar-tooth structure are preserved throughout the Zhangqu Formation and the unusual 'circular' MTS are exposed predominantly at the top of the main hill within the geopark.

The Zhangqu Formation is mainly composed of shale, marl, dolomite, and argillaceous limestone and ranges from 294 to 378 m in thickness (Sun et al., 2020; Liu et al., 2005; AHBGMR, 1993). Along with the underlying Niyuan and Jiudingshan formations and the overlying Weiji Formation, the Zhangqu Formation is considered to reflect deposition on a predominantly stable carbonate platform (Ma, 2015; Wang, 2009). The Zhangqu Formation is constrained in age to the early Neoproterozoic, younger than 930 ± 10 Ma (U/Pb SHRIMP; Gao et al., 2009), from a diabase intruding the underlying Niyuan Formation. An early Neoproterozoic age is also consistent with a detrital zircon age of 950 Ma retrieved from clastic rocks of the overlying Shijia Fm. (He et al., 2017).

Detailed stratigraphic measurement marks the base of the Zhangqu Formation by the presence of a one meter-thick intraclastic carbonate, followed by generally thin-bedded mudstone and medium-bedded microcrystalline dolostone (Sun et al., 2020). Liu et al. (2005) divided the formation in intervals that represent initial shoaling from a storm-dominated shelf to peritidal environments, a transgression back to subtidal limestone, and subsequent shoaling to shallow subtidal shelf environments.

MT Occurrences

MTS occur throughout the Zhangqu Formation (Liu et al., 2005), but unusual 'circular' morphologies (cf. Figure 3.3) are exposed primarily near the top of the main hill in the Qingyunshan National Geopark. The stratigraphically lowest section of the Zhangqu Formation exposed in the park of the outcrop exposes a few beds dominated by MTS (Figure 3.6). Here the Zhangqu Formation consists of buff weathered limestone with ~5 cm thick, poorly laminated beds separated by cm-thick intervals of finely laminated limestone, to thicker intervals up to 25 cm MT occurs primarily as predominantly vertical, slightly curvilinear, centimeter-wide cracks that crosscut bedding (Figure 3.6). These wide, spindle-shaped cracks commonly narrow at the intersection with more finely laminated layers, sometimes terminating at the boundary. In other places, extending horizontally and following discrete laminae. Within thinly laminated intervals, MTS becomes more complex, sometimes recording many smaller, randomly oriented spindles. For example, Figure 3.6A shows a series of smaller vertical structures within finely laminated intervals. These secondary structures are often of a smaller size, and they pinch out after a few centimeters. In the lower Zhangqu Formation successive cycles of similar strata are separated by MTS breccias and stromatolites (Figure 3.7). Higher in the section, where beds of unusual 'circular' MTS are exposed, MTS occurs within a similar facies to that

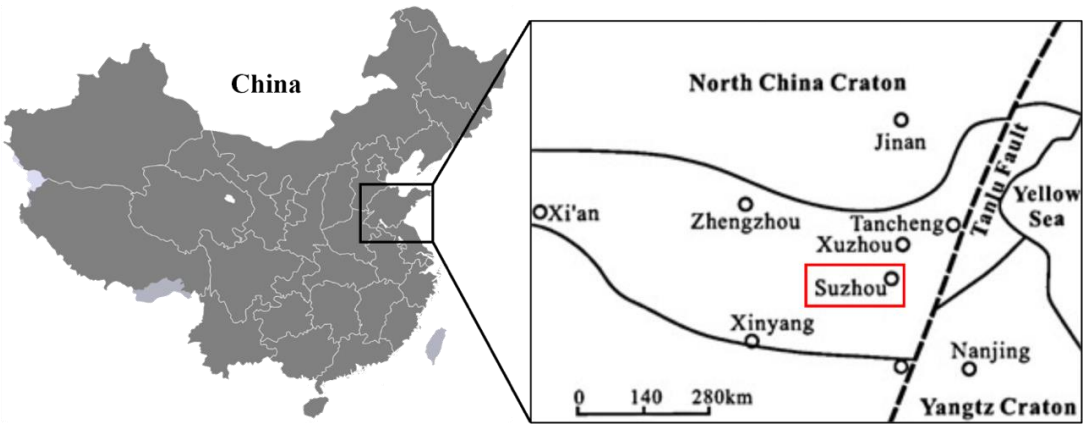


Figure 3.4. Location of the study site. The Qingyunshan National Geopark is located at Northeast of Suzhou, in the Anhui Province, close to the town of Yugou. Strata exposed within the park include Meso- to Neoproterozoic-aged formations of the Huaihe Group in the Xuhuai Basin. Molar-tooth structure are preserved in the Zhangqu Formation and are exposed predominantly at the top of the main hill within the geopark. Close view (right) from Sun et al. (2012).

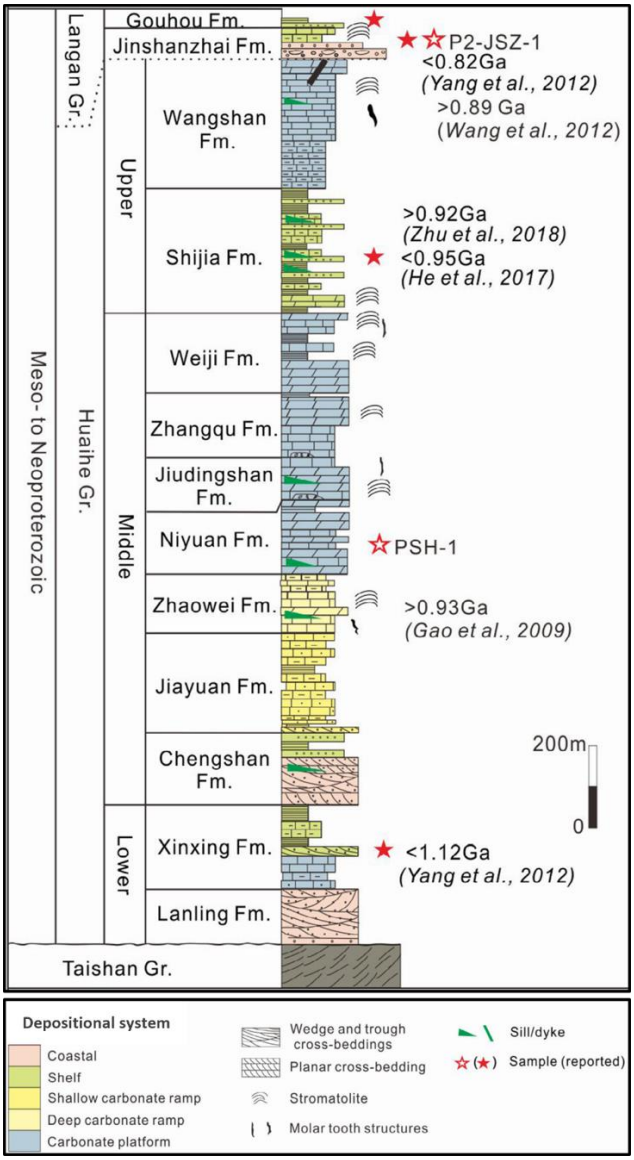


Figure 3.5. Stratigraphic column of the Proterozoic Huaihe Group. The Neoproterozoic Zhangqu Formation is located within a shoaling cycle, including the Niyuan, Jiudingshan, and Weiji Formations. MTS from the Qingyunshan National Geopark belongs to the Zhangqu Formation, which is constrained in age by the underlying Niyuan Formation, dated <930 ± 10 Ma (Gao et al., 2009), and the overlying Shijia Formation dated <950 Ma retrieved from clastic rocks (He et al., 2017). Stratigraphic column from Sun et al. (2020).

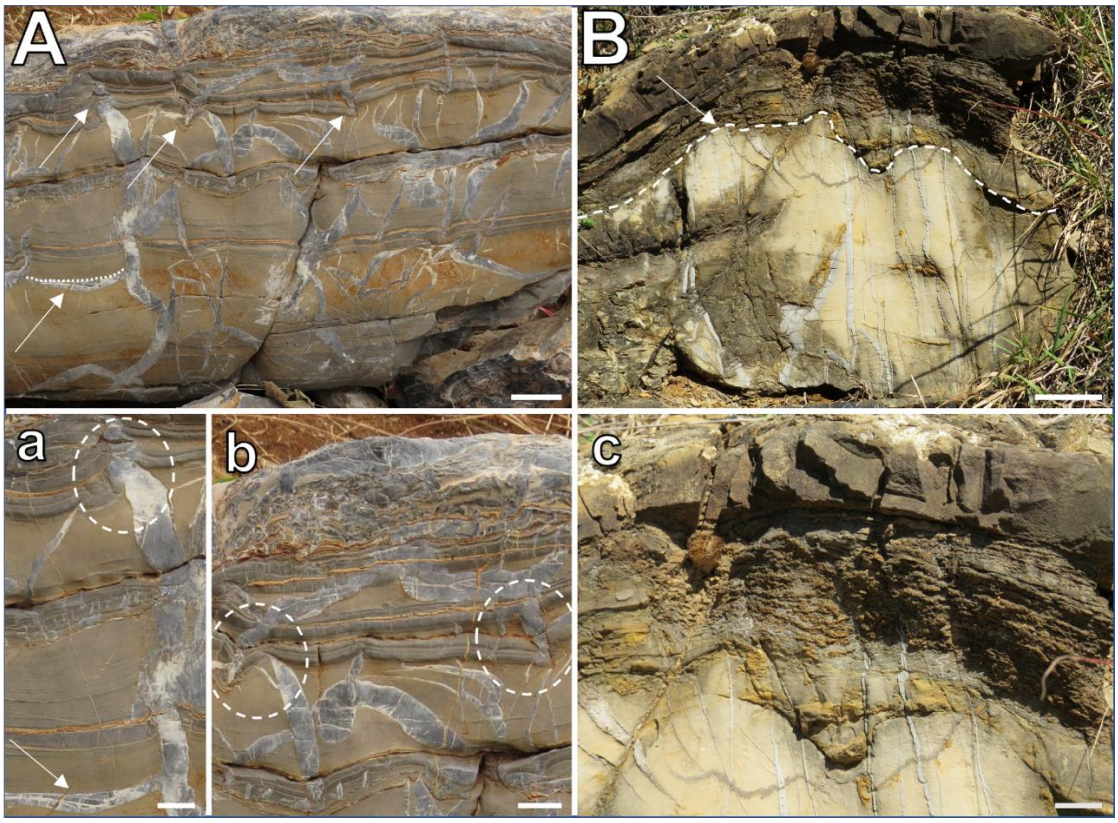


Figure 3.6. Molar-tooth structure from the lowest section of the Zhangqu Formation showing thick, slightly curvilinear, vertical features. A) Up to 1.5 cm wide MTS crossing thinly laminated carbonate intervals, topped by a bed of brecciated MTS. Arrows indicate areas highlighted in **a** and **b**. **a**, MTS protruding upwards, with deformation of overlying carbonate layers (dashed circle), and horizontal MTS following the carbonate layer (arrow). **b**, MTS protruding downward to the underlying carbonate layer (dashed circles). B) Over 25 cm long, vertical MTS penetrating a concretion of fine-grained carbonate and overlying microbially laminated dolomitic interval, terminating abruptly at an overlying sandstone layer. **c**, Closer view of B, showing various behavior of MTS within the well-laminated dolomite, and terminating at the contact with the overlying sandstone. Scale bars are 5 cm (A and B), and 2 cm (a, b, and c).

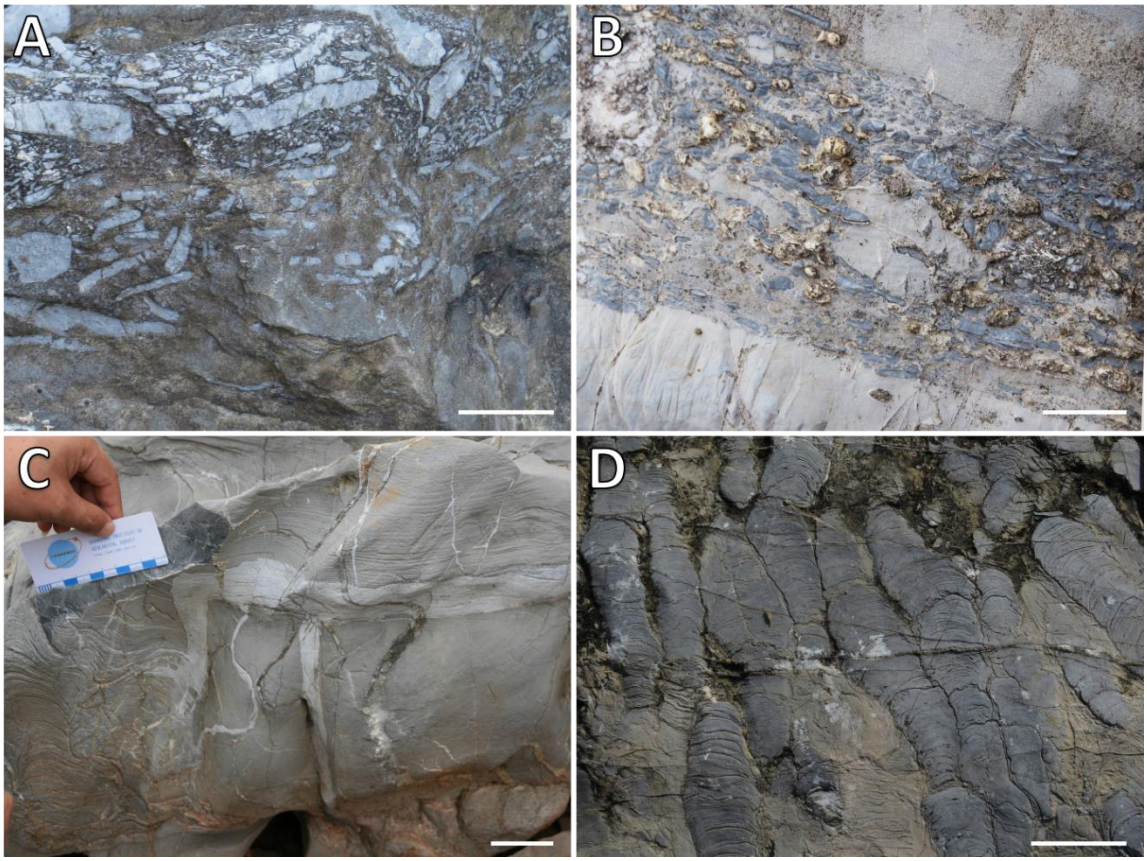


Figure 3.7. Brecciated MTS and stromatolite intervals within the Zhangqu Formation. A and B) Sedimentary breccias composed of broken and redeposited pieces of MT ribbons within a carbonate matrix. Scale bars are 2 cm. C) Stromatolites associated with MTS ribbons that occurring at the edge and within thinly laminated microbial carbonates. D) Columnar stromatolites between MTS-bearing beds in the Zhangqu Formation. Scale bars are 5 cm.

observed lower in the Zhangqu Formation, in which ~5 cm thick beds of massive to vaguely planar laminated limestone are interbedded with 1-3 cm thick beds of well laminated limestone. Here MTs occurs in discrete three-dimensional bodies (Figure 3.3). A key observation is that the density of MTS within these polygonal structures is substantially higher than in the surrounding matrix, and oftentimes MTS is restricted to within these spheroidal bodies. In plan view, MTS appear as polygons formed by the radial segmentation of nested, circular MT rings (Figures 3.3 and 3.8). MT cracks that form these broadly circular features average 1 cm wide. Individual polygons vary in size and shape, tending from circular to almost rectangular in shape; the outer rings range from 10 to 30 cm in diameter while the inner rings range from 2 to 10 cm in diameter, and can be either continuous or discontinuous. In some cases (Figure 3.8), these polygonal to circular features contain a subset of smaller MTS that mimic the structure of the larger features.

Molar-tooth structure are commonly constrained to (or present in higher density within) ellipsoidal bodies (Figure 3.9 and 3.10; cf. Figure 3.3). The sedimentary layers above and below these areas with MTS follow the shape of the ellipsoids. At the edges of the bodies (Figure 3.9), the lithology bends and thins. MT cracks show a distinct change when intersecting this boundary, either stopping or showing an arcuate form that curves inward toward the center of the ellipsoidal body (Figure 3.10). Within the ellipsoidal bodies, the MTS is variable in shape, and show characteristic changes in morphology that appear to be related to the composition of the individual sedimentary layers. Figure 3.10b, for example, shows how MTS developed very thick ribbons within a single layer, occupying a great volume of it. These ribbons extend laterally, but not so vertically toward the underlying or overlying beds. When these cracks reach the edge of the layer, they either push material outwards (bending the laminae) not cutting through, cut through the next layer but they shift direction and pinch out, or simply follows the edge, never going across it. This behavior indicated that MTS may have formed in specific layers due to their rheology and were unable to trespass to others probably more rigid, or less permeable. Figure 3.10c show some areas with some premature enigmatic ring structures.

All these MTS occurrences also contain thin to thick, dark grey to yellow veins that cross-cut both MT-bearing bodies and the surrounding sedimentary packages (cf. Figure 3.10). In some areas, these veins are filled by more than one composition. This observation indicates that brittle deformation occurred at a later state, after all the previous structures formed, as a product of a more rigid behavior. Veins with different mineralogy also indicate various processes of deformation and different fluids involved.

DISCUSSION

Mechanism for the development of concretions

Within the upper Zhangqu Formation, Qingyunshan National Geopark, an unusual morphology of MTS occurs which, in plan view, records an intricate system of nested rings and septae. Notably, in this region, the occurrence of MTS are associated with, and

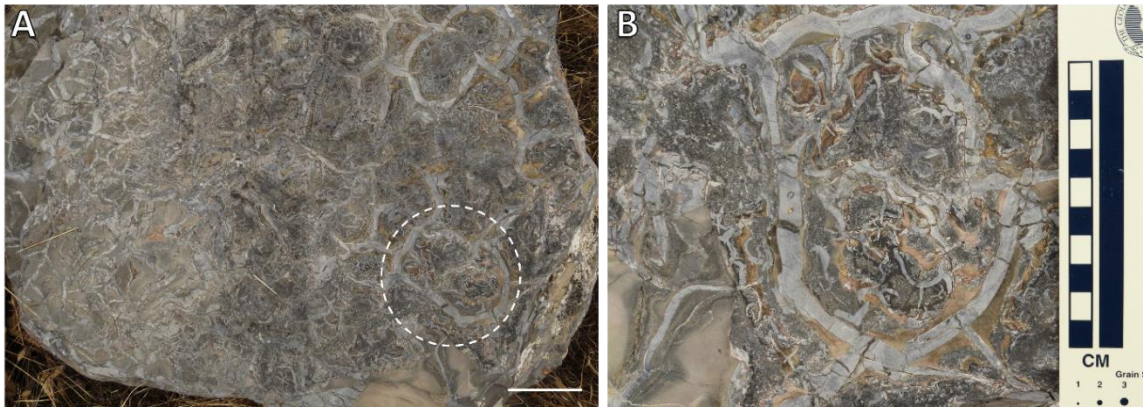


Figure 3.8. Plan view of three-dimensional MT-bearing bodies. MTS appear as polygons formed by the radial segmentation of nested, circular MT rings. Individual polygons vary from circular to almost rectangular in shape; outer rings range from 10 to 30 cm in diameter while the inner rings range from 2 to 10 cm in diameter. Radial MT fractures often appear to join the apices of the polygons. The inner-most area of the rings is often devoid of MTS. A) Plan view of the exposed, weathered surface of a bedding plane showing polygonal MTS. Scale bar is 5 cm. B) Closer view of a single external polygon showing internal septae and smaller-scale MTS within the primary ring.

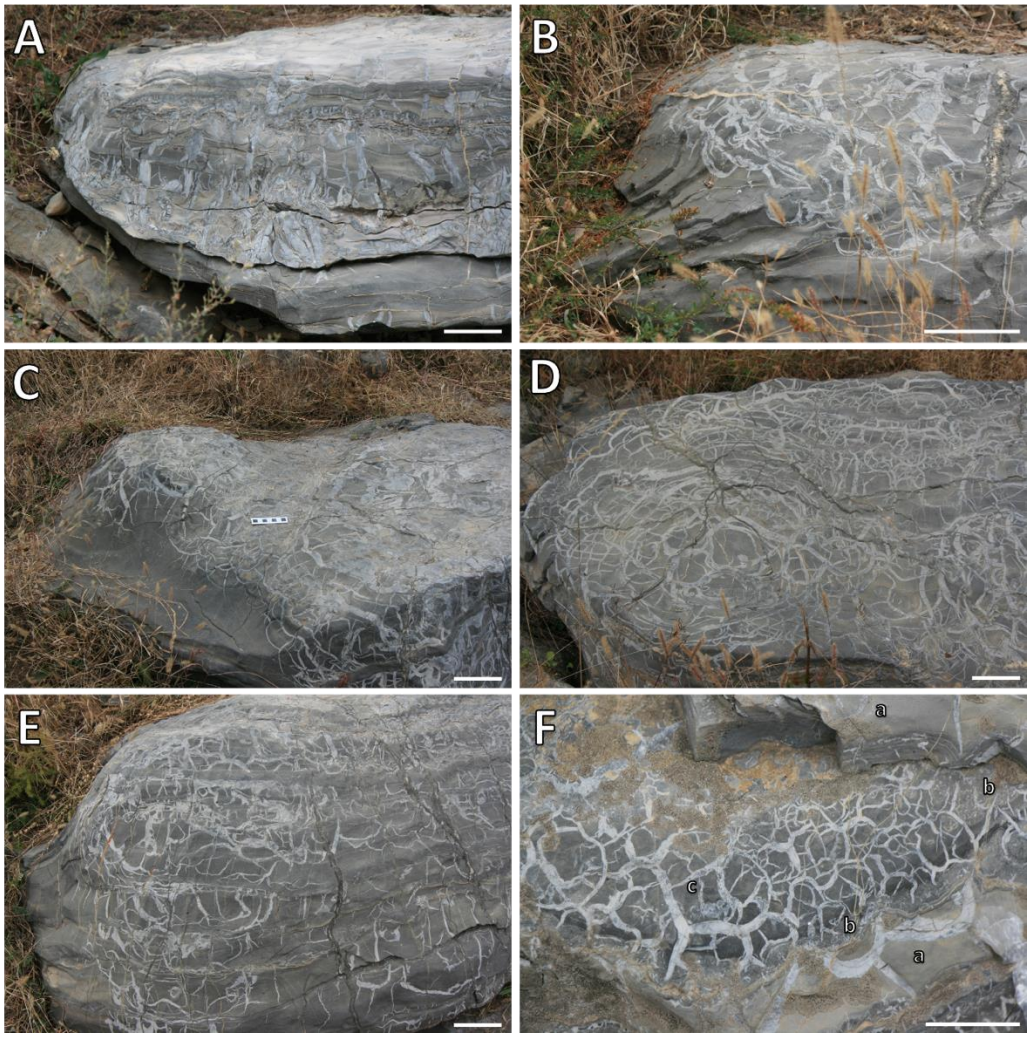


Figure 3.9. Dense accumulation of MTS within ellipsoidal bodies. A) Dominantly vertical MT ribbons that vary in size depending on lamina structure; note that underlying beds curve upward at the edge of the MT-bearing body. B) MTS showing curvature that marks the edge of the MT-bearing body, associated with bending and thinning of host rock lithologies. C) Intersection of two MT-bearing ellipsoidal bodies. D) Intersection of three discrete MT-bearing ellipsoidal bodies, with curvature of MT ribbons following the shape external shape of the MT-bearing body. E) MTS ending abruptly at the edge of the ellipsoidal body, with associated bending and thinning of host rock lithologies. Internally, changing morphology of MTS is strongly associated with distinct beds within the host rock. F) Flatter ellipse detailing the different behavior of MT cracks with lithology: (a) outer layers that bend around the body, with thick short MTS; (b) Medium-grey layer with thin, short MTS constrained to within this layer; and (c) an inner section with nested, polygonal MTS.

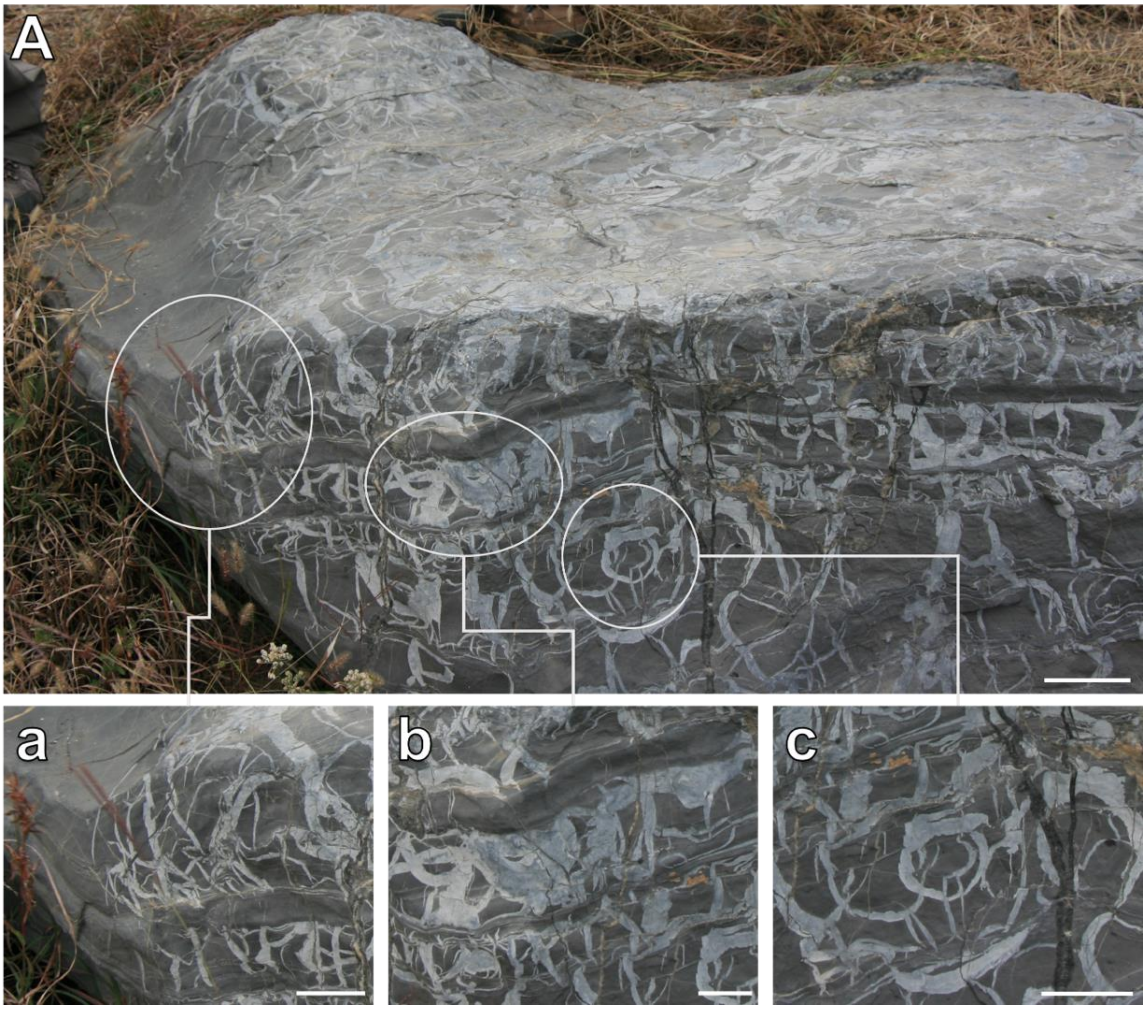


Figure 3.10. Variability of MTS within a single ellipsoidal body. A) Two ellipsoidal bodies joined by a single layer of MTS (cf. Figure 3.9C). A dense network of MTS is confined largely to within the ellipsoidal bodies. (a) Dominantly vertical, arcuate ribbons curve inward, marking the boundary of the ellipsoidal body. (b) Variation in shape and density of MTS is correlated with changes in host rock lithology; arrest, or a change in direction, of MT ribbons at a single layer suggests difference in strength between the layers. (c) Rare region where nested rings occur in cross-section of the ellipsoidal body. Note dark late-stage veins that crosscut bedding planes, MTS, and edges of the hosting body. Scale bars are 10 cm (A), and 5 cm (a, b, and c).

constrained within, decimeter- to meter-scale ellipsoidal bodies. These ellipsoidal bodies are further marked by the thinning and bending of host rock layers at the edge of the bodies. Combined, these features suggest that MTS of the upper Zhangqu Formation occur in association with the formation of concretions. Concretions are spherical to ellipsoidal bodies that occur when a sedimentary rock undergoes differential cementation of the host rock through authigenic material precipitation within the host rock (Sellés-Martínez, 1996). Porosity, permeability, and other physical properties of the substrate are key in the formation and preservation of concretionary bodies and their diagenetic cementation history (Raiswell and Fisher, 2000).

Concretionary structures are perhaps best known for the high-quality preservation of skeletal material and soft tissue (Orr et al., 2000; Martill, 1988), or similarly, the preservation of undeformed sedimentary structures (Savrda and Bottjer, 1988; Maples, 1986). The absence of compaction within concretions (as well as the compaction of host rock laminae at the edges of concretions) suggests that the material within the concretion was preferentially resistant to compaction. It is often assumed that concretions represent fully lithified and rigid bodies: Hudson (1978) described concretions with brecciated centers, and Martill and Hudson (1989) observed clastic dykes that either deflected around or caused brittle fractures within other concretions. Exhumed concretions on the seafloor are also oftentimes broken and then bored as hardgrounds (Fürsich et al., 1992; Hesselbo and Palmer, 1992; Hallam, 1969). Other evidence, however, suggests that concretions were not fully rigid (Hesselbo and Palmer, 1992; Criss et al., 1988; Bjørlykke, 1973). Raiswell and Fisher (2000) concluded that these mechanisms are not inconsistent, since brittle failure requires low degree of rigidity, while plastic behavior depends on strain rate. Therefore, an initial degree of cementation would still behave plastically during shallow burial, yet still be rigid enough to undergo brittle failure and to be preserved under compaction.

The cementation that results in the formation of concretions can be either pore-filling and displacive (Fisher et al., 1998; Huggett, 1994), as well as replacive (Huggett, 1994; Feistner, 1989; Hennessy and Knauth, 1985). In light of these observations, Raiswell and Fisher (2000) proposed a process wherein early cementation can result in semi-lithified regions of host rock that are resistant to compaction, but still porous, and fully cemented only after burial. Such cementation may have occurred either concentrically or pervasively. Concentric growth reflects an initial nucleation point and successive cementation outward from this point. By contrast, pervasive growth starts with the formation of many individual nuclei across the concretionary body, and further precipitation on to these nuclei (Raiswell and Fisher, 2000). Concretions, however, are complex and recognizing a single end-member behavior associated with their formation and cementation may not always be possible; studies often show a complex cementation history (cf. Dickson and Barber, 1976).

Of particular interest here is the formation of fissures (such as MT cracks) within concretions. Septarian fissures are typically carbonate or iron-rich concretions that contain radiating cracks (referred to as septaria) that are commonly filled with late-stage carbonate

cements. These fissures within what are commonly referred to as septarian nodules have an uncertain origin. One suggestion is that early cementation would lower the permeability of the concretion, resulting in pore pressure higher inside the concretion than in the surrounding sediment (Hounslow, 1997). With burial, overpressure of the sediment would then result in deformation by tensile fractures (Astin, 1986). Hesselbo and Palmer (1992), however, found septarian cracks at depths of less than 30 m, and Duck (1995) found septarian cracks in beds that have been buried less than 10 m, suggesting that overburden pressure was unlikely to have driven crack-formation. Others suggest that septarian nodules represent shrinkage or dehydration during shallow burial (Raiswell, 1971). Sellés-Martínez (1996) proposed that septarian cracks could form in the shallow subsurface in semi-lithified concretions when stress is imparted to a plastic sediment by shrinking of gels, or by synaeresis within the fine-grained core of the concretion.

Formation of Zhangqu Formation MT-bearing concretions

When exposed in three-dimensions, unusual 'circular' MTS of the upper Zhangqu Formation records the preferential formation and preservation of MTS within meter-scale concretionary bodies. Similar to septarian nodules, MTS of the upper Zhangqu Formation is represented by a network of arcuate cracks that occur both parallel and perpendicular to the edges of concretions, the edges of which are defined by the bending and thinning of host rock layers. Although some cracks crosscut the boundary between ellipsoidal boundaries (cf. Figure 3.9C), they more commonly show a change in orientation parallel to the edge of the concretion (cf. Figures 3.9 and 3.10). Unlike classic septarian nodules, however, which typically are filled with late-diagenetic cements that show nucleation on the crack edge and competitive growth toward the center, Zhangqu Formation septarian-like concretions are composed of cracks filled with a unique equant microspar that is characteristic of MTS (Kriscautzky et al., 2022).

Here we suggest that concretion formation within the upper Zhangqu resulted from a change in the rheology of the substrate that was favorable for the formation of MTS. MTS occurs primarily in shallow marine environments where a semi-rigid, yet not fully lithified, substrate constrains the behavior of gasses produced in the substrate by microbially metabolisms (Pollock et al., 2006; Frank and Lyons, 1998; Furniss et al., 1998) In this scenario, cracks form only when gas production is sufficient to overcome the strength of the surrounding substrate, forming cracks. These cracks are generally vertical, suggesting primary expansion of crack tip driven by gas migration toward the sediment-water substrate. Depending on stresses produced by gas expansion, however, cracks can also be deflected at the boundary between layers of different strength (see examples in Pollock et al., 2006). Here we suggest that broadly circular pattern recorded by the largest MT cracks reflect changes in strength within the concretion that resulted from concentric growth. In this model, distinctly different physical properties are assumed for inside and outside of the concretions, wherein the sediment outside of the concretions show substantial

compaction, indicating a lack of rigidity that is necessary to form MT cracks. Within concretions, MTS shows a diversity of forms that further suggests that individual beds behaved differently during early lithification, potentially reflecting extent, and connectivity of original pore space.

The hypothesis that concretion formation was a pre-requisite to the formation of MTS is consistent, as well, with other features of the upper Zhangqu Formation. Both stratigraphically below and above the interval characterized by MT-bearing concretions is evidence of seismically-driven substrate deformation and liquefaction (Jia et al., 2011; Jia et al., 2003; Du et al., 2001; Qiao et al., 1994; Figure 3.11). Liquefaction, in particular, suggests that the shallow sediment stack was dominantly unlithified and water-rich. Gas formation within such materials would likely escape during seismically-induced dewatering. Seismic disruption of the substrate, in fact, has been argued as a potential mechanism for the formation of MTS (Kah et al., 2012; Kah et al., 2007; Stagner et al., 2004; Moussine-Pouchkine and Bertrand-Sarfati, 1997). Such models, however, typically ascribe seismic activity to the structural formation of fractures within the substrate. A combination of spheroidal voids and spindle shaped cracks within the Sheepbed mudstone, Gale crater, Mars, are similar to MTS and have been suggested to potentially represent the effects of seismic waves on substrate gasses (Siebach et al., 2014; Stack et al., 2014). In this extraterrestrial scenario, seismic waves emanating from local impacts could induce the exsolution of substrate gas, resulting in void formation. This extraterrestrial scenario differs from traditional models of MT formation because it is not predicated on the active production of gas in the substrate by microbial activity. In a terrestrial realm, however, one can envision that microbial activity in the substrate may have aided in the formation of initial concretionary forms (Raiswell and Fisher, 2000; Coleman and Raiswell, 1995; Coleman and Raiswell, 1993; Raiswell, 1976). Either continued gas production within the semi-lithified concretion, or exsolution of gasses during seismic activity, could then be responsible for crack formation.

Zhangqu Formation MT-bearing concretions are similar to structures described from the Neoproterozoic Burovaya Formation, Northwestern Siberia, Russia (cf. Figures 2-4 in Pope et al., 2003). In these spectacular examples, 1–2-meter diameter spheroidal nodules occur within dark gray dolostone. The host rock is thinly laminated, and laminae are readily traced from the surrounding host rock through the concretions. Abundant MTS occurs within the nodules but is not found in host rock outside of these nodules. In two-dimensions, cracks sometimes show nested polygonal shapes with radiating septae extending from their corners (Figure 3.5 in Pope et al., 2003). In contrast to the hypothesis proposed here that concretion formation was necessary to provide the substrate rigidity necessary for the formation of MT cracks, Pope et al. (2003) suggest that a difference in carbonate saturation within the regions now seen as concretions was responsible for aiding in the precipitation of carbonate locally within MTS, thereby allowing their preservation; cracks within the surrounding substrate are then assumed to have been lost during substrate compaction. We suggest that, in both these formations, the circular to polygonal fractures



Figure 3.11. Examples of beds indicating seismic deformation and liquefaction. A) deformation of beds with loss of most of the initial structure suggesting liquefaction; note centimeter-scale rigid clasts floating within liquified layer (cf. Jia et al., 2011; Jia et al., 2003; Du et al., 2001; Qiao et al., 1994). Scale bar is 20 cm.

that are oriented broadly parallel to and perpendicularly to the edges of concretions demands that crack orientation was governed by the difference in substrate strength inside and outside of the concretions and supports formation of MT cracks only within the concretion. Salinity may have increased either in the shallow lower section by evaporation, or within the concretions by burial processes (Raiswell, 1971), increasing carbonate saturation. Substrate lithification, therefore, is constrained to have occurred prior to crack formation, suggesting that precipitation of the crack-filling microspar represents a discrete episode of carbonate formation. Kriscautzky et al. (2022) suggest that microspar precipitation within MT cracks may have required enhancing the saturation state locally within fractures by the microbial modification of seawater within substrate pore space.

Formation of MTS in time and space

Earlier investigation demonstrates that the preservation of MTS in the geologic record requires a mechanism for formation of cracks within the substrate as well as a mechanism for precipitating microspar within the cracks prior to subsequent compaction of the substrate, and that the ultimate demise of MTS within the geologic record may reflect a fundamental change in the carbonate saturation state of the oceans (cf. Kah and Bartley, 2021; Cantine et al., 2019; Hodgskiss et al., 2018; Pollock et al., 2006) It is perhaps interesting to note that examples where MTS is confined to concretionary bodies occurs in the early Neoproterozoic, near the global demise of MTS (cf. Figure 3.2; see also Jiayuan, Zhaowei, Weiji, and Wangshan Formations, A. Kriscautzky and L.C. Kah, personal observations).

Key observations to this trend may be found in the Zhangqu Formation. Here, MTS occur in a variety of facies that show no evidence of concretions, and instead show interbedding with a variety of stromatolite morphologies and intraclastic breccias. Intraclastic breccias are most common in shallow subtidal lithologies that experience active wave energy that disrupts the substrate. In a recent compilation of facies, Kah and Bartley (2021) suggest that intraclastic breccias are also diagnostic of the late Mesoproterozoic and propose that this interval in time (here presumably extending into the early Neoproterozoic) represents a critical threshold of marine carbonate saturation state that is distinct from more elevated saturation states earlier in the Proterozoic, and lower saturation states in the mid-Neoproterozoic (see also Cantine et al., 2019). Kah and Bartley (2021) propose that this critical threshold of saturation state resulted in shallow marine environments that were sensitive to small changes in local environment. Local environmental changes (cf. freshwater influx, evaporation, microbial activity) could then drive lamina-by-lamina variation in the degree of substrate lithification that was conducive to the formation of intraclasts during storm events. In their detailed analysis of late Mesoproterozoic carbonate facies, Kah and Bartley (2021) found one succession which contained abundant carbonate concretions. These concretions formed in water depths greater than those that produced widespread early lithification (e.g., stromatolites, MTS, and intraclastic breccias),

suggesting that local saturation state was insufficient in these regions to drive the rapid lithification of the substrate. Instead, it was hypothesized that microbial reactions within the shallow substrate were needed to drive carbonate saturation state to a point where carbonate precipitation occurred within the substrate.

The detailed compilation of late Mesoproterozoic carbonate facies provides a framework for better understanding MT-bearing concretions within the early Neoproterozoic. We suggest that the stratigraphically lowermost Zhangqu Formation exposed within the Qingyunshan National Geopark represents generally peritidal deposition where early lithification of the substrate was relatively widespread and marked by stromatolite formation, widespread MTS, and the formation of intraclastic breccias. Stratigraphically higher portions of the Zhangqu formation lack widespread stromatolites (although some still occur locally) and lack widespread MTS and intraclastic breccia. Rather, these strata are marked by evidence for substrate deformation and liquefaction that suggests early cementation was confined to a localized occurrence of MT-bearing concretions. These observations suggest that the upper Zhangqu Formation represents deeper-water deposits and a marine water column whose carbonate saturation state was insufficient to drive substantial carbonate production. In this localized region, active microbial activity within the shallow substrate likely drives the formation of the Zhangqu formations and continued even within a semi-lithified concretions to form the MT voids. In this scenario, the pore-waters within the concretions would likely be in equilibrium with the surrounding carbonate concretion (potentially elevated than the substrate outside the concretion), permitting additional substrate gas to drive the precipitation of MT microspar within the voids. The presence of dark veins that crosscut all of these structures are then hypothesized to have formed during the late diagenetic tectonic uplift of the Neoproterozoic successions in this region (He et al., 2017; Tang et al., 2015; Xiao et al., 2014; Sun et al., 2013, 2012; Sun et al., 2011).

CONCLUSIONS

- Early Neoproterozoic rocks of the Anhui Province contain abundant MTS, largely within rocks interpreted to have formed in stable carbonate platforms.

- The Zhangqu Formation (<930 Ma) in the Qingyunshan National Geopark contains abundance of an unusual morphology of MTS that consists of ‘circular’, nested features. These MTS have a structure much like fractures within septarian nodules; and the majority of them in the upper Zhangqu Formation is restricted to meter-scale concretionary bodies.

- We suggest that the upper Zhangqu Formation represents dominantly subtidal deposition that lacks evidence for early diagenetic cementation of the substrate. Rather cementation within the substrate is confined to concretions that may have been loci of microbial activity. We propose that metabolic reactions related to

microbial activity and decomposition within the substrate continued after initial lithification, wherein microbially produced gasses then formed MT cracks and initiated crack-filling microspar. Future work involving state of the art technology should seek for a methodology to distinguish potential metabolic reactions that occurred within the sediment, and potential gasses released during redox processes that could originate MT cracks.

ACKNOWLEDGEMENTS

I want to thank my advisor, Dr. Linda Kah, and my committee members, Dr. Anna Szynkiewicz, Dr. Molly McCanta, and Dr. Julie Bartley, for their time and commitment to improving this chapter. I would like to thank Dr. Hongwei Kuang and extended it to all our Chinese colleagues for inviting us to do fieldwork in Northeast China.

REFERENCES

AHBGMR, 1993. Regional Geology of Anhui Province [M], Bureau of Geology and Mineral Resources of Anhui Province. Geological Publishing House Beijing (in Chinese), pp. 517-547.

Astin, T., 1986. Septarian crack formation in carbonate concretions from shales and mudstones. Clay Minerals 21, 617-631.

Bauerman, H., 1885. Report on the geology of the country near the forty-ninth parallel of north latitude west of the Rocky Mountains, Report of progress 1882-1884. Geological Survey of Canada, pp. B 1-42.

Bergmann, K.D., Grotzinger, J.P., Fischer, W.W., 2013. Biological influences on seafloor carbonate precipitation. Palaios 28, 99-115.

Bertrand-Sarfati, J., Plaziat, J., MoussinePouchkine, A., 1997. Vermicular structures in the Neoproterozoic of the West African Craton: Microbialites versus 'molar tooth'. Facies 36, 231-234.

Bishop, J.W., Sumner, D.Y., 2006. Molar tooth structures of the Neoarchean Monteville Formation, Transvaal Supergroup, South Africa. I: Constraints on microcrystalline CaCO3 precipitation. Sedimentology 53, 1049-1068.

Bishop, J.W., Sumner, D.Y., Huerta, N.J., 2006. Molar tooth structures of the Neoarchean Monteville Formation, Transvaal Supergroup, South Africa. II: A wave-induced fluid flow model. Sedimentology 53, 1069-1082.

Bjørlykke, K., 1973. Origin of limestone nodules in the Lower Palaeozoic of the Oslo Region. Universitetsforlaget.

Boudreau, B.P., 2012. The physics of bubbles in surficial, soft, cohesive sediments. Marine and Petroleum Geology 38, 1-18.

Calver, C., Baillie, P., 1990. Early diagenetic concretions associated with intrastratal shrinkage cracks in an Upper Proterozoic dolomite, Tasmania, Australia. Journal of Sedimentary Petrology 60, 293-305.

Cantine, M.D., Knoll, A.H., Bergmann, K.D., 2019. Carbonates before skeletons: A database approach. Earth-Science Reviews 201, 103065.

Coleman, M., Raiswell, R., 1993. Microbial mineralization of organic matter: mechanisms of self-organization and inferred rates of precipitation of diagenetic minerals. Philosophical Transactions of the Royal Society of London. Series A: Physical and Engineering Sciences 344, 69-87.

Coleman, M.L., Raiswell, R., 1995. Source of carbonate and origin of zonation in pyritiferous carbonate concretions; evaluation of a dynamic model. American Journal of Science 295, 282-308.

Cowan, C.A., James, N.P., 1992. Diastasis cracks: mechanically generated synaeresis-like cracks in Upper Cambrian shallow water oolite and ribbon carbonates. Sedimentology 39, 1101-1118.

Criss, R., Cooke, G., Day, S., 1988. An organic origin for the carbonate concretions of the Ohio Shale. US Geological Survey Bulletin 1836, 1-21.

Daly, R.A., 1912. Memoir 38, Geology of the North American Cordillera at the forty-ninth parallel. Department of Mines Geological Survey of Canada, Ottawa.

Demicco, R.V., Hardie, L.A., 1994. An Inventory of Common Sedimentary Structures and Early Diagenetic Features of Shallow Marine Carbonate Deposits. Society for Sedimentary Geology, Tulsa, Oklahoma.

Dickson, J., Barber, C., 1976. Petrography, chemistry and origin of early diagenetic concretions in the Lower Carboniferous of the Isle of Man. Sedimentology 23, 189-211.

Du, Y., Han, X., Gu, S., Lin, W., Zhang, C., 2001. Earthquake event deposits in Mesoproterozoic Kunyang Group in Central Yunnan Province and its geological implications. Science in China (Series D) 31, 283-289.

Duck, R., 1995. Subaqueous shrinkage cracks and early sediment fabrics preserved in Pleistocene calcareous concretions. Journal of the Geological Society 152, 151-156.

Eby, D., 1975. Carbonate sedimentation under elevated salinities and implications for the origin of “molar-tooth” structure in the Middle Belt Carbonate interval (late Precambrian), northwestern Montana. Abstracts with Program 7, 1063.

Fairchild, I.J., Einsele, G., Song, T., 1997. Possible seismic origin of molar tooth structures in Neoproterozoic carbonate ramp deposits, north China. Sedimentology 44, 611-636.

Feistner, K., 1989. Petrographic examination and re-interpretation of concretionary carbonate horizons from the Kimmeridge Clay, Dorset. Journal of the Geological Society 146, 345-350.

Fenton, C.L., Fenton, M.A., 1937. Belt series of the North: Stratigraphy, sedimentation, paleontology. Bulletin of the Geological Society of America 48, 1873-1970.

Fisher, Q., Raiswell, R., Marshall, J., 1998. Siderite concretions from nonmarine shales (Westphalian A) of the Pennines, England; controls on their growth and composition. Journal of Sedimentary Research 68, 1034-1045.

Frank, T.D., Lyons, T.W., 1998. “Molar-tooth” structures: A geochemical perspective on a Proterozoic enigma. Geology 26, 683-686.

Furniss, G., Rittel, J.F., Winston, D., 1998. Gas bubble and expansion crack origin of "molar-tooth" calcite structures in the Middle Proterozoic Belt Supergroup, Western Montana. Journal of Sedimentary Research 68, 104-114.

Fürsich, F., Oschmann, W., Singh, I., Jaitly, A., 1992. Hardgrounds, reworked concretion levels and condensed horizons in the Jurassic of western India: their significance for basin analysis. Journal of the Geological Society 149, 313-331.

Gao, L., Zhang, C., Liu, P., Tang, F., Song, B., Ding, X., 2009. Reclassification of the Meso-and Neoproterozoic chronostratigraphy of North China by SHRIMP zircon ages. Acta Geologica Sinica-English Edition 83, 1074-1084.

Gilleaudeau, G., Kah, L., 2010. Molar-tooth crack formation and the Proterozoic marine substrate: Insights from the Belt Supergroup, Montana and the Atar Group, Mauritania. Geological Society of America Abstracts with Programs 42, 137.

Goodman, E.E., Kah, L., 2007. Reassessing formation of Precambrian molar-tooth microspar: constraints from carbonate precipitation experiments. Geological Society of America Abstracts with Programs 39, 420.

Hallam, A., 1969. A pyritized limestone hardground in the Lower Jurassic of Dorset (England). Sedimentology 12, 231-240.

He, T., Zhou, Y., Vermeesch, P., Rittner, M., Miao, L., Zhu, M., Carter, A., von Strandmann, P.A.P., Shields, G.A., 2017. Measuring the 'Great Unconformity'on the North China Craton using new detrital zircon age data. Geological Society, London, Special Publications 448, 145-159.

Hennessy, J., Knauth, L.P., 1985. Isotopic variations in dolomite concretions from the Monterey Formation, California. Journal of Sedimentary Research 55, 120-130.

Hesselbo, S., Palmer, T., 1992. Reworked early diagenetic concretions and the bioerosional origin of a regional discontinuity within British Jurassic marine mudstones. Sedimentology 39, 1045-1065.

Higgins, J.A., Fischer, W., Schrag, D., 2009. Oxygenation of the ocean and sediments: consequences for the seafloor carbonate factory. Earth and Planetary Science Letters 284, 25-33.

Hodgskiss, M.S.W., Kunzmann, M., Poirier, A., Halverson, G.P., 2018. The role of microbial iron reduction in the formation of Proterozoic molar tooth structures. Earth and Planetary Science Letters 482, 1-11.

Horodyski, R.J., 1976. Stromatolites of the upper Siyeh limestone (Middle Proterozoic), Belt Supergroup, Glacier National Park, Montana. Precambrian Research 3, 517-536.

Hounslow, M.W., 1997. Significance of localized pore pressures to the genesis of septarian concretions. Sedimentology 44, 1133-1147.

Hudson, J., 1978. Concretions, isotopes, and the diagenetic history of the Oxford Clay (Jurassic) of central England. Sedimentology 25, 339-370.

Huggett, J., 1994. Diagenesis of mudrocks and concretions from the London Clay Formation in the London Basin. Clay Minerals 29, 693-707.

James, N.P., Narbonne, G.M., Sherman, A.G., 1998. Molar-tooth carbonate: Shallow subtidal facies of the Mid- to Late Proterozoic. Journal of Sedimentary Research 68, 716-722.

Jia, Z.H., Hong, T.Q., Zheng, W.W., Li, S.Y., 2003. The characters and environments of the seismites of the Neoproterozoic Wangshan Formation in North Anhui. Journal of Stratigraphy 27, 146-149, 158.

Jia, Z.H., Ning, X.F., Hong, T.Q., Zheng, W.W., 2011. The Neoproterozoic molar-tooth carbonate rock veins in northern Anhui and Jiangsu Provinces and their forming mechanism. Journal of Paleogeography 13, 627-634.

Kah, L.C., Bartley, J., Milam, K., 2007. Unusual breccias in the Proterozoic Atar Group, Mauritania-Mali-Algeria: potential deposition related to extraterrestrial impact and impact-related tsunamis. Geological Society of America Abstracts with Programs 39, 311.

Kah, L.C., Bartley, J.K., Teal, D.A., 2012. Chemostratigraphy of the Late Mesoproterozoic Atar Group, Taoudeni Basin, Mauritania: Muted isotopic variability, facies correlation, and global isotopic trends. Precambrian Research 200-203, 82-103.

Kah, L.C., Bartley, J.K., 2021. Carbonate fabric diversity and environmental heterogeneity in the late Mesoproterozoic Era. Geological Magazine, 1-27.

Kah, L.C., Knoll, A.H., 1996. Microbenthic distribution of Proterozoic tidal flats: Environmental and taphonomic considerations. Geology 24, 79-82.
Knoll, A., Swett, K., 1990. Carbonate deposition during the late Proterozoic Era: an example from Spitsbergen. American Journal of Science 290, 104-132.
Kriscautzky, A., Kah, L.C., Bartley, J.K., 2022. Molar-Tooth Structure as a Window into the Deposition and Diagenesis of Precambrian Carbonate. Annual Review of Earth and Planetary Sciences 50, 205-230.
Kuang, H.-W., 2014. Review of molar tooth structure research. Journal of Paleogeography 3, 359-383.
Kuang, H.W., Jin, G.C., Liu, Y.X., 2009. Genesis tpes of the Neoproterozoic molar tooth structures in the southeastern Jilin and eastern Liaoning provinces and its research significances. Science in China Series D: Earth Sciences 52, 135-142.
Kuznetsov, V., 2003. The "molar tooth" structure and its relation to bios evolution. Doklady Earth Sciences 392, 947-950.
Liu, Y., Gao, L., Liu, Y., 2005. Neoproterozoic Molar-tooth Structure and Constraint of Depositional Facies and Environment in the North China Platform in Jiangsu, Anhui and Liaoning, Eastern China. Acta Geologica Sinica 79, 533-539.
Long, D.G.F., 2007. Tomographic study of Paleoproterozoic carbonates as key to understanding the formation of molar-tooth structure. Gondwana Research 12, 566-570.
Ma, X.F., 2015. Sedimentary Environment Evolution and Event Deposition of the Lower Neoproterozoic in Xuzhou Area, China University of Mining and Technology.
Maples, C.G., 1986. Enhanced paleoecological and paleoenvironmental interpretations result from analysis of early diagenetic concretions in Pennsylvanian shales. Palaios, 512-516.
Marshall, D., Anglin, C., 2004. CO_2-clathrate destabilization: a new model of formation for molar tooth structures. Precambrian Research 129, 325-341.
Martill, D.M., 1988. Preservation of fish in the Cretaceous Santana Formation of Brazil. Palaeontology 31, 1-18.
Martill, D.M., Hudson, J.D., 1989. Injection clastic dykes in the Lower Oxford Clay (Jurassic) of central England: relationship to compaction and concretion formation. Sedimentology 36, 1127-1133.
McMahon, S., van Smeerdijk Hood, A., McIlroy, D., 2016. The origin and occurrence of subaqueous sedimentary cracks, In: Brasier, A.T., McIlroy, D., McLoughlin, N. (Eds.), Earth System Evolution and Early Life: a Celebrtion of the Work of Martin Brasier. Geological Society of London, Special Publication 448, London 448, pp. 285-309.
Mei, M., Tucker, M.E., 2011. Molar tooth structure: a contribution from the Mesoproterozoic Gaoyuzhuang Formation, Tianjin City, North China. Acta Geologica Sinica-English Edition 85, 1084-1099.
Meng, X.H., Ge, M., 2002. The sedimentary features of Proterozoic microspar (molar-tooth) carbonates in China and their significance. Episodes 25, 185-195.
Miller, K., Simpson, E.L., Sherrod, L., Wizevich, M.C., Malenda, M., Morgano, K., Richardson, A., Livingston, K., Bogner, E., 2018. Gas bubble cavities in deltaic

muds, Lake Powell delta, Glen Canyon National Recreation Area, Hite, Utah. Marine and Petroleum Geology 92, 904-912.
Moussine-Pouchkine, A., Bertrand-Sarfati, J., 1997. Tectonosedimentary subdivisions in the Neoproterozoic to Early Cambrian cover of the Taoudenni Basin (Algeria-Mauritania-Mali). Journal of African Earth Sciences 24, 425-443.
O'Connor, M.P., 1972. Classification and environmental interpretation of the cryptalgal organosedimentary "molar-tooth" structure from the late Precambrian Belt-Purcell Supergroup. Journal of Geology 80, 592-610.
Orr, P.J., Briggs, D.E., Siveter, D.J., Siveter, D.J., 2000. Three-dimensional preservation of a non-biomineralized arthropod in concretions in Silurian volcaniclastic rocks from Herefordshire, England. Journal of the Geological Society 157, 173-186.
Petrov, P.Y., 2011. Molar tooth structures: Formations and specificity of carbonate diagenesis in the Late Precambrian, Middle Riphean Sukhaya Tunguska Formation of the Turukhansk Uplift, Siberia. Stratigraphy and Geological Correlation 19, 247-267.
Plummer, P.S., Gostin, V.A., 1981. Shrinkage cracks: disiccation or synaeresis? Journal of Sedimentary Petrology 51, 1147-1156.
Pollock, M.D., Kah, L.C., Bartley, J.K., 2006. Morphology of Molar-Tooth Structures in Precambrian Carbonates: Influence of Substrate Rheology and Implications for Genesis. Journal of Sedimentary Research 76, 310-323.
Pope, M.C., Bartley, J.K., Knoll, A.H., Petrov, P.Y., 2003. Molar tooth structures in calcareous nodules, early Neoproterozoic Burovaya Formation, Turukhansk region, Siberia. Sedimentary Geology 158, 235-248.
Pratt, B.R., 1998. Syneresis cracks: subaqueous shrinkage in argillaceous sediments caused by earthquake-induced dewatering. Sedimentary Geology 117, 1-10.
Pratt, B.R., 2001. Oceanography, bathymetry and syndepositional tectonics of a Precambrian intracratonic basin: integrating sediments, storms, earthquakes and tsunamis in the Belt Supergroup (Helena Formation, ca. 1.45 Ga), western North America. Sedimentary Geology, 371-394.
Pratt, B.R., 2011. Molar-tooth structure, In: Reitner, J., Thiel, V. (Eds.), Encyclopedia of Geobiology. Springer, University of Göttingen, Germany, pp. 662-666.
Qiao, X., Song, T., Gao, L.Z., Peng, Y., Li, H., Gao, M., Song, B., Zhang, Q., 1994. Seismic Sequence in Carbonate Rocks By Vibrational Liquefaction. Acta Geologica Sinica-English Edition 7, 243-265.
Raiswell, R., 1971. The growth of Cambrian and Liassic concretions. Sedimentology 17, 147-171.
Raiswell, R., 1976. The microbiological formation of carbonate concretions in the Upper Lias of NE England. Chemical Geology 18, 227-244.
Raiswell, R., Fisher, Q., 2000. Mudrock-hosted carbonate concretions: a review of growth mechanisms and their influence on chemical and isotopic composition. Journal of the Geological Society 157, 239-251.
Rezak, R., 1957. Stromatolites of the Belt series in Glacier National Park and vicinity, Montana. USGS Professional Paper 294(D), 127-154.

Ross, C.P., 1959. Geology of Glacier National Park and the Flathead region, northwestern Montana. US Geological Survey.
Savrda, C.E., Bottjer, D.J., 1988. Limestone concretion growth documented by trace-fossil relations. Geology 16, 908-911.
Sellés-Martínez, J., 1996. Concretion morphology, classification and genesis. Earth-Science Reviews 41, 177-210.
Shields, G.A., 2002. 'Molar-tooth microspar': a chemical explanation for its disappearance ~ 750 Ma. Terra Nova 14, 108-113.
Siebach, K., Grotzinger, J., Kah, L., Stack, K., Malin, M., Léveillé, R., Sumner, D., 2014. Subaqueous shrinkage cracks in the Sheepbed mudstone: Implications for early fluid diagenesis, Gale crater, Mars. Journal of Geophysical Research: Planets 119, 1597-1613.
Smith, A., 2016. A review of molar-tooth structures with some speculations on their origin, In: MacLean, J.S., Sears, J.W. (Eds.), Belt Basin: Window to Mesoproterozoic Earth. Geological Society of America Special Paper 522, pp. 71-99.
Smith, G.A., 1968. The Origin and Deformation of Some "Molar-Tooth" Structures in the Precambrian Belt-Purcell Supergroup. Journal of Geology 76, 426-443.
Stack, K., Grotzinger, J., Kah, L., Schmidt, M., Mangold, N., Edgett, K., Sumner, D., Siebach, K., Nachon, M., Lee, R., 2014. Diagenetic origin of nodules in the Sheepbed member, Yellowknife Bay formation, Gale crater, Mars. Journal of Geophysical Research: Planets 119, 1637-1664.
Stagner, A.F., Bartley, J.K., Kah, L.C., 2004. Variation in deformation style of molar-tooth structure during fluidization: Tawaz Formation, Atar Group, Mauritania. Geological Society of America Abstracts with Programs 36, 88.
Stewart, E.K., Mauk, J.L., 2017. Sedimentology, sequence-stratigraphy, and geochemical variations in the Mesoproterozoic Nonesuch Formation, northern Wisconsin, USA. Precambrian Research 294, 111-132.
Sun, F., Peng, P., Zhou, X., Magalhaes, A., Guadagnin, F., Zhou, X., Zhang, Z., Su, X., 2020. Provenance analysis of the late Mesoproterozoic to Neoproterozoic Xuhuai Basin in the southeast North China Craton: Implications for paleogeographic reconstruction. Precambrian Research 337, 105554.
Sun, L., Gui, H., Chen, S., Ma, Y., He, Z., 2011. Geochemical characteristics and geological significance of the Neoproterozoic carbonates from northern Anhui Province, China. Chinese Journal of Geochemistry 30, 40-50.
Sun, L., Gui, H., Chen, S., 2012. Geochemistry of sandstones from the Neoproterozoic Shijia Formation, northern Anhui Province, China: implications for provenance, weathering and tectonic setting. Geochemistry 72, 253-260.
Sun, L., Gui, H., Chen, S., 2013. Geochemistry of sandstones from the Neoproterozoic Jinshanzhai Formation in northern Anhui Province, China: Provenance, weathering and tectonic setting. Chinese Journal of Geochemistry 32, 95-103.
Tang, L., Santosh, M., Dong, Y., 2015. Tectonic evolution of a complex orogenic system: evidence from the northern Qinling belt, central China. Journal of Asian Earth Sciences 113, 544-559.

Wang, L.J., 2009. Stratigraphic division, correlation and sedimentary environment analysis of the Neoproterozoic in Xuhuai region, Shandong University of Science and Technology.

Winston, D., 1986. Sedimentation and tectonics of the Middle Proterozoic Belt Basin and their influence on Phanerozoic compression and extension in western Montana and northern Idaho, In: Peterson, J.A. (Ed.), Paleotectonics and Sedimentation in the Rocky Mountain Region, United States. American Association of Petroleum Geologists Memoir 41, pp. 87-118.

Winston, D., Rittel, J.F., Furniss, G., 1999. Gas bubble and expansion crack origin of molar-tooth calcite structures in the Middle Proterozoic Belt Supergroup, western Montana - reply. Journal of Sedimentary Research 69, 1140-1145.

Xiao, S., Shen, B., Tang, Q., Kaufman, A.J., Yuan, X., Li, J., Qian, M., 2014. Biostratigraphic and chemostratigraphic constraints on the afe of early Neoproterozoic carbonate successions in North China. Precambrian Research 246, 208-225.

Young, G., Long, D., 1977. Carbonate sedimentation in a late Precambrian shelf sea, Victoria island, Canadian Arctic Archipelago. Journal of Sedimentary Research 47, 943-955.

APPENDIX I

Table 4. Occurrences of Molar-tooth structure (MTS).

Era	Bin (Ma)	Region	Unit	References
Archean	2600-2400	South Africa	Monteville Formation Gamohaan Formation	McMahon et al. (2016); Bishop and Sumner (2006); Bishop et al. (2006); Shields (2002)
Paleoproterozoic	2000-1800	Canada	Goulburn Group	Campbell and Cecile (1976)
Paleoproterozoic	1800-1600	Canada	Tukarak Formation Fairweather Formation	Hodgskiss et al. (2018); Ricketts and Donaldson (1981)
Paleoproterozoic	1800-1600	Canada	Gillespie Lake Group	Delaney (1981)
Mesoproterozoic	1600-1400	Canada	Chischa Formation George Formation	Bellefroid et al. (2019); Hodgskiss et al. (2018); Ross et al. (2001); Taylor and Stott (1973)
Mesoproterozoic	1600-1400	USA-Canada	Chamberlain Formation Newland Formation Helena/Siyeh and Wallace/Kitchner Fm Snowslip Formation	Smith (1968) O'Connor (1972) Taylor and Stott (1973) Höy (1993) Pratt (2011, 1999); Pratt (1998) Schieber (1992) Pollock et al. (2006); Marshall and Anglin (2004); Furniss et al. (1998)
Mesoproterozoic	1600-1400	Russia	Kaltasy Formation	Kah et al. (2007)
Mesoproterozoic	1600-1400	Russia	Burzyan Formation	Gao et al. (2007)
Mesoproterozoic	1400-1200	Canada	Sulky Formation Greenhorn Formation	Kah and Bartley (2021); Donaldson (1973)
Mesoproterozoic	1400-1200	China	Gaoyuzhuang Formation	Mei (2007, 2005) Li et al. (2010)
Mesoproterozoic	1400-1200	China	Wumishan Formation	Kuang et al. (2012); Kuang et al. (2009); Zhang et al. (2009)
Mesoproterozoic	1400-1200	Tasmania	Irby Siltstone/Humoldt Formation	Hodgskiss et al. (2018); Halpin et al. (2014); Calver and Baillie (1990)
Mesoproterozoic	1400-1200	India	Godavari Supergroup	Chaudhuri (2003); Sarkar and Bose (1992)
Mesoproterozoic	1200-1000	Canada	Iqquittuq Formation Angmaat Formation Victor Bay Formation	Kah and Bartley (2021); Hodgskiss et al. (2018); Kah et al. (2001); Sherman et al. (2001, 2000); Kah et al. (1999); James et al. (1998); Jackson and Iannelli (1981)

Table 4 continued

Era	Bin (Ma)	Region	Unit	References
Mesoproterozoic	1200-1000	Greenland	Narssarssuk Formation	Fairchild et al. (2000); Jackson (1986)
Mesoproterozoic	1200-1000	USA	Nonesuch Formation	Stewart and Mauk (2017)
Mesoproterozoic	1200-1000	Mauritania	Atar Formation Tawaz Formation	Kah and Bartley (2021); Kah et al. (2012); Gilleaudeau and Kah (2010); Shields (2002); Moussine-Pouchkine and Bertrand-Sarfati (1997); Moussine-Pouchkine et al. (1988)
Mesoproterozoic	1200-1000	Russia	Avzyan Formation	Kah and Bartley (2021); Bartley et al. (2007); Maslov and Krupenin (1991); Keller and Chumakov (1983)
Mesoproterozoic	1200-1000	Russia	Sukhaya Tunguska Formation	Petrov (2016, 2011); Knoll et al. (1995); Petrov (1993)
Mesoproterozoic	1200-1000	Russia	Uchur-Maya Region	Semikhatov and Serebryakov (1983)
Mesoproterozoic	1200-1000	Russia	Yenesei Ridge	Semikhatov (1962)
Mesoproterozoic	1200-1000	Brazil	Paranoá Group	Alvarenga et al. (2014)
Mesoproterozoic	1200-1000	India	Deoban Limestone	Saha et al. (2021)
Mesoproterozoic	1200-1000	India	Bhander Limestone	Gilleaudeau et al. (2018); Bose et al. (2012)
Mesoproterozoic	1200-1000	India	Godavari Supergroup	Saha et al. (2021)
Neoproterozoic	1000-800	Russia	Burovaya Formation Shorikha Formation Miroyedikha Formation	Petrov and Semikhatov (2009); Pope et al. (2003); Petrov and Semikhatov (2001, 1998); Gorokhov et al. (1995)
Neoproterozoic	1000-800	Russia	Inzer Formation Uk Formation	Maslov et al. (2019); Keller and Chumakov (1983)
Neoproterozoic	1000-800	Canada	Fifteen Mile Group Hematite Group	Roest-Ellis et al. (2021); Hodgskiss et al. (2018); James et al. (1998); Hofmann (1985); Aitken (1981)
Neoproterozoic	1000-800	Canada	Little Dal Group	Turner and Bekker (2016); Turner et al. (1997); Strauss (1993); Hofmann (1985); Aitken (1981)
Neoproterozoic	1000-800	Canada	Boot Inlet Formation	Hodgskiss et al. (2018); Greenman (2017); Turner and Bekker (2016); James et al. (1998); Young (1981); Young and Long (1977)

Table 4 continued

Era	Bin (Ma)	Region	Unit	References
Neoproterozoic	1000-800	Svalbard	Backlundtoppen Formation Draken Formation Svenberjellet Formation	Tosca et al. (2011); Fairchild et al. (2000); Knoll and Swett (1990); Fairchild and Spiro (1987); Fairchild and Hambrey (1984); Knoll (1984)
Neoproterozoic	1000-800	Norway	Båtsfjord Formation	Hodgskiss et al. (2018); Siedlecka (1978)
Neoproterozoic	1000-800	UK	Ballachulish Limestone	Fairchild et al. (2018b)
Neoproterozoic	1000-800	China	Wanlong/Qinggouzi/Kanjia Formation	Wu et al. (2020); Kuang et al. (2004a); Kuang et al. (2004b); Kuang et al. (2004c); Meng and Ge (2002)
Neoproterozoic	1000-800	China	Xingmincun Formation	Yang et al. (2012); Gao et al. (2009); Fairchild et al. (2000); Fairchild et al. (1997); Qiao et al. (1994)
Neoproterozoic	1000-800	China	Jiayuan Formation Zhaowei Formation Niyuan Formation Jiudingshan Formation Weiji Formation	Zhou et al. (2020); Zhou (2017); Liu et al. (2016); Xiao et al. (2014); Jia et al. (2011); Liu et al. (2005); Jia (2004); Liu et al. (2004); Meng et al. (2004)
Neoproterozoic	1000-800	China	Hejaiyao Formation	Gao and Liu (2005)
Neoproterozoic	1000-800	China	Hejiazhai Formation	Wang and Li (2020); Yue et al. (2020)
Neoproterozoic	1000-800	China	Shiwangzhuang Formation	Kuang (2014); Wang et al. (2007)
Neoproterozoic	1000-800	China	Kunyang Group	Liu et al. (2010); Zhang et al. (2007); Du et al. (2001)
Neoproterozoic	1000-800	China	Kava Bulake, Xinjiang	Cai et al. (2013)
Neoproterozoic	800-600	Canada	Wynniatt Formation	Thomson et al. (2014); James et al. (1998); Young (1981); Young and Long (1977)
Neoproterozoic	800-600	Canada	Tindir Group	Young (1982)
Neoproterozoic	800-600	Svalbard	Elbobreen Formation	Fairchild et al. (2000); Knoll and Swett (1990); Fairchild and Spiro (1987); Fairchild and Hambrey (1984); Knoll (1984)
Neoproterozoic	800-600	Greenland	Upper Eleanore Bay Group	Halverson et al. (2004); Fairchild et al. (2000); Fairchild and Herrington (1989); Bertrand-Sarfati and Caby (1976)

Table 4 continued

Era	Bin (Ma)	Region	Unit	References
Neoproterozoic	800-600	UK	Lossit Limestone	Fairchild et al. (2018a)
Neoproterozoic	800-600	Australia	Bitter Springs Formation	Shields (2002); Southgate (1991)
Neoproterozoic	800-600	Ethiopia	Tambien Group	Park et al. (2020); MacLennan et al. (2018); Swanson-Hysell et al. (2015); Miller et al. (2009)
Neoproterozoic	800-600	USA	Kwagunt Formation	Walter et al. (2000)
Neoproterozoic	600-400	Namibia	Maieberg Formation	Hodgskiss et al. (2018)
Neoproterozoic	600-400	Australia	Wonoka Formation	Shields-Zhou et al. (2012); Shields (2002)

REFERENCES

Aitken, J., 1981. Stratigraphy and sedimentology of the Upper Proterozoic Little Dal Group, Mackenzie Mountains, Northwest Territories, In: Campbell, F.H.A. (Ed.), Proterozoic Basins of Canada. Geological Survey of Canada Paper 81, pp. 47-71.

Alvarenga, C.J.S., Santos, R.V., Vieira, L.C., Lima, B.A.F., Mancini, L.H., 2014. Meso-Neoproterozoic isotope stratigraphy on carbonates platforms in the Brasilia Belt of Brazil. Precambrian Research 251, 164-180.

Bartley, J.K., Kah, L.C., McWilliams, J.L., Stagner, A.F., 2007. Carbon isotope chemostratigraphy of the Middle Riphean type section (Avzyan Formation, Southern Urals, Russia): Signal recovery in a fold-and-thrust belt. Chemical Geology 237, 211-232.

Bellefroid, E., Planavsky, N.J., Hood, A., Halverson, G., Spokas, K., 2019. Shallow water redox conditions of the Mid-Proterozoic Muskwa Assemblage, British Columbia, Canada. American Journal of Science 319, 122-157.

Bertrand-Sarfati, J., Caby, R., 1976. Carbonates et stromatolites du sommet du Groupe d'Eleanore Bay (Precambrien terminal) au Canning Land (Groenland oriental). Grønlands Geologiske Undersøgelse 119, 51.

Bishop, J.W., Sumner, D.Y., 2006. Molar tooth structures of the Neoarchean Monteville Formation, Transvaal Supergroup, South Africa. I: Constraints on microcrystalline $CaCO_3$ precipitation. Sedimentology 53, 1049-1068.

Bishop, J.W., Sumner, D.Y., Huerta, N.J., 2006. Molar tooth structures of the Neoarchean Monteville Formation, Transvaal Supergroup, South Africa. II: A wave-induced fluid flow model. Sedimentology 53, 1069-1082.

Bose, P., Eriksson, P., Sarkar, S., Wright, D., Samanta, P., Mukhopadhyay, S., Mandal, S., Banerjee, S., Altermann, W., 2012. Sedimentation pattern during the Precambrain: Aunique record? Marine and Petroleum Geology 33, 34-68.

Cai, X., Tian, W., Zhang, X., Wu, L., 2013. Formation symbols and significance of Mesoproterozoic carbonate platform in the area of Kavabulake, Xianjiang. Resources Survey and Environment 34, 8-15.

Calver, C., Baillie, P., 1990. Early diagenetic concretions associated with intrastratal shrinkage cracks in an Upper Proterozoic dolomite, Tasmania, Australia. Journal of Sedimentary Petrology 60, 293-305.

Campbell, F.H.A., Cecile, M., 1976. Geology of Kilohigok Basin, Goulburn Group, Bathurst Inlet, District of Mackenzie. Geological Survey of Canada, Paper 76-1A, 369-377.

Chaudhuri, A., 2003. Stratigraphy and palaeogeography of the Godavari Supergroup in the south-central Pranhita–Go-davari valley, South India. Journal of Asian Earth Sciences 21, 295-611.

Delaney, G., 1981. The mid-Proterozoic Wenecke Supergroup, Wernecke Mountains, Yukon Territory, In: Campbell, F.H.A. (Ed.), Proterozoic Basins of Canada. Geological Survey of Canada Paper 81-10, pp. 1-23.

Donaldson, J., 1973. Possible correlations between Proterozoic strata of the Canadian Shield and North American Cordillera, Belt Symposium. University of Idaho, Moscow 1, pp. 61-75.

Du, Y., Han, X., Gu, S., Lin, W., Zhang, C., 2001. Earthquake event deposits in Mesoproterozoic Kunyang Group in Central Yunnan Province and its geological implications. Science in China (Series D) 31, 283-289.

Fairchild, I.J., Hambrey, M., 1984. The Vendian succession of northeastern Spitsbergen: Petrogenesis of a dolomite–tillite association. Precambrian Research 26, 111-167.

Fairchild, I.J., Spiro, B., 1987. Petrological and isotopic implications of some contrasting Late Precambrian carbonates, NE Spitsbergen. Sedimentology 34, 973-989.

Fairchild, I.J., Herrington, P., 1989. Carbonate shelf and slope facies evolution prior to Vendian glaciation, east central Greenland, In: Gayer, R. (Ed.), The Caledonide Geology of Scandinavia. Grahham & Trotman, London, pp. 263-273.

Fairchild, I.J., Einsele, G., Song, T., 1997. Possible seismic origin of molar tooth structures in Neoproterozoic carbonate ramp deposits, north China. Sedimentology 44, 611-636.

Fairchild, I.J., Spiro, B., Herrington, P., Song, T., 2000. Controls on Sr and C isotope compositions of Neoproterozoic Sr-rich limestones of east Greenland and north China, In: Grotzinger, J.P., James, N.P. (Eds.), Carbonate Sedimentation and Diagenesis in the Evolving Precambrian World. Society for Sedimentary Geology (SEPM), Tulsa Special Publication 67, pp. 297-313.

Fairchild, I.J., Spencer, A.M., Ali, D.O., Anderson, R.P., Anderton, R., Boomer, I., Dove, D., Evans, J.D., Hambrey, M.J., Howe, J., 2018a. Tonian-Cryogenian boundary sections of Argyll, Scotland. Precambrian Research 319, 37-64.

Fairchild, I.J., Spencer, A.M., Ali, D.O., Anderson, R.P., Anderton, R., Boomer, I., Dove, D., Evans, J.D., Hambrey, M.J., Howe, J., Sawaki, Y., Shields, G.A., Skelton, A., Tucker, M.E., Wang, Z., Zhou, Y., 2018b. Tonian-Cryogenian boundary sections of Argyll, Scotland. Precambrian Research 319, 37-64.

Furniss, G., Rittel, J.F., Winston, D., 1998. Gas bubble and expansion crack origin of "molar-tooth" calcite structures in the Middle Proterozoic Belt Supergroup, Western Montana. Journal of Sedimentary Research 68, 104-114.

Gao, L., Liu, Y., 2005. Microspar veins in the Neoproterozoic Hejiayao Formation in the Songshan area, Henan Province. Geological Review 51, 373-381.

Gao, L., Ding, X., Yin, C., Ren, L., Li, T., Chen, T., Chen, B., Li, G., Lu, S., 2007. Meso- and Neoproterozoic stratigraphic sequences in the southern Ural area and discovery of molar-tooth structures in carbonate and clastic rocks of the sequences and their geological significance. Geology in China 34, 962-973.

Gao, L., Zhang, C., Liu, P., Tang, F., Song, B., Ding, X., 2009. Reclassification of the Meso-and Neoproterozoic chronostratigraphy of North China by SHRIMP zircon ages. Acta Geologica Sinica-English Edition 83, 1074-1084.

Gilleaudeau, G., Kah, L., 2010. Molar-tooth crack formation and the Proterozoic marine substrate: Insights from the Belt Supergroup, Montana and the Atar Group, Mauritania. Geological Society of America Abstracts with Programs 42, 137.

Gilleaudeau, G.J., Sahoo, S.K., Kah, L.C., Henderson, M.A., Kaufman, A.J., 2018. Proterozoic carbonates of the Vindhyan Basin, India: Chemostratigraphy and diagenesis. Gondwana Research 57, 10-25.

Gorokhov, I.M., Semikhatov, M.A., Baskakov, A.V., Kutyavin, E.P., Melnikov, N.N., Sochava, A.V., Turchenko, T.L., 1995. Sr isotopic composition in Riphean, Vendian and Lower Cambrian carbonates from Siberia Stratigraphy and Geological Correlation 3, 1-28.

Greenman, W., 2017. Characterization of a ~1 billion year old carbonate ramp in the Brock Inlier, Arctic Canada, Carleton University, Ottawa, Ontario.

Halpin, J.A., Jensen, T., McGoldrick, P., Meffre, S., Berry, R.F., Everard, J.L., Calver, C.R., Thompson, J., Goemann, K., Whittaker, J.M., 2014. Authigenic monazite and detrital zircon dating from the Proterozoic Rocky Cape Group, Tasmania: Links to the Belt-Purcell Supergroup, North America. Precambrian Research 250, 50-67.

Halverson, G.P., Maloof, A.C., Hoffman, P.F., 2004. The Marinoan glaciation (Neoproterozoic) in northeast Svalbard. Basin Research 16, 297-324.

Hodgskiss, M.S.W., Kunzmann, M., Poirier, A., Halverson, G.P., 2018. The role of microbial iron reduction in the formation of Proterozoic molar tooth structures. Earth and Planetary Science Letters 482, 1-11.

Hofmann, H., 1985. The mid-Proterozoic Little Dal macrobiota, Mackenzie Mountains north-west Canada. Palaeontology 28, 331-354.

Höy, T., 1993. Geology of the Purcell Supergroup in the Fernie Westhalf Map Area, Southeastern British Columbia. Geological Survey of Canada Bulletin 84, 1-157.

Jackson, G., Iannelli, T., 1981. Rift-related cyclic sedimentation in the Neohelikian Borden Basin, northern Baffin Island, In: Campbell, F.H.A. (Ed.), Proterozoic Basins of Canada. Geological Survey of Canada Paper 81, pp. 269-302.

Jackson, G., 1986. Notes on the Proterozoic Thule Group, northern Baffin Bay. Geological Survey of Canada, Paper 86, 541-552.

James, N.P., Narbonne, G.M., Sherman, A.G., 1998. Molar-tooth carbonate: Shallow subtidal facies of the Mid- to Late Proterozoic. Journal of Sedimentary Research 68, 716-722.

Jia, Z.H., 2004. Research on the changing depositional environments and their biological response during the sedimentation of the Neoproterozoic Jiuliqiao Formation, Hauinan Region, Anhui Province, China Hefei University of Technology, Hefei, China.

Jia, Z.H., Ning, X.F., Hong, T.Q., Zheng, W.W., 2011. The Neoproterozoic molar-tooth carbonate rock veins in northern Anhui and Jiangsu Provinces and their forming mechanism. Journal of Paleogeography 13, 627-634.

Kah, L.C., Sherman, A.G., Narbonne, G.M., Knoll, A.H., Kaufman, A.J., 1999. $\delta^{13}C$ stratigraphy of the Proterozoic Bylot Supergroup, Baffin Island, Canada: implications for regional lithostratigraphic correlations. Canadian Journal of Earth Sciences 36, 313-332.

Kah, L.C., Lyons, T.W., Chesley, J.T., 2001. Geochemistry of a 1.2 Ga carbonate-evaporite succession, northern Baffin and Bylot Islands: implications for Mesoproterozoic marine evolution. Precambrian Research 111, 203-234.

Kah, L.C., Bartley, J., Milam, K., 2007. Unusual breccias in the Proterozoic Atar Group, Mauritania-Mali-Algeria: potential deposition related to extraterrestrial impact and impact-related tsunamis. Geological Society of America Abstracts with Programs 39, 311.

Kah, L.C., Bartley, J.K., Teal, D.A., 2012. Chemostratigraphy of the Late Mesoproterozoic Atar Group, Taoudeni Basin, Mauritania: Muted isotopic variability, facies correlation, and global isotopic trends. Precambrian Research 200-203, 82-103.

Kah, L.C., Bartley, J.K., 2021. Carbonate fabric diversity and environmental heterogeneity in the late Mesoproterozoic Era. Geological Magazine, 1-27.

Keller, B., Chumakov, N., 1983. Stratotype of Riphean. Stratigraphy. Geochronology. USSR Academy of Sciences, Geological Institute, Trudy 377, 1-184.

Knoll, A., Swett, K., 1990. Carbonate deposition during the late Proterozoic Era: an example from Spitsbergen. American Journal of Science 290, 104-132.

Knoll, A.H., 1984. Microbiotas of the late Precambrian Hunnberg Formation, Nordaustlandet, Svalbard. Journal of Paleontology 58, 131-162.

Knoll, A.H., Kaufman, A.J., Semikhatov, M.A., 1995. The carbon-isotopic composition of Proterozoic carbonates: Riphean successions from Northwestern Siberia (Anabar massif, Turukhansk uplift). American Journal of Science 295, 823-850.

Kuang, H.-W., Li, Y.-X., Zeng, Y.-T., Meng, X.-H., Ge, M., 2004a. Biomarkers in the molar tooth (MT)-bearing limestones in the Jilin-Liaoning area of China. Chinese Journal of Geochemistry 23, 334-341.

Kuang, H.-W., 2014. Review of molar tooth structure research. Journal of Paleogeography 3, 359-383.

Kuang, H., Liu, Y., Peng, N., Luo, S., Li, J., Cen, C., Chen, M., 2012. Molar-Tooth Structure from the Mesoproterozoic Wumishan Formation in Lingyuan, Yanshan Region, North China, and Geological Implications. Acta Geologica Sinica 86, 85-95.

Kuang, H.W., Jin, G.C., Liu, Y.X., Meng, X.H., Ge, M., 2004b. The environmental conditions of the microsparite (molar tooth) carbonates opened out by geochemistry: An example from the microsparite carbonates of Neoproterozoic in Ji-Liao region, China. Natural Gas Geoscience 15, 150-155.

Kuang, H.W., Liu, Y.X., Meng, X.H., Ge, M., Cai, G.Y., 2004c. Sedimentary lithofacies and petrological features of Neoproterozoic MT structures-bearing carbonates in Jilin-Liaoning area. Acta Geoscientica Sinica 25, 647-652.

Kuang, H.W., Jin, G.C., Liu, Y.X., 2009. Genesis tpes of the Neoproterozoic molar tooth structures in the southeastern Jilin and eastern Liaoning provinces and its research significances. Science in China Series D: Earth Sciences 52, 135-142.

Li, H.K., Zhu, S.X., Xiang, Z.Q., Su, W.B., Lu, S.N., Zhou, H.Y., Geng, J.Z., Li, S., Yang, F.J., 2010. Zircon U-Pb dating on tuff bed from Gaoyuzhuang Formation in Yanqing, Beijing: Further constraints on the new subdivision of the Mesoproterozoic stratigraphy in northern North China. Yanshi Xuebao 26, 2131-2140.

Liu, W., Meng, X., Ge, M., Kuang, H., Liu, Y., 2004. Origin of the Neoproterozoic molar-tooth carbonates in the Xuzhou-Huainan area. Geological Review 50, 454-463.

Liu, W., Liu, S., Sun, L., Bai, W., Ding, Z., Wang, Z., 2016. Neoproterozoic stratigraphic correlation of Subei-Huainan in China. Journal of Central South University 23, 1449-1458.

Liu, Y., Gao, L., Liu, Y., 2005. Neoproterozoic Molar-tooth Structure and Constraint of Depositional Facies and Environment in the North China Platform in Jiangsu, Anhui and Liaoning, Eastern China. Acta Geologica Sinica 79, 533-539.

Liu, Y.Q., Kuang, H.W., Peng, N., Liu, Y.X., Jiang, X.J., Xu, H., 2010. Proterozoic microspar and constraints of sedimentary environment in China. Acta Petrologica Sinica 26, 2122-2130.

MacLennan, S., Park, Y., Sawanson-Hysell, N., Maloof, A., Schoene, B., Gebreslassie, M., Antilla, E., Tesema, T., Alene, M., Haileab, B., 2018. The arc of the Snowball: U-Pb dates constrain the Islay anomaly and the initiation of the Sturtian glaciation. Geology 46, 539-542.

Marshall, D., Anglin, C., 2004. CO_2-clathrate destabilization: a new model of formation for molar tooth structures. Precambrian Research 129, 325-341.

Maslov, A.V., Krupenin, M.T., 1991. Riphean sections of the Baskiriya anticlinorium (western slope of the south Urals), Sverdlovsk. USSR Academy of Sciences, Uralian Branch, Institute of Geology and Geochemistry.

Maslov, A.V., Grazhdankin, D.V., Dub, S.A., Melnik, D.S., Parfenova, T.M., Kolesnikov, A.V., Cherednichenko, N.V., Kiseleva, D.V., 2019. Sedimentology and geochemistry of the Uk Formation, Upper Riphean, the Southern Urals. Lithosphere (Russia) 19, 659-686.

McMahon, S., van Smeerdijk Hood, A., McIlroy, D., 2016. The origin and occurrence of subaqueous sedimentary cracks, In: Brasier, A.T., McIlroy, D., McLoughlin, N. (Eds.), Earth System Evolution and Early Life: a Celebrtion of the Work of Martin Brasier. Geological Society of London, Special Publication 448, London 448, pp. 285-309.

Mei, M.X., 2005. Preliminary study on sequence-stratigraphic position and origin for molar-tooth structure of the Gaoyuzhuang Formation of Mesoproterozoic at Jixian section in Tianjin. Journal of Paleogeography 7, 437-447.

Mei, M.X., 2007. Implications of the Precambrian non-stromatolitic carbonate succession making up the third member of Mesoproterozoic Gaoyuzhuang Formation in Yanshan area of North China. Journal of China University of Geosciences 18, 191-209.

Meng, X., Ge, M., Liu, Y., Kuang, H., Liu, W., Bourrouilh-Le Jan, F.G., Bourrouilh, R., 2004. Molar-tooth Carbonate Sequences and Sr Isotopes in the Neoproterozoic for Stratigraphic Correlation: Research in the Jilin-Liaoning-Xuzhou-Huaiyang Area of the Sino-Korean Plate and Its Correlation with the Yangtze Plate. Acta Geologica Sinica 78, 775-783.

Meng, X.H., Ge, M., 2002. The sedimentary features of Proterozoic microspar (molar-tooth) carbonates in China and their significance. Episodes 25, 185-195.

Miller, N.R., Stern, R.J., Avigad, D., Beyth, M., Schilman, B., 2009. Cryogenian slate-carbonate sequences of the Tambien Group, northern Ethiopia (I): Pre-"Sturian" chemostratigraphy and regional correlations. Precambrian Research 170, 129-156.

Moussine-Pouchkine, A., Bertrand-Sarfati, J., Ball, E., Caby, R., 1988. Les séries sédimentaires et volcaniques anorogéniques protérozoïques impliquées dans la chaîne pan africaine: la région de l'Adrar Ahnet (NW Hoggar, Algérie). Journal of African Earth Sciences (and the Middle East) 7, 57-75.

Moussine-Pouchkine, A., Bertrand-Sarfati, J., 1997. Tectonosedimentary subdivisions in the Neoproterozoic to Early Cambrian cover of the Taoudenni Basin (Algeria-Mauritania-Mali). Journal of African Earth Sciences 24, 425-443.

O'Connor, M.P., 1972. Classification and environmental interpretation of the cryptalgal organosedimentary "molar-tooth" structure from the late Precambrian Belt-Purcell Supergroup. Journal of Geology 80, 592-610.

Park, Y., Swanson-Hysell, N.L., MacLennan, S.A., Maloof, A.C., Gebreslassie, M., Tremblay, M.M., Schoene, B., Alene, M., Anttila, E.S., Tesema, T., 2020. The lead-up to the Sturtian Snowball Earth: Neoproterozoic chemostratigraphy time-calibrated by the Tambien Group of Ethiopia. Geological Society of America Bulletin 132, 1119-1149.

Petrov, P.Y., 1993. Depositional environments of the lower formations of the Riphean Sequence, northern part of the Turukhansk Uplift, Siberia. Stratigraphy and Geological Correlation 1, 181-191.

Petrov, P.Y., Semikhatov, M.A., 1998. The Upper Riphean stromatolitic reefal complex: Burovaya Formation of the Turukhansk region, Siberia. Lithology and Mineral Resources 33, 539-560.

Petrov, P.Y., Semikhatov, M.A., 2001. Sequence organization and growth patterns of late Mesoproterozoic stromatolite reefs: An example from the Burovaya Formation, Turukhansk uplift, Siberia. Precambrian Research 111, 257-281.

Petrov, P.Y., Semikhatov, M.A., 2009. Platforms: Shorikha Formation of the Turukhansk uplift, Siberia. Stratigraphy and Geological Correlation 17, 461-475.

Petrov, P.Y., 2011. Molar tooth structures: Formations and specificity of carbonate diagenesis in the Late Precambrian, Middle Riphean Sukhaya Tunguska Formation of the Turukhansk Uplift, Siberia. Stratigraphy and Geological Correlation 19, 247-267.

Petrov, P.Y., 2016. Molar tooth structure and origin of peloids in Proterozoic carbonate platforms (Middle Riphean of the Turukhansk Uplift, Siberia). Lithology and Mineral Resources 51, 290-309.

Pollock, M.D., Kah, L.C., Bartley, J.K., 2006. Morphology of Molar-Tooth Structures in Precambrian Carbonates: Influence of Substrate Rheology and Implications for Genesis. Journal of Sedimentary Research 76, 310-323.

Pope, M.C., Bartley, J.K., Knoll, A.H., Petrov, P.Y., 2003. Molar tooth structures in calcareous nodules, early Neoproterozoic Burovaya Formation, Turukhansk region, Siberia. Sedimentary Geology 158, 235-248.

Pratt, B.R., 1998. Syneresis cracks: subaqueous shrinkage in argillaceous sediments caused by earthquake-induced dewatering. Sedimentary Geology 117, 1-10.

Pratt, B.R., 1999. Gas bubble and expansion crack origin of molar-tooth calcite structures in the Middle Proterozoic Belt Supergroup, Western Montana-Discussion. Journal of Sedimentary Research 69, 1136-1140.

Pratt, B.R., 2011. Molar-tooth structure, In: Reitner, J., Thiel, V. (Eds.), Encyclopedia of Geobiology. Springer, University of Göttingen, Germany, pp. 662-666.
Qiao, X., Song, T., Gao, L., Peng, Y., Li, H., Gao, M., Song, B., Zhang, Q., 1994. Seismic Sequence in Carbonate 1ocks By Vibrational Liquefaction. Acta Geologica Sinica 7, 243-267.
Ricketts, B., Donaldson, J., 1981. Sedimentary history of the Belcher Group of Hudson Bay, In: Campbell, F.H.A. (Ed.), Proterozoic Basins of Canada. Geological Survey of Canada Paper 81, pp. 235-254.
Roest-Ellis, S., Strauss, J.V., Tosca, N.J., 2021. Experimental constraints on nonskeletal $CaCO_3$ precipitation from Proterozoic seawater. Geology 49, 561-565.
Ross, G.M., Villeneuve, M.E., Theriault, R.J., 2001. Isotopic provenance of the lower Miskwa assemblage (Mesoproterozoic, Rocky Mountains, British Columbia): New clues to correlation and source areas. Precambrian Research 111, 57-77.
Saha, S., Dutt, S., Barkat, R., 2021. Enigmatic molar-tooth structures (MTS) from Mesoproterozoic Deoban limestone, NW-Lesser Himalaya: Evidence for microbial decay and *in-situ* precipitation. Journal of Earth System Science 130, 1-13.
Sarkar, S., Bose, P.K., 1992. Variations in Late Proterozoic stromatolites over a transition from basin plain to nearshore subtidal zone. Precambrian Research 56, 139-157.
Schieber, J., 1992. Facies and deposition of a mixed terrigenous-carbonate suite in a Mid-Proterozoic epicratonic sea: The Newland Formation, Belt Supergroup, Montana, U.S.A. . Neues Jahrbuch für Geologie und Paläontologie - Abhandlungen 184, 155-180.
Semikhatov, M.A., 1962. Riphean and Lower Cambrian of the Yenisei Ridge. USSR Academy of Sciences, Geological Institute, Trudy.
Semikhatov, M.A., Serebryakov, S.N., 1983. Siberian hypostratotype of the Riphean. USSR Academy of Sciences, Geological Institute, Trudy.
Sherman, A.G., Narbonne, G.M., James, N.P., 2000. Sedimentology of a late Mesoproterozoic muddy carbonate ramp, northern Baffin Island, Arctic Canada In: Grotzinger, J.P., James, N.P. (Eds.), Carbonate Sedimentation and Diagenesis in the Evolving Precambrian World. Society for Sedimentary Geology (SEPM), Tulsa Special Publication 67, pp. 275-294.
Sherman, A.G., Narbonne, G.M., James, N.P., 2001. Anatomy of a cyclically packed Mesoproterozoic carbonate ramp in northern Canada. Sedimentary Geology 139, 171-203.
Shields-Zhou, G.A., Hill, A.C., Macgabhann, B.A., 2012. The cyogenian period, In: Gradstein, F.M., Ogg, J.G., Schmitz, M.D., Ogg, G.M. (Eds.), The Geologic Time Scale. Elsevier, Boston, pp. 393-411.
Shields, G.A., 2002. 'Molar-tooth microspar': a chemical explanation for its disappearance ~ 750 Ma. Terra Nova 14, 108-113.
Siedlecka, A., 1978. Late Precambrian tidal-flat deposits and algal stromatolites in the Båtsfjord Formation, East Finnmark, North Norway. Sedimentary Geology 21, 277-310.
Smith, G.A., 1968. The Origin and Deformation of Some "Molar-Tooth" Structures in the Precambrian Belt-Purcell Supergroup. Journal of Geology 76, 426-443.

Southgate, P., 1991. A sedimentological model for the Loves Creek member of the Bitter Springs Formation, northern Amadeus Basin. Aus Bur Min Res Bulletin 236, 113-126.

Stewart, E.K., Mauk, J.L., 2017. Sedimentology, sequence-stratigraphy, and geochemical variations in the Mesoproterozoic Nonesuch Formation, northern Wisconsin, USA. Precambrian Research 294, 111-132.

Strauss, H., 1993. The sulfur isotopic record of Precambrian sulfates: new data and a critical evaluation of the existing record. Precambrian Research 63, 225-246.

Swanson-Hysell, N.L., Maloof, A.C., Condon, D.J., Jenkin, G.R.T., Alene, M., Tremblay, M.M., Tesema, T., Rooney, A.D., Haileab, B., 2015. Stratigraphy and geochronology of the Tambien Group, Ethiopia: Evidence for globally synchronous carbon isotope change in the Neoproterozoic. Geology 43, 323-326.

Taylor, G.C., Stott, D.F., 1973. Tuchodi Lakes map-area, British Columbia. Geological Survey of Canada, Memoir 373.

Thomson, D., Rainbird, R.H., Dix, G., 2014. Architecture of a Neoproterozoic intracratonic carbonate ramp succession: Wynniatt Formation, Amundsen Basin, Arctic Canada. Sedimentary Geology 299, 119-138.

Tosca, N.J., Macdonald, F.A., Strauss, J.V., Johnston, D.T., Knoll, A.H., 2011. Sedimentary talc in Neoproterozoic carbonate successions. Earth and Planetary Science Letters 306, 11-22.

Turner, E., Bekker, A., 2016. Thick sulfate evaporite accumulations marking a mid-Neoproterozoic oxygenation event (Ten Stone Formation, Northwest Territories, Canada). GSA Bulletin 128, 203-222.

Turner, E.C., James, N.P., Narbonne, G.M., 1997. Growth dynamics of Neoproterozoic calcimicrobial reefs, Mackenzie Mountains, northwest Canada. Journal of Sedimentary Research 67, 437-450.

Walter, M.R., Veevers, J.J., Calver, C.R., Gorjan, P., Hill, A.C., 2000. Dating the 840-544 Ma Neoproterozoic interval by isotopes of strontium, carbon, and sulfur in seawater, and some interpretative models. Precambrian Research 100, 371-433.

Wang, B.S., Zhang, X.Y., Li, J.B., 2007. Seismites sequence of Shiwangzhuang Formation of Neoproterozoic in South Shandong sector of Tancheng-Lujiang fault zone. Journal of Shandong University of Science and Technology (Natural Science) 26, 4-9, 22.

Wang, Z., Li, X., 2020. New understanding on the genetic mechanism of microsparite (molar-tooth) carbonates in the Neoproterozoic Hejiazhai Formation in Songshan area, Henan province. Journal of Paleogeography 22.

Wu, H., Wang, G., Ding, X., Wang, H., 2020. Geochemistry of the Neoproterozoic molar tooth carbonate in the Benxi Area, North China Craton: The paleo-ocean environment. Journal of Coastal Research 115, 446-450.

Xiao, S., Shen, B., Tang, Q., Kaufman, A.J., Yuan, X., Li, J., Qian, M., 2014. Biostratigraphic and chemostratigraphic constraints on the afe of early Neoproterozoic carbonate successions in North China. Precambrian Research 246, 208-225.

Yang, D.B., Xu, W.L., Xu, Y.G., Wang, Q.H., Pei, F.P., Wang, F., 2012. U-Pb ages and Hf isotope data from detrital zircons in the Neoproterozoic sandstones of northern Jiansu and southern Liaoning provinces, China: Implications for the Late Precambrian evolution of the southeastern North China Craton. Precambrian Research 216-219, 162-176.

Young, G., Long, D., 1977. Carbonate sedimentation in a late Precambrian shelf sea, Victoria island, Canadian Arctic Archipelago. Journal of Sedimentary Research 47, 943-955.

Young, G.M., 1981. The Amundsen Embayment, Northwest Territories; Relevance to the Upper Proterozoic evolution of North America, In: Campbell, F.H.A. (Ed.), Proterozoic Basins of Canada. Geological Survey of Canada Paper 81-10, pp. 203-218.

Young, G.M., 1982. The late Proterozoic Tindir Group, east-central Alaska: Evolution of a continental margin. Geological Society of America Bulletin 93, 759-783.

Yue, L., Liu, Z., Ma, Y., Chen, H., Wu, H., 2020. Sedimentary sequence and evolutionary history of the Proterozoic basin at the southern margin of North China Craton. Precambrian Research 344, 105765.

Zhang, C.H., Gao, L.Z., Wu, Z.J., Shi, X.Y., Yan, Q.R., Li, D.J., 2007. Zircon SHRIMP U-Pb ages of tuff in the Kunyang Group in central Yunnan province: Orogenic evidence for Grenville Period in South China. Chinese Science Bullitin 52, 818-824.

Zhang, S.-H., Zhao, Y., Yang, Z.-Y., He, Z.-F., Wu, H., 2009. The 1.35 Ga diabase sills from the northern North China Craton: implications for breakup of the Columbia (Nuna) supercontinent. Earth and Planetary Science Letters 288, 588-600.

Zhou, Q., Du, T., Guo, L., Sant, G., Bauchy, M., 2020. Role of Internal Stress in the Early-Stage Nucleation of Amorphous Calcium Carbonate Gels. Applied Sciences 10, 4359.

Zhou, Y., 2017. Reconstructing the strontium isotopic composition of Neoproterozoic seawater, University College London, London.

APPENDIX II

Table 5.1. Analytical conditions for the analysis of carbonates.

Element	JEOL JXA-8230	CAMECA
	Standard/crystal/average detection limit (ppm)/counting times on peak and background	Standard/average detection limit (ppm)
Fe	hematite/LiFH/150/10 s/5 s	siderite/150/160 s
Mn	pyrolusite/LiFH/150/10 s/5 s	spessartine/200/160 s
Mg	MgO/TAP/60/10 s/5 s	dolomite/100/60 s
Ca	calcite/PETJ/120/10 s/5 s	diopside
Ni	Nickeline/LiFH/180/10 s/5 s	
Zn	ZnO/LiFH/340/10 s/5 s	
Sr	celestite/PETJ/320/10 s/5 s	strontianite/220/160 s
Ba	baryte/PETJ/330/10 s/5 s	
Pb	Pyromorphite/PETJ/560/10 s/5 s	
Na	albite/TAP/150/5 s/2.5 s	
K	orthoclase/PETJ/90/10 s/5 s	
S	celestite/PETJ/230/10 s/5 s	

Blank: not analyzed.

Table 5.2. Analytical conditions for the analysis of silicates.

Element	JEOL JXA-8230
	Standard/crystal/average detection limit (ppm)
Fe	hematite/LiFH/140
Mn	pyrolusite/LiFH/140
Mg	MgO/TAP/70
Ca	anorthite/PETJ/130
Na	albite/TAP/140
K	orthoclase/PETJ/100
Cr	chromite/LiFH/150
Ti	ilmenite/PETJ/160
Al	albite/TAP/100
Si	albite/TAP/170

APPENDIX III

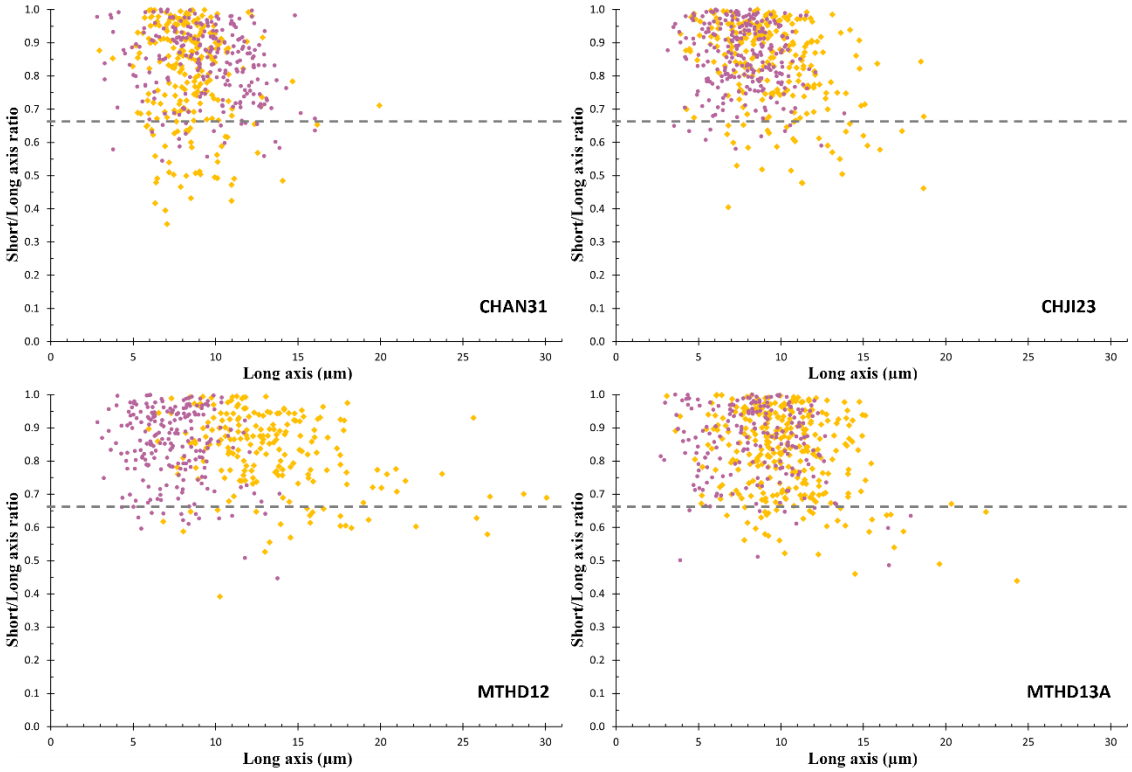


Figure 4.1. Distribution of the Short/Long axis ratio versus the long axis per individual sample. Pink (circles) represent MT cores, and yellow (diamonds) represent the whole crystal (core plus rim). Observe how the distribution of the cores remains within the cloud of the whole crystal. Dotted line at 0.66 ratio shows the arbitrary limit from which higher values (closer to 1) are considered equant shapes, and lower values (closer to 0) are not equant. Although variability is observed, average core shapes are equant, with only a few dots falling out of this range. Whole crystals show a wider range, although, as with cores, the higher density of points falls within equant proportions.

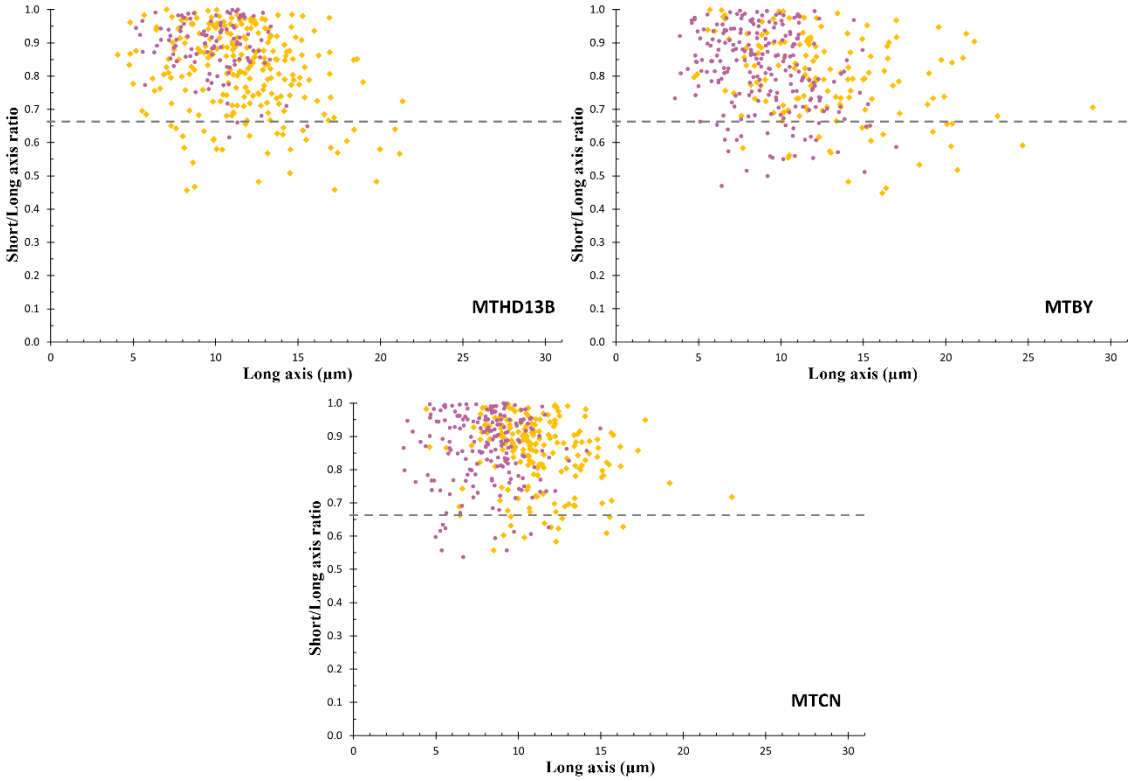


Figure 4.1 continued

VITA

Agustin Kriscautzky grew up in Catamarca Province, Northwest Argentina. After high school, with orientation in Biology, he went to Cordoba Province where he studied at the quadricentennial National University of Cordoba and earned a Bachelor of Science degree in Geology. After defending his BS thesis, he applied to the University of Tennessee, Knoxville, to pursue a Doctor of Philosophy degree in geology, focusing on sedimentology, stratigraphy, and geochemistry; he has also taught Physical Geology, Mineralogy, and Sedimentology and Stratigraphy. During his years at the institution, he also earned an MS degree in geology. His research involved the study of Precambrian marine carbonate rocks to better understand genesis, diagenesis, and potential implications of ancient carbonate fabrics. He is grateful for the encouragement and support from his family, friends, professors, and mentors as he moves forward in his professional life.